Abstract

Title: **CONTROLLED LIPOSOME FORMATION AND SOLUTE ENCAPSULATION WITH CONTINUOUS-FLOW MICROFLUIDIC HYDRODYNAMIC FOCUSING**

Andreas Jahn, Doctor of Philosophy, 2008

Directed By: **Professor Don L. DeVoe,**
Department of Mechanical Engineering

Liposomes enable the compartmentalization of compounds making them interesting as drug delivery systems. A drug delivery system (DDS) is a transport vehicle for a drug for *in vivo* drug administration. Drugs can be encapsulated, bound, or otherwise tethered to the carrier which can vary in size from tens of nanometers to a few micrometers. Liposomal DDSs have shown their capability to deliver drugs in a new fashion, allowing exclusive sales of encapsulated drugs to be extended beyond the initial compound's patent expiration date. However, existing methods to form liposomes and encapsulate drugs are based on bulk mixing techniques with limited process control and the produced liposomes frequently require post-processing steps.

In this dissertation, a new method is demonstrated to control liposome formation and compound encapsulation that pushes beyond existing benchmarks in liposome size homogeneity and adjustable encapsulation. The technology utilizes microfluidics for future pharmacy-on-a-chip applications. The microfluidic system allows for precise control of mixing *via* molecular diffusion with reproducible and controlled physicochemical conditions compared to traditional bulk-phase preparation techniques (*i.e.* test tubes and beakers). The laminar flow and facile fluidic control in microchannels

enables reproducible self-assembly of lipids into liposomes in a sheathed flow-field. Confining a water-soluble compound to be encapsulated to the immediate vicinity where liposome formation is expected to occur reduces sample consumption without affecting liposome loading. The ability to alter the concentration and control the amount of encapsulated compounds within liposomes in a continuous-flow mode is another interesting feature towards tailored liposomal drug delivery. The liposome formation strategy demonstrated in this dissertation offers potential for point-of-care drug encapsulation, eliminating shelf-life limitations inherent to current liposome preparation techniques.

CONTROLLED LIPOSOME FORMATION AND SOLUTE ENCAPSULATION WITH CONTINUOUS-FLOW MICROFLUIDIC HYDRODYNAMIC FOCUSING

By

Andreas Jahn

Dissertation submitted to the Faculty of the Graduate School of the
University of Maryland, College Park, in partial fulfillment
of the requirements for the degree of
Doctor of Philosophy
2008

Advisory Committee:
Professor Don L. DeVoe, Chair
Associate Professor Srinivasa Raghavan
Associate Professor Keith Herold
Assistant Professor Helim Aranda-Espinoza
Associate Professor David Bigio, Dean's representative

Acknowledgements

I would like to thank my research advisor, Don L. DeVoe, and my NIST project leaders, Michael Gaitan and Laurie E. Locascio for their years of project guidance, and for, of course, their financial support. Additionally, I am especially indebted to Wyatt N. Vreeland whose expertise and support served as an excellent complement in the pursuit of my graduate studies. Finally, I am grateful to Srinivasa Raghavan, Keith Herold, Helim Aranda-Espinoza, and David Bigio for the participation in my defense committee.

A must also express my gratitude to many of my coworkers at NIST who helped me with succeeding on my endeavors. These are in no particular order: Joseph E. Reiner, Sam Stavis, John Geist, Brian Nablo, Joey Robertson, Jane Wilkes, David Ross, Jennifer S. Hong, John J. Kasianowisz, Jason Karlj, and Nicole Morgan. Many thanks go to Russell E. Hajdaj at the NIST AML and John M. Moreland at NIST in Boulder for helping me with the chip fabrication.

Lastly, and most importantly, I want to thank Steffi Jacob for her undivided support and love on all my endeavors; Roland Raederscheidt, Tammy Macartney, Vivian Luna, Ksenia Brazhnik for their continuous motivation and belief during my graduate studies.

Table of Contents

Acknowledgements ii
Table of Contents iii
Chapter 1: Introduction 1
1.1 Motivation 1
1.2 What are Liposomes? 3
1.2.1 Classification of Liposomes 5
1.2.3 Traditional Liposome Bulk Formation Methods 9
1.3 Nanoparticle Formation with Microfluidics 12
Chapter 2: Concept of Microfluidic Liposome Formation 16
2.1 Liposome Formation with MHF 16
2.2 Encapsulation with MHF 20
2.3 Microfluidic Channel Design and Device Fabrication 23
2.3 Characterization of Liposome Size, Size Distribution, and Encapsulation 29
Chapter 3: Microfluidic Directed Liposome Formation of Controlled Size 33
3.1 Introduction 33
3.2 Description of Experimental Procedures 33
3.2.1 Device Fabrication 33
3.2.2 Materials 35
3.2.3 Liposome Formation 35
3.2.4 Microscopic Imaging 36
3.2.5 Cryogenic Transmission Electron Microscopy 36
3.2.6 Light Scattering and AF^4 Procedure 37
3.3 Results and Discussion 38
3.3.1 Influence of Q_t and Shear Forces on Liposomes Formation 41
3.3.2 Influence of FRR on Liposomes Formation 42
3.4 Summary 47
Chapter 4: Geometric and Hydrodynamic Aspects of Liposome Formation 48
4.1 Introduction 49
4.1 Description of Experimental Procedures 50
4.1.1 Device Fabrication 50
4.1.2 Materials 52
4.1.3 Liposome Formation 52
4.1.4 Light Scattering and AF^4 Procedure 52
4.2 Results and Discussion 53
..... 54
4.2.2 Influence of Microchannel Geometry on Liposome Formation 55
4.2.3 Influence of Q_t on Liposome Formation at High and Low FRRs 58
4.2.4 Influence of Diffusive and Convective Mixing on Liposome Formation. 60
4.2.5 Reproducibility of Liposome Formation with MHF 73
4.3 Summary 75
Chapter 5: Controlled Encapsulation of a Model Drug in Nano-Liposomes 77
5.1 Introduction 77
5.2 Description of Experimental Procedures 79
5.2.1 Materials 80

5.2.2 Liposome Formation 80
5.2.3 Fluorescence Fluctuation Spectroscopy 81
5.3 Results and Discussion 86
5.3.1 Liposome Size Distribution after Gel Permeation Chromatography 86
5.3.2 Free SRB Dye Fluctuations 88
5.3.3 High Encapsulation of Low Concentrated SRB in Nano-liposomes 91
5.3.4 Reducing the Amount of Non-Encapsulated SRB with MHF 96
5.4 Summary 100
Chapter 6: Summary and Future Work 102
6.1 Future Work: Functionalizing Liposomes 105
Appendix A 111
Gel Permeation Chromatography 111
Lightscattering 113
Quasi-Elastic Light Scattering 114
Multi-angle Laser Light Scattering 118
Asymmetric Flow Field-Flow Fractionation 124
Separation Method with AF^4 126
Fluorescence Correlation Spectroscopy 130
Fluorescence Cumulant Analysis 134
Nomenclature 138
Bibliography 140

Chapter 1: Introduction

1.1 Motivation

Utilizing liposomes as drug delivery systems (DDSs) offers the ability to formulate drugs for sustained release, targeted delivery, and extended longevity of sensitive encapsulated molecules.

A DDS is a combination of a transport vehicle and a drug for *in vivo* administration. Drugs can be encapsulated, bound, or otherwise tethered to the carrier, which can vary in size from tens of nanometers to a few micrometers. Examples for carriers are liposomes, solid lipid particles, polymeric particles, dendrimers, and functionalized particles.[1,2] DDS products amount to about 13 % of the global pharmaceutical market sales.[3] The global drug delivery market is predicted to have revenues of $543.8 billion with an expected annual growth rate of 5 % between 2005 and 2010.[4] The estimated sales of DDSs in the U.S. alone are expected to grow to $153.5 billion by 2011.[5] The success of a DDS is not determined by its level of sophistication but the ability to add value to the pharmaceutical product. One such value is found in life cycle management of already marketed products.[3] Drug companies face a substantial commercial demise of their major branded drugs as they reach their patent expiration date through reallocation of billions of dollars in revenues towards generic drug makers. DDSs can be applied to existing drugs to extend their commercial life.

Doxil®,the first liposomal DDS approved by the Food and Drug Administration (FDA) in 1995[6], gained sales of $177 million in the US and 5 major European countries in 2005.[7] Liposomal DDSs have shown their capability to deliver drugs in a new fashion, allowing exclusive sales of encapsulated drugs to be extended beyond the initial

compound's patent expiration date. However, existing methods to form liposomes and encapsulate drugs are based on bulk mixing techniques with limited process control and the produced liposomes frequently require post-processing steps. In this dissertation, a new method is proposed to control liposome formation and compound encapsulation that pushes beyond existing benchmarks in liposome size homogeneity and adjustable encapsulation. The technology utilizes microfluidics for future pharmacy-on-a-chip applications.

Microfluidics allows for explicit control of mixing *via* molecular diffusion with reproducible and controlled mechanical fluid forces over micrometer length-scales. Decreasing a sample streamwidth to sub-micrometer length-scales allows for controlled and reproducible mechanical and chemical conditions across the stream width, especially compared to traditional bulk-phase preparation techniques (*i.e.* test tubes and beakers). The laminar flow enables reproducible flow conditions for the self-assembly of lipids into liposomes in a sheathed flow-field. Confining a water-soluble substance to be encapsulated to the immediate vicinity of the alcohol stream where liposome formation is expected to occur reduces the sample consumption without adversely affecting the encapsulation of compounds into liposomes. The possibility of altering the concentration of the encapsulant from an initial starting concentration *via* controlled diffusive mixing enabling control over the loading efficiency of liposomes in a continuous flow mode is another interesting feature towards tailored liposomal drug delivery. The liposome formation strategy proposed in this dissertation could be implemented for point-of-care drug encapsulation eliminating shelf-life limitations of the liposome preparation method.

1.2 What are Liposomes?

Liposomes are microscopic spherical self-closed structures formed by one or more concentric lipid bilayers that can entrap water-soluble (hydrophilic) pharmaceutical agents in their internal water compartment and water-insoluble (hydrophobic) pharmaceuticals into the lipid-membrane, as shown in Figure 1.[8,9] Liposomes are made of amphiphiles (molecules composed of a polar and apolar region) and have attracted great interest since their discovery in 1965 by A. Bangham *et al.* for a wide range of biological, pharmaceutical, and industrial applications.[8,10-13] Liposomes are the smallest artificial vesicles of spherical shape, that can be completely produced from naturally occurring substances and are biocompatible, biodegradable, and non-immunogenic.[8]

All biological membranes contain lipids as primary constituents. Lipid molecules, the building blocks of liposomes, are surface-active amphiphiles with a head group that is strongly hydrophilic, coupled to a hydrophobic tail. Lipid molecules are insoluble in water and form colloidal dispersions. In this proposal, lipids are distinguished from detergent molecules by the fact that lipids are generally composed of two hydrocarbon chains, whereas detergent molecules contain only one hydrocarbon chain. If a large head group is attached to a single hydrocarbon chain, the molecule is wedge-shaped and will tend to form spherical micelles, which are spherical structures formed by a single layer of molecules that have a hydrocarbon core and a polar surface. A double tail yields a roughly cylindrical molecule. Such molecules can easily pack in parallel to form extended sheets of bilayer membranes with the hydrophilic head groups facing outwards into the aqueous regions on either side. The vesicle size ranges from 20 nm to several dozen micrometers while the thickness of the membrane is about 4 nm to 5 nm.

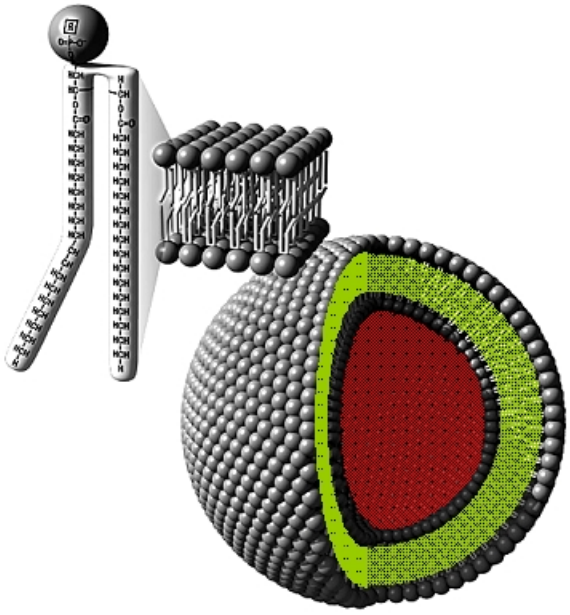

Figure 1 Schematic of a liposome that encapsulates a hydrophilic compound (red) in the interior and intercalates a lipophilic compound (green) within the lipid membrane. Shown is a lipid molecule that arranges into an ordered bilayer, which then closes into a spherical structure (liposome). Adapted from [14].

Because of their solubility properties the structure of liposomes involves the ordering of lipid molecules in such a way, that the polar head is in contact with water while the nonpolar hydrocarbon chain is hidden from water in the interior of the bilayered structures. Depending on the form factor of the lipid molecule they can form bilayers, micelles, or vesicles when in contact with water.

1.2.1 Classification of Liposomes

Liposomes occur in a large variety of structures. Figure 2 groups liposomes according to their structural properties and field of applications.[15] An important structural feature of liposomes is their size. Depending on its diameter liposomes are differentiated into small unilamellar (20 nm to 150 nm), large unilamellar (150 nm to 1000 nm), and multilamellar vesicles (>1000 nm). Liposomes can be composed of one or multiple bilayers and are distinguished into unilamellar or multilamellar vesicles. Further classification can be achieved by grouping liposomes according to their surface charge and surface property, which can be easily changed by modifying the lipid blend and adding new ingredients prior to the liposome preparation. Modifying the liposomes' coatings can result in long-circulating liposomes *in vivo*. The bandwidth of diagnostic or therapeutic applications of liposomes is very large. An example is immunoliposomes, liposomes that have antibodies attached to their surfaces, which are able to accumulate in a specific location in the body as they recognizes and bind to its antigen. In this proposal primarily anionic, small unilamellar liposomes without further surface modification through additional substances are investigated.

According to size

Small unilamellar vesicles (SUVs)

Large unilamellar/multilamellar vesicles (LUVs/LMVs)

Giant unilamellar/ mulilamellar vesicles (GUVs/GMVs)

According to circulation *in vivo*

Classical or conventional liposomes; sterically stabilized liposomes

According to lamellarity

Unilamellar, multilamellar

According to application

Diagnostic, therapeutic

According to surface charge

Cationic/Liposomal DNA vector, anionic, neutral

Specialized liposomes, targeted liposome

Immunoliposome, transferosome

Liposomal DNA vector, LPDI (cationic with poly-L-lysine DNA complex), LPDII (anionic)

Figure 2 Classification of liposomes according to their properties and applications.[15]

1.2.2 Applications of Liposomes

The ability to encapsulate and thereby segregate aqueous components led to a variety of applications of liposomes. These include their use in biological systems as quantized reagent packets for the delivery of genes[16,17] and deoxyribonucleic acid (DNA) vectors, drugs or other therapeutic agents[18-27], contrast agents for enhanced magnet resonance imaging (MRI)[28-31], model systems for the study of biological membranes and their fusion, transport studies, investigation of membrane proteins that can be reconstituted in liposomes,[32] encapsulation of cells and proteins[33], protective coatings for enzymes entrapped in silica sol-gel biocomposites[34], or as templates for the formation of solid hydrogel nanoparticles.[35,36] Liposomes are especially interesting as transport vehicles for *in vivo* applications such as drug delivery systems (DDSs) where they can achieve selective and high localization of active drug at the disease site. Due to their biphasic character, liposomes can act as carriers for both lipophilic drugs that are compartmentalized in the bilayer and hydrophilic compounds that are encapsulated in their aqueous interior. A homogenous size distribution is important to assure a controlled drug dosage while liposome size ultimately influences the detection and clearance rate by the complement system.[37]

The extreme versatility of liposomes is due to the variability in their composition and surface modifications that allow liposomes to be tailored to a myriad of specific applications. Modifying liposomes with low molecular weight polyethyleneglycol (PEG) renders their surface more hydrophilic, which allows increased circulation times in the blood stream. These so called "stealth" liposomes are currently being used as carriers for hydrophilic anticancer drugs like doxorubicin, mitoxantrone and others.[1] Other

modifications include rendering the liposome surface positive (cationic liposomes) for enhanced cell uptake or with antibodies for targeted drug delivery. Multiple liposomal DDSs that are FDA approved and have reached the market (*i.e.* Doxil/Caelyx (1995/1999), Myocet (2000), DepoCyt (1999), etc.) or are undergoing clinical evaluations are shown in Figure 3.[1,8]

Active drug	Product name‡	Indications
Daunorubicin	DaunoXome	Kaposi's sarcoma
Doxurubicin	Mycet	Combinational therapy of recurrent breast cancer
Doxorubicin in PEG-liposomes	Doxil/Caelyx	Refractory Kaposi's sarcoma; ovarian cancer; recurrent breast cancer
Amphotericin B	AmBisome	Fungal infections
Cytarabine	DepoCyt	Lymphomatous meningitis
Vincristine	Onco TCS	Non-Hodgkin's lymphoma
Lurtotecan	NX211	Ovarian cancer
Nystatin	Nyotran	Topical antifungal agent
All-*trans* retinoic acid	Altragen	Acute promyelocytic leukaemia; non-Hodgkin's lymphoma; renal-cell carcinoma; Kaposi's sarcoma
Platinum compounds	Platar	Solid tumours
Annamycin		Doxorubicin-resistant tumours
E1A gene		Various tumours
DNA plasmid encoding HLA-B7 and α2 microglobulin	Allovectin-7	Metastatic melanoma
Liposomes for various drugs and diagnostic agents (lipoMASC)		Broad applications

*In different countries the same drug could be approved for different indications or be at different phases of clinical trials). ‡Name of liposome formulation.

Figure 3 Liposomal drugs approved for clinical application or undergoing clinical evaluation. Adapted from Torchilin.[8]

1.2.3 Traditional Liposome Bulk Formation Methods

In order to produce liposomes, lipid molecules must be introduced into an aqueous environment. However, most of the liposome-forming molecules, including all phospholipids, are insoluble in water. Mixing of dry powders or waxes with water results in inefficacious formation of liposomes: most of the lipid is not fully hydrated but instead trapped in the interior of structures, which are hydrated only in the outermost bilayers. Furthermore, in most cases the lipid mixture will not mix evenly into the particles formed. Additional treatment such as prolonged heat and mechanical treatments, even if successful in hydrating the lipids, generate lipid degradation. To facilitate the hydration of lipids one has to increase the surface-to-volume ratio of the lipid. This is commonly done either by preparing a dried thin lipid-film by evaporation from an organic phase, a porous cake of freeze-dried lipid, or fine powder of spray-dried lipid from the organic solution. The alternative possibility is to introduce lipids directly into water from the organic phase. This can be accomplished, depending on the miscibility of the particular organic solvent with water by emulsification, injection, solvent dialyses and extraction. Upon diffusion of the organic solvent into the surrounding water and *vice versa*, lipid monomers aggregate as the solvent mixes with the surrounding aqueous solution.

There are a variety of methods available to produce liposomes in bulk solution processes (*e.g.*, alcohol injection [38-41], membrane extrusion [40], detergent dialysis [40], and sonication [40,42]), but in all cases they are formed by the self-assembly of phospholipid molecules in aqueous solution to form a lipid bilayer membrane that encapsulates an aqueous core. Comparison of liposome populations produced from those different techniques reveals a great deal of variability in terms of average diameter and size

homogeneity, but the narrowest size distributions are most often obtained from multi-step methods that include an initial self-assembly followed by a post-processing step (most often, sonication or membrane extrusion).

Figure 4 shows an overview of the most common procedures to generate liposomes from a lipid blend. In the commercially common thin-film-hydration method (Figure 4(→)) a lipid mixture is dissolved in an organic solvent, which is subsequently evaporated and results into a thin lipid-film on the inside wall of a glass flask. Hydration of the dry lipid-film with an aqueous solution and mechanical agitation results in the formation of liposomes.

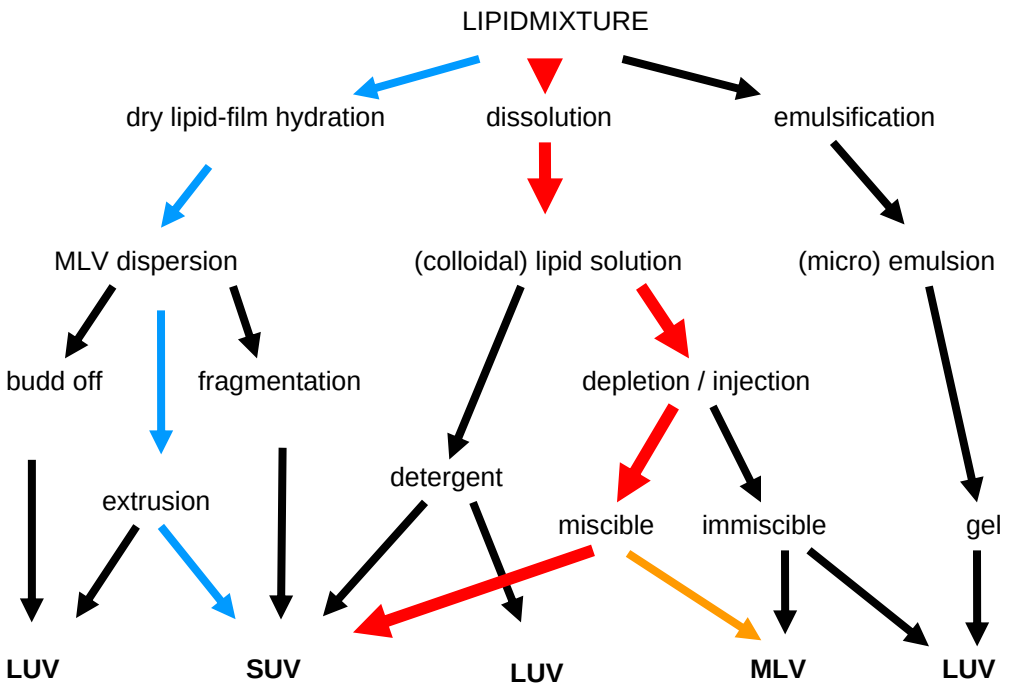

Figure 4 Overview of common liposome preparation techniques. The blue arrows (→) depict a very common liposome formation procedure. The red arrow (→) shows the basic steps of the solvent injection method that can result in SUVs and LUVs (→).

Liposomes prepared with thin-film-hydration are characterized by a very heterogeneous dispersion of predominantly large multi-lamellar vesicles (LMV's). Lipids can also be introduced into the aqueous phase directly from an organic solution (Figure 4 (→), (→)), so called alcohol injection method.[38-41] Solvent injection is used when the organic solution is water-miscible, whereas demulsification is used when the solvent is immiscible with water. Injection of a lipid-containing organic solution yields liposomes when the organic solvent concentration in the final homogenous solution falls below the solubility limit of lipids.

Additional mechanical, chemical, or electrostatic treatment will produce mixtures that form smaller less lamellar vesicles up to homogenous solutions of small unilamellar vesicles (SUV's) depending on the intensity of the respective post processing procedure. Most frequently, extrusion through filters with pores of different diameters, high pressure extrusion of a suspension of multilamellar liposomes through a French pressure cell[43], or sonication is applied to achieve a homogenous size of liposomes. In these post-processing techniques, the initial multilamellar vesicles are torn apart into small bilayered fragments or flakes, which upon fusion self-close into the desired small unilamellar vesicles.[32] Small unilamellar liposomes with diameters of approximately 25 nm are usually obtained by either directly immersing a high-energy probe sonicator into the liposome solution or by suspending phospholipid dispersion in a glass vial in a low-energy ultrasonic cleaning bath. High-energy sonication potentially causes oxidation and degradation of phospholipids and may damage the solute molecules it is desired to encapsulate in the liposomes interior space. Furthermore, titanium particles erode from the probe tip and have to be removed. Low-energy sonication as in the cleaning bath

varies often in its efficiency requiring prolonged periods of sonication, which at the end can also be destructive to the phospholipids molecules.[38]

In summary, traditional liposome preparation methods are generally conducted through mixing of bulk phases. The bulk methods often produce inhomogeneous chemical and/or mechanical conditions at the lipid phase–aqueous phase interface during liposome formation; resulting in liposomes that are polydisperse in size and lamellarity. To yield the desired homogeneous liposome populations traditional methods to formulate liposomes require additional steps such as solvent removal,[33] membrane extrusion,[38] or sonication[42]. Methods that can control liposome size during formation obviating additional steps would simplify their preparation. The challenge is to produce liposome formulations with a defined size for the specific application and with little size variation in their population, while guaranteeing batch-to-batch consistency. The methods for liposome production should also be flexible so that a protocol can be optimized for the desired concentration of encapsulated compounds and for functionalizing their surfaces. Lastly, shelf life of the formulation is of concern, and so the ability for production on demand would be of interest.

1.3 Nanoparticle Formation with Microfluidics

One of the great benefits of microfluidics is that it enables fine control and manipulation of fluids and fluid interfaces. Small packets of fluids with volumes measured in the picoliter- to attoliter-range can be manipulated, split, or combined with precise timing. Mixing can occur by simple diffusion or in a patterned channel that promotes folding of the fluid layers to reduce diffusion distances. Fluid streams flowing

toward one another can merge and form very sharp and well-defined interfaces by virtue of laminar flow.[44]

Application examples for microfluidic technologies which takes advantage of these features are synthesis, formation, and self-assembly of microscale and nanoscale particles. Nanoscale particles that have been formed using microfluidics include semiconductor quantum dots [45], metal colloids [46], and more recently, liposomes [41,47,48] and lipid nanotubes[49-51]. For both quantum dots and metal colloid formation, microfluidic synthesis has been reported to be superior to benchtop methods for producing high quality, monodisperse particles due to the ability maintaining fine control of all solution variables including reactant concentration, timing of reagent addition, and temperature.[52-55] Microfluidic methods for rapid mixing and exquisite control of reagent concentration can produce the precise conditions required for nanoparticle production. These methods include hydrodynamic focusing [56], flow lamination [57], and fluid folding [58] or chaotic mixing [59]. Flow focusing has been applied to generate homogeneous emulsion.[60]

Kuribayashi *et al.* showed electroformation of giant liposomes in microfluidic channels [61]. Specifically, a polymethylvinylsiloxane sheet containing the microchannel is sandwiched between two indium tin oxide glass plates which serve as transparent electrodes. A thin lipid film is dried on the bottom of a microchannel, hydrated with deionized water by capillary filling, and subsequently exposed to an alternating current (AC) signal producing giant unilamellar vesicles. Electro-formation of liposomes in this manner resulted in giant unilamellar liposomes (liposomes composed of a single bilayer membrane) in contrast to giant multilamellar liposomes (liposomes composed of many

bilayer membranes) that are produced by gentle hydration of lipid films without the electric field. Liposomes prepared by electro-formation were overall larger with a mean liposome diameter of about 12 µm compared to those produced by gentle hydration without applying an AC field with a mean liposome diameter of about 5 µm. This is thought to be due to liposome fusion caused by the vibrational energy induced by the AC field.

In another study Wagner *et al.* used the fluidic cross-flow ethanol injection method to produce homogenous liposome populations on an industrial scale.[41] The cross-flow injection technique utilizes two welded stainless steel tubes that form a cross, as shown in Figure 5.

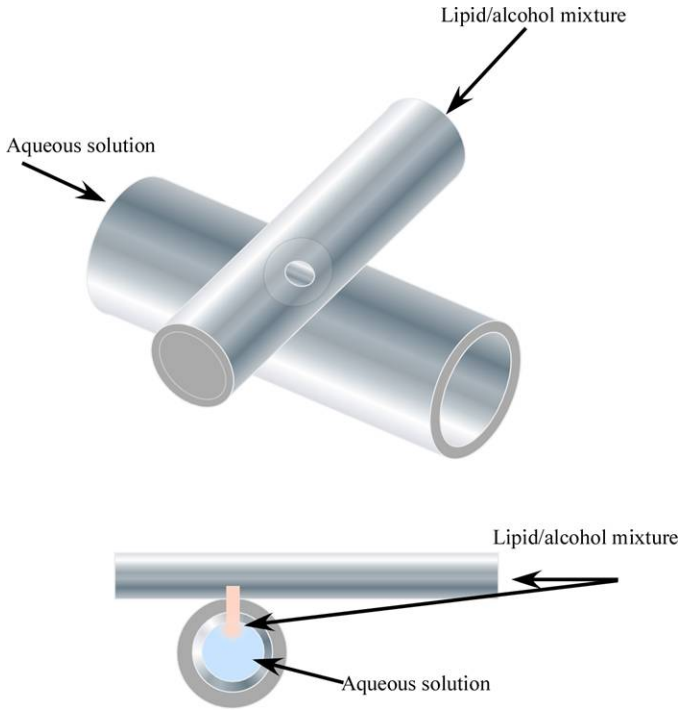

Figure 5 Welded steel tube arrangements of the Wagner[41] cross-flow method. The injection pinhole is 100 µm to 250 µm in diameter at the welded intersection.

At the connecting point a hole with a diameter of 150 µm to 250 µm serves as an injection point for a lipid/ethanol mixture. This method is an improvement to the traditional ethanol injection method in which a lipid/ethanol mixture is slowly injected manually into a rapidly vortexing aqueous buffer. The cross-flow injection method provides better control and reproducibility compared to manual injection of the lipid. In this method, the ethanol/lipid stream is injected obliquely into the water stream. One part of the ethanol/lipid stream forms a non-miscible interface with the stainless steel tubing and the other forms an active liquid miscible interface with the buffer. Liposomes form at the miscible buffer/ethanol interface. The liposomes produced with the cross-flow injection method vary in diameter between 200 nm and 500 nm.

Despite the development of a variety of new liposome formation methods there is still a limited understanding of the mechanism of lipid-to-liposomes self-assembly with conventional bulk methods. Vesicle formation is mostly determined by experimental parameters such as flow velocity, injection pressure, or stirring rate but precise control of the exact mixing parameters but their impact on formation remains untenable. This limited understanding is probably due to the often uncontrolled turbulent mixing conditions in batch processing[38,39] or visual inaccessibility of mixing performance[41].

In the following chapter a new method is described to produce homogeneous unimodal liposome populations with average vesicle diameters that can be chosen between 45 nm to 150 nm. Microfluidic hydrodynamic focusing (MHF) takes advantage of laminar flow in microfluidics. The microfluidic approach to form liposomes allows controlling the vesicle diameter and offers high reproducibility of the vesicle size distribution.

Chapter 2: Concept of Microfluidic Liposome Formation

2.1 Liposome Formation with MHF

Hydrodynamic focusing has been applied in various fields such as micromixers[56], flow cytometers[62], and fluidic switches to name a few. The concept of hydrodynamic focusing is based on conventional flow cytometry with an axially symmetric sample and sheath flow. A sample stream is thinned or focused by an adjacent sheath-flow and passed through a detection region, where particles or cells are counted or separated.[63] The focusing of the sample stream depends on the volumetric flow rate ratio between the sample and the surrounding sheath flow. Although the concept of hydrodynamic focusing and its rapid mixing on the micrometer length-scale is well established, hydrodynamic focusing to our knowledge has not been applied to control lipid self-assembly into liposomes in a microfluidic device until recently.[47,48]

The formation of vesicles with microfluidic hydrodynamic focusing (MHF) is adapted from the batch solvent injection method.[38,39] The conventional standard solvent injection into a glass vial filled with aqueous solution or buffer does not allow for reproducible control of shear forces and mixing conditions and therefore generally results in polydisperse liposome populations. Contrary, MHF enables the facile and reproducible control of the fluidic mixing conditions under laminar flow, thereby producing predictable flow conditions, which can be studied by fluid momentum and mass transport simulations. The focusing is visually accessible and allows the comparison of experimental with simulated focusing profiles. MHF produces a controlled steady-state concentration distribution profile of the miscible alcohol/water system. The controlled environment of the MHF method allows further elucidating the

vesicle formation process and investigating it more thoroughly by extracting the mixing details of alcohol and aqueous buffer in this system with numerical simulations. These include the concentration profiles of alcohol/water mixtures as they change for different focusing conditions and velocities as well as the viscous anisotropy that is often inherent in these miscible solvent-buffer combinations.[64-68]

Liposome formation in MHF occurs by a diffusively driven process, when a stream of lipids dissolved in an organic solvent such as 2-propanol (IPA) is hydrodynamically sheathed between two oblique phosphate buffered saline (PBS) streams in a microfluidic channel. The main concept of hydrodynamic focusing is to reduce the streamwidth and consequently the mixing path length of the focused stream. A stream of lipids resolubilized in IPA is hydrodynamically focused into a very narrow sheet with a thickness varying from a few micrometers down to sub-micrometers depending on the respective PBS-to-IPA volumetric flow rate ratios (FRR). The laminar flow conditions facilitate controlled diffusive mixing at the two liquid interfaces reproducibly diluting the IPA concentration below the solubility limit of lipids and initiating lipid self-assembly into small unilamellar vesicles ranging in diameters from 40 nm to 150 nm. In Figure 6a simulation of the mixing of IPA as it is focused by two oblique aqueous buffer streams and vesicle formation at the alcohol/water interface is shown. A fluorescence microscope image is shown in Figure 6b that depicts the focusing of a lipid stream containing a fluorophore in a microfluidic device.

a)

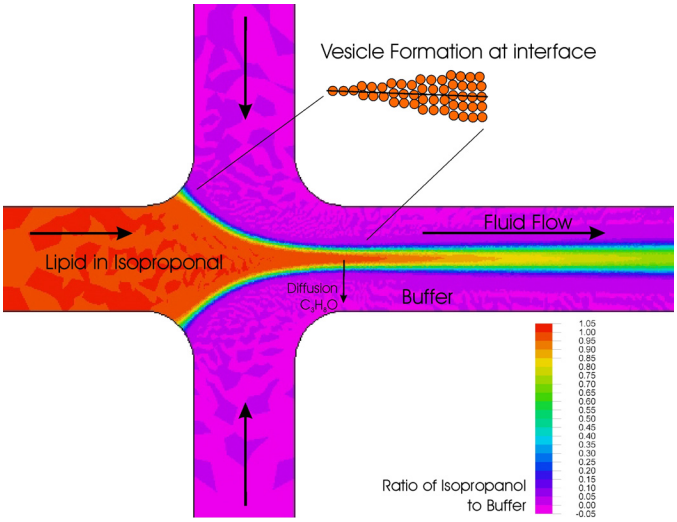

b)

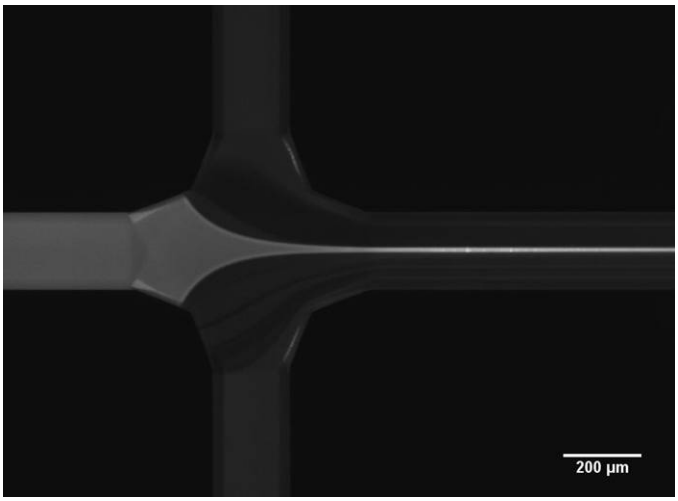

Figure 6 Schematic of the lipid self-assembly into liposomes with MHF (a). The color contours are generated by finite element analysis modeling of the flow field with Navier-Stokes convection and Stoke-Einstein diffusion equations and represent the concentration ratio of IPA to PBS. Lipid vesicles are formed where the concentration ratio of alcohol to buffer is at a critical condition and lipids are no longer soluble.[47] (b) Fluorescence microscope image of the focused IPA stream on a microfluidic chip (double cross design). A non-polar fluorophore (DiI_{C18}) is mixed into the IPA/lipid stream to visualize the focusing.

According to a theory by Lasic *et al.*, lipids dissolved in an organic solvent transform into intermediate bilayer phospholipids fragment (BPF) structures. Reducing the solubility conditions of lipids by increasing inter-diffusion of water and alcohol leads to thermodynamic instabilities at the edges of BPFs which induces bending and closing of the BPF upon itself and formation of vesicles.[32,47,48]

Changes in FRR result in variable stream widths of the focused solvent/lipid stream. As FRR decreases, the solvent stream width increases; therefore the concentration gradient decreases providing a central region with higher solvent content. This potentially stabilizes BPFs and allows larger congregation of lipids to yield larger BPFs, which eventually results in larger vesicles and broader distribution. At higher FRRs the solvent stream is focused into a narrower stream, the results are smaller and more homogenous liposome populations.

In contrast to batch solvent injection[38,39], from which MHF is adapted, MHF enables the facile and reproducible control of the fluidic mixing conditions under laminar flow, thereby producing predictable flow conditions. A controlled steady-state concentration distribution profile of the miscible alcohol-water system is established and can be studied by fluid momentum and mass transport simulations. The controlled environment of the MHF method allows further elucidating the vesicle formation process and investigating it more thoroughly by extracting the mixing details of alcohol and water in this system with numerical simulations. These include concentration profiles of IPA/water mixtures as they change for different focusing conditions and velocities as well as the viscous anisotropy (discussed in Chapter 4) often inherent in these miscible solvent-buffer systems.[64-68]

2.2 Encapsulation with MHF

Encapsulation of compounds into liposomes can be accomplished by one of three primary mechanisms: encapsulation, partitioning, and reverse/remote loading.[69] Encapsulation is useful for hydrophilic drugs, where the drug is dissolved in the hydration buffer. As the lipids self-assemble into liposomes in the hydration buffer they compartmentalize the drug in their aqueous interior. The partitioning strategy is suitable for lipophilic drugs, which are intercalated in the membrane interstitial of liposomes. The lipophilic drug is dissolved in a suitable organic solvent along with the phospholipids and subsequently added to the hydration buffer. As liposomes form, the drug is solubilized in the intrabilayer space. Residual solvent is removed under vacuum. Reverse or remote loading can be used for weakly acidic or alkaline drugs. Drug loading is achieved with either a pH gradient or an ammonium salt gradient between the inside and the outside of the liposome membrane. The idea is that neutral drug molecules are shuttled into the aqueous interior of the liposome across the phospholipid bilayer and become subsequently charged inside the liposome due to the different pH. Once charged, the drug molecule is not lipophilic enough to permeate through the bilayer again and is trapped inside the liposome.[69,70] The reverse loading method allows very high accumulation of the drug inside liposomes that can be as high as 100-fold the compound concentration in the remote loading medium and can achieve up to 90 % encapsulation efficiency.[71] Liposome loading of a hydrophilic drug simulant with MHF is accomplished by means of passive encapsulation. Encapsulation with the multiple-inlet microfluidic channel device addresses a major drawback in encapsulating solutes with other bulk formation processes. In Figure 7 the encapsulation of a hydrophilic drug with the standard alcohol injection method is depicted. An alcohol/lipid tincture is injected

with a syringe into an aqueous hydration buffer solution containing a homogenous concentration of drug. As lipids self-assemble into liposome due to the polarity of the hydration buffer, they simultaneously sequester the surrounding medium into the liposomes interior. However, due to the maximum amount of solvent that can be mixed with the hydration buffer and still result in formation of stable liposomes, only a fraction of the drug is eventually encapsulated in the liposome's interior. The non-encapsulated drug is subsequently separated from the liposome sample with gel filtration. To increase the encapsulation efficiency (the amount of drug encapsulated into liposomes versus the total amount of drug in the hydration buffer) it would be desirable to confine the drug only to the liposome formation region.

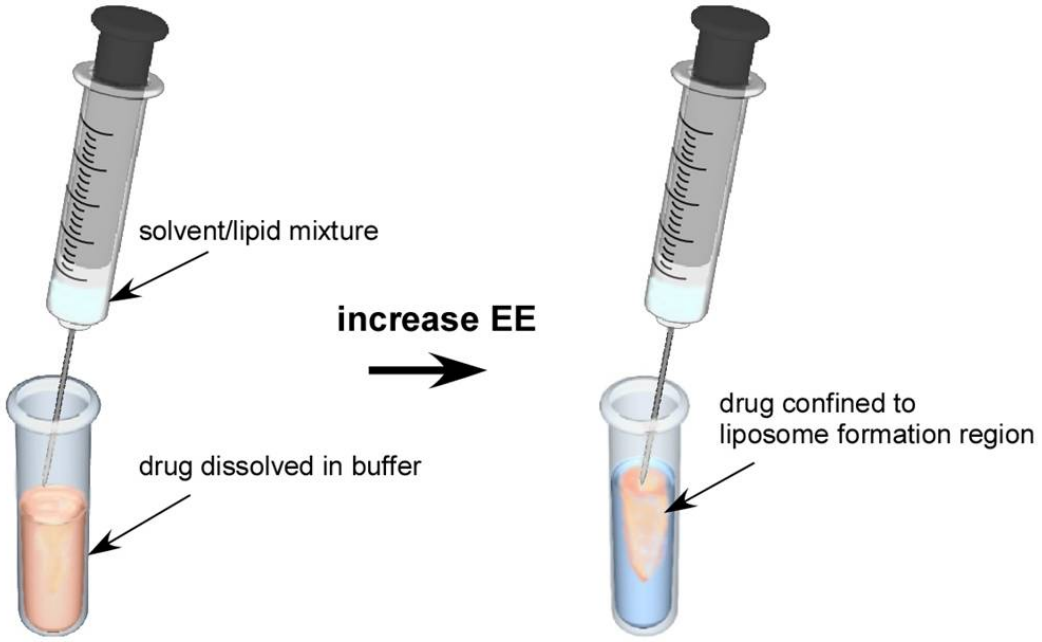

Figure 7 Schematic of drug encapsulation with standard alcohol injection and hypothetically increasing the encapsulation efficiency (E.E.) by confining the drug to the area where liposome formation occurs.

Confining a drug to the liposomes formation site as shown with the standard injection methods in Figure 7 is unfeasible. However, the MHF approach allows confining the drug to the immediate vicinity where lipids self-assemble into liposomes. This is shown in Figure 8 where the encapsulant carboxyfluorescein (CF) is confined to the liposome formation region, rather than throughout the entire aqueous fluid. This allows reducing the amount of non-encapsulated compound.

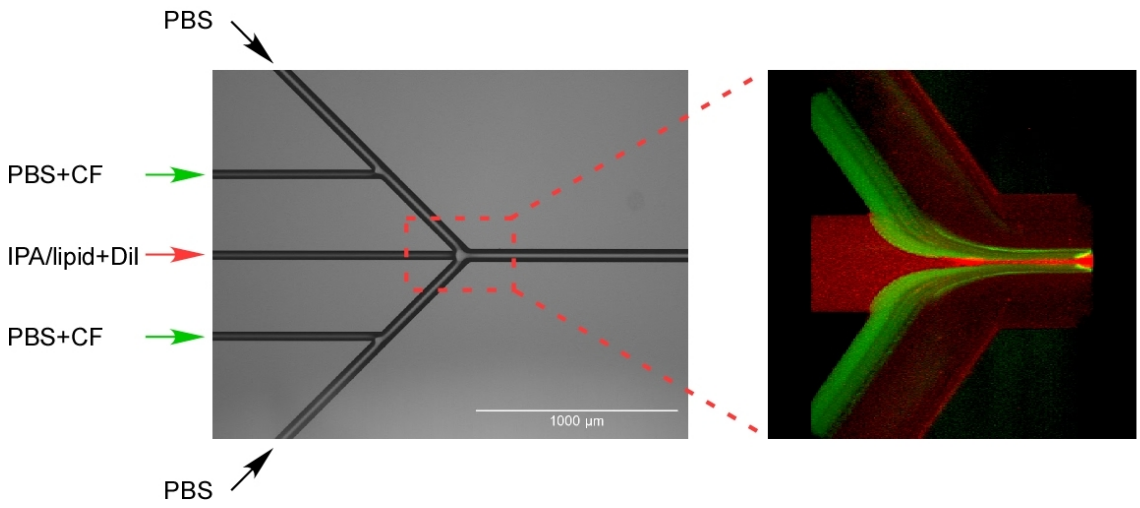

Figure 8 Micrograph of the multiple-inlet channel that allows confining the compound of interest to the immediate vicinity of liposome formation (left). 3D-confocal micrograph at an angle that shows the sheathing of green CF (the compound to be encapsulated) in PBS to the IPA/lipid solution (DiIC_{18} fluorophore is added to visualize the focusing). Transparent PBS is sheathed next to the CF containing PBS and fills the majority of the center channel.

2.3 Microfluidic Channel Design and Device Fabrication

Liposome formation *via* hydrodynamic focusing was investigated with three different microfluidic devices, as shown in Figure 9. A T-channel served as a proof of concept for liposome formation in microchannels. However, the T-channel design produces solid-liquid interactions of lipids at the channel wall in addition to liquid-liquid interactions between the buffer and the lipid solvent stream. In order to limit the lipid interactions to the liquid phase, the T-channel design was replaced soon after by a second design, the double-cross channel design, as shown in Figure 9a. In the double-cross channel design the solvent stream is sandwiched between two buffer streams minimizing lipid interaction at the wall during lipid self-assembly. The channel layout in Figure 9b includes multiple inlets to allow separate injection of a solute of interest to be encapsulated into liposomes through the two inner side channels. Figure 9c shows a single cross microchannel layout that has narrower channels compared to the previous two designs and plays an integral part in the investigation of the effect of channel dimensions on liposome formation. The multiple-inlet design and single cross design have microchannel with a higher aspect-ratio (ratio of channel depth to channel width) and a rectangular cross sectional area compared to the shallower trapezoidal channels of the double-cross design. The goal is to homogenize the 3-dimensional parabolic flow-profile across the depth of the channel.

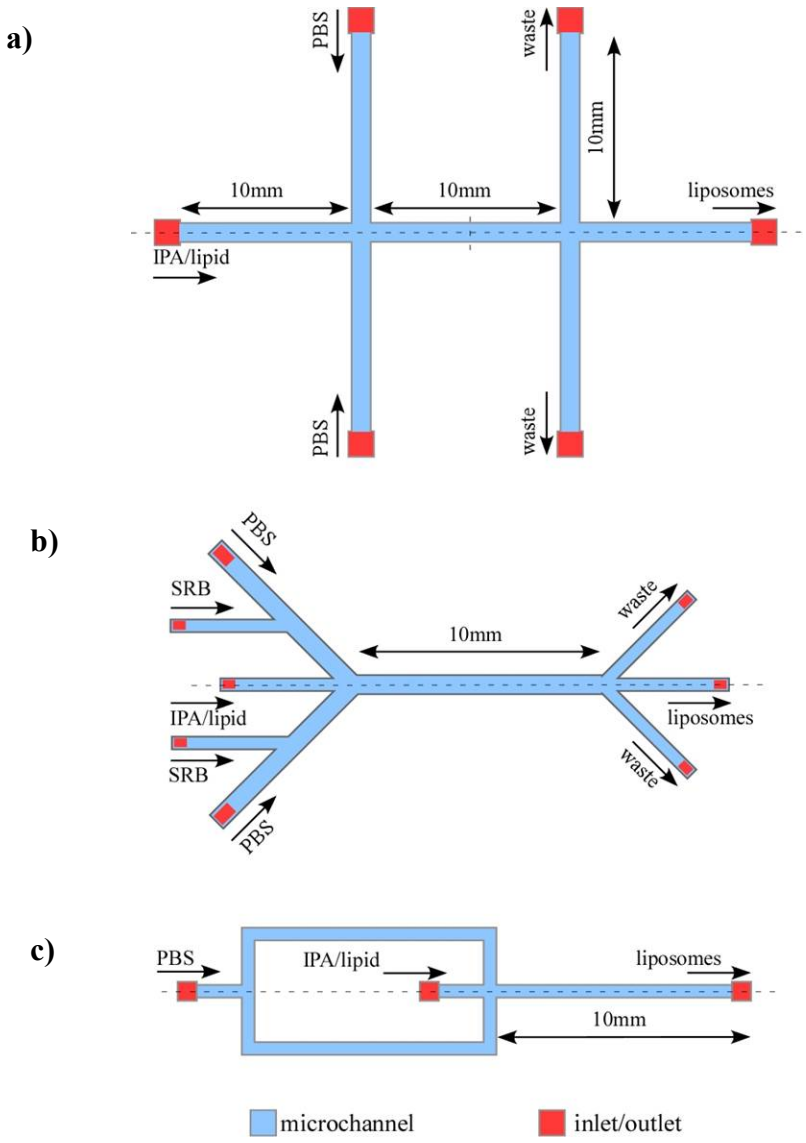

Figure 9 Shown are three microchannel designs applied for liposomes formation with MHF. (a) The double-cross design has a trapezoidal channel cross-section. The channels are 200 µm wide channels (on the top) and 40 µm deep. (b) The multiple-inlet design allows separate injection of an encapsulant. The channel cross-section area is rectangular. The channel width is 42 µm for the IPA/lipid, SRB, and three outlet channels and 65 µm for the PBS and mixing channel. All channels are either 100 µm or 120 µm deep. (c) A cross channel design with rectangular channel cross section. The channels are 10 µm wide and 36 µm deep.

Furthermore, in the multiple-inlet design, the fluid access holes at each channel terminus are confined within the microchannel; meaning the through-holes do not extend past the microchannel width (Figure 9b) in contrast to Figure 9a and Figure 9c where the access holes at the channel terminus are wider than the microchannel. Limiting the fluid access-holes to within the microchannel width reduces dead volume and vortices in the injection points. The three outlets in the double cross and multiple inlet designs serve the purpose of increasing the collected liposome concentration by removing excessive buffer through the two waste outlets.

The double cross-channel design is fabricated with an anisotropic wet-etching technique. The anisotropy of the wet-etching technique depends on the orientation of the silicon crystal structure in the silicon wafer. Due to this constraint, the channels must be aligned orthogonally to each other and the etched structures will be of rectangular geometry with respect to the surface, while the cross-sectional area will be trapezoidal or triangular, depending on the depth of the channel. The multiple inlet and single-cross design is fabricated with deep reactive ion-etching (DRIE).[72]

The microchannel layouts were etched into a silicon wafer (<100> orientation, 75 mm diameter 0.3 mm thickness, Nova Electronics Material Inc., TX). The silicon wafer is then anodically bonded to a borofloat glass wafer (BSG) to seal the microchannels. Fluidic connectors are glued to the backside of the silicon wafer to facilitate the injection of fluid with syringes through PEEK capillary tubing.

Figure 10 depicts the details of the fabrication process flow for the multiple-inlet channel designs. A silicon (Si) wafer is dipped into hydrofluoric (HF) acid to strip the native oxide layer, and subsequently dried on a hotplate for 5 min at 115 C.

Hexamethyldisiloxane (HMDS) is spin-coated at 2500 rpm for 50 s onto the frontside of a Si-wafer to improve the adhesion of a 3 μm thick layer of positive tone photo resist (Shipley SPR-220-3; Rohm and Haas, Marlborough, MA, USA), which is subsequently spin-coated at 2500 rpm for 45 s. A prebake on a hotplate at 115 C for 90 s solidifies the resist. The channel layout is transferred lithographically in hard-contact mode with a patterned chrom/glass mask and a mask aligner (MA6; Suss MicroTec, Waterbury, VT, USA) onto the photoresist. The photoresist is exposed to UV light (i-line) at 21 mW/cm^2 for 30 s followed by a postexposure-bake on a hotplate at 115 C for 90 s. The photoresist is subsequently developed for approximately 1 min in a basic MF351 developer. A oxidized Si-wafer is spin-coated with SPR-220-3 and bonded to the first Si-wafer. Both wafers are hard-baked on a hotplate at 115 C for 30 min. The channels are etched 100 μm to 120 μm deep with DRIE.[73] After the microchannels are etched into the front side of the Si-wafer, the wafers are separated. The microfluidic through-holes are etched into the backside of the Si-wafer in the same manner. After the through-holes are etched into the Si-wafer, the wafer is striped again of native oxide in buffered oxide etch (6:1 HF).

Prior to bonding, the glass wafer (75 mm diameter, 0.1 mm thick, Corning Pyrex 7740) and the silicon wafer are thoroughly cleaned and dehydrated to ensure conformal contact between the wafers. Cleaning is accomplished by dipping the oxidized silicon wafers in RCA1 (NH_4OH, H_2O_2, H_2O; 1:1:5) at 80 C for 10 min to remove organic compounds, followed by a short dip into 2% HF and immersing for another 10 min into 80 C RCA2 (HCl, H_2O_2, H_2O; 1:1:5) to remove remaining metal and alkali impurities. The wafers are then anodically bonded at 400 ºC for 60 min with a ramp rate of

25 ºC min^{-1} at a bonding voltage of 800 V. The glass is connected to the negative electrode while the silicon is connected to the positive electrode of the power supply, thus the sodium ions drift towards the negative electrode creating a very large electric field at the silicon/glass interface, which pulls the two surfaces together facilitating the bonding of the two surfaces.

Fluidic nanoports (F-124S, Upchurch Scientific, USA) connect external capillary tubing to the microchannel network. These ports minimize fluid dead volume between the external capillary tubing and the microfluidic device. The nanoports are bonded to the backside of the silicon wafer using vendor supplied adhesive rings according to their instructions. Capillary tubes deliver the fluid from glass syringes to the microchannel network.

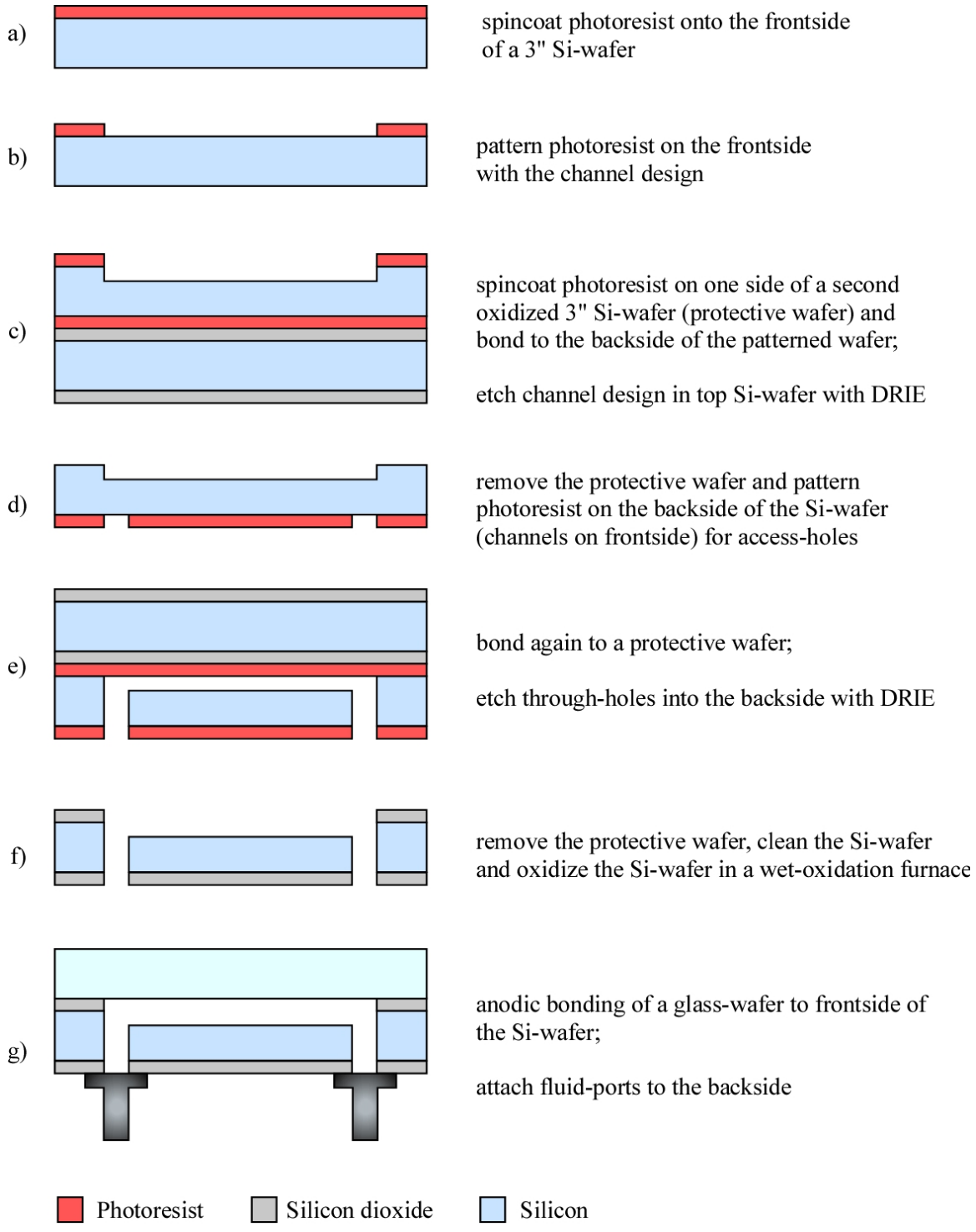

Figure 10 Schematic of the fabrication process for the multiple-inlet design.

2.3 Characterization of Liposome Size, Size Distribution, and Encapsulation

Light scattering is commonly used to determine the size and size distribution of colloidal systems. As light interacts with matter the electrical field of the electromagnetic wave separates charges in the particle. The amount of charge separation depends on the polarizability of the particle itself. If the wavelength of the light is much longer than the physical dimensions of the particle the separated charges produce a dipole field. The oscillating electric field of the light creates an oscillating dipole in the particle, which then reradiates the light predominantly in the plane perpendicular to the incident polarized light. Depending on the size of the particle the perpendicular scattering is characterized by an angular scattering dependence.[74] When the particles are below a critical physical dimension compared to the wavelength of the oscillating field, its scattering is nearly independent of the angle perpendicular to the incident light. At a wavelength of about 690 nm of the incident light, as in the light scattering instrument utilized, isotropic scattering occurs at particle sizes of less than 10 nm radius and anisotropic scattering occurs with larger radii; this allows size characterization of small unilamellar vesicles (SUVs) with diameters of about 20 nm to 25 nm. Larger particles scatter more light and show a larger angular dependence of scattered light than smaller particles. Analysis of the particle scattering pattern and intensity allows for determination of particle size. To obtain an accurate characterization of the liposome size distribution it is necessary to fractionate liposomes. Asymmetric flow field-flow fractionation (AF^4), a type of liquid chromatography that does not use a stationary phase, separates particles by a cross-flow field in an otherwise laminar flow. It allows the separation of particles with sizes ranging from 1 nm to several 1000 nm encompassing the separation of micelles, liposomes, emulsions, viruses, bacteria, cells, proteins, glyco-

proteins, and protein-complexes.[75] The combination of AF^4, multi-angle laser light scattering (MALLS), and quasi elastic light scattering (QELS) allows for determination of liposome size distributions with very high resolution.

Other commonly used techniques to measure liposome size and size distribution include transmission electron microscopy (TEM) and atomic force microscopy (AFM). TEM measurements of liposomes often require complicated sample preparation and can induce artifacts such as shrinkage and shape distortion as liposomes are removed from their native environment. The structural information about the morphology is very good and allows very precise particle characterization. Nevertheless, TEM measurements are very time consuming if one wants to obtain statistically meaningful and representative size distributions of a vesicle population and hence TEM is not amenable to being a routine measurement.[76] On the other hand AFM, which was developed in 1986, allows for easy and fast sample preparation while still allowing the vesicles to remain preserved in their native aqueous environment. The ability of the AFM to operate in a non-contact mode prevents deformation of soft-matter particles such as liposomes. Nevertheless, even if using AFM in non-contact mode and operating in aqueous solution the measurement requires that the liposomes are deposited on substrate such as silicon or mica. Ruozi et al. reported recently that already 10 minutes after deposition liposomes showed a progressive tendency to turn into asymmetrical and flattened structures often describes as planar vesicles.[77] This tendency to change their structure varies with the composition of the liposomes. While both AFM and TEM provide excellent information about the morphology in respect to lamellarity and nanometer-scale resolution on vesicles, they require meticulous sample preparation to minimize artifacts of the vesicle

size and shape. The continuous improvement of AFM and TEM measurement procedures in the field of soft-matter particles will eventually provide a very important tool to better characterize liposomes for drug delivery applications.

Information about the bilayer structure can also be obtained with small angle neutron scattering (SANS), small angle X-ray scattering (SAXS) or nuclear magnetic resonance (NMR) spectroscopy.[76] SAXS and SANS both belong to scattering technologies just as light scattering but while light and X-rays are both scattered by electrons surrounding the atomic nuclei, neutron are scattered by the nucleus itself. The lower energy of the neutrons in SANS measurements compared to that of X-ray photons in SAXS makes the former more suitable for the study of sensitive biological samples such as lipid vesicles.[78] In the case of SAXS Bouwstra et al.[79] reported that the scattering curve changes dramatically when a small fraction of multilamellar vesicles is present in a sample of mostly unilamellar vesicles. This could potentially lead to erroneous interpretations about the overall lamellarity of the vesicle population. In the ^{31}P NMR technique Mn^{2+}, which interacts with the negatively charged phosphate groups of phospholipids, is added to a liposome sample to quench the ^{31}P NMR signal from phospholipids on the exterior of the outermost phospholipids bilayer. The lamellarity can be subsequently determined from the signal ratio before and after Mn^{2+} addition to the liposome sample. However, this technique is quite sensitive to Mn^{2+} concentrations and buffer concentrations and the type of lipids used. While SAXS, SANS, and NMR are certainly important and mature techniques to analyze the lamellar structure of vesicles, the sample preparation and costs that are often associated with these techniques but also the required vesicle concentrations that are much higher than obtained with the

microfluidic focusing method make QELS and MALLS the preferred method to characterize the size distribution of submicrometer-scale liposomes. Additionally, cryogenic-TEM (cryo-TEM) is applied to investigate the lamellarity of liposomes prepared with the microfluidic hydrodynamic focusing method. Here, a liposome sample is rapidly frozen in liquid ethane cooled to -180 ºC by liquid nitrogen. The rapid freezing prevents ice-crystal formation which would otherwise result in the destruction of the liposomes.

The common goal of drug delivery systems (DDSs) is to achieve a very high encapsulation efficiency and reduce the amount of solute waste that has to be preprocessed for subsequent use. The number of molecules encapsulated within liposomes is analyzed with fluorescence cumulant analysis (FCA).[80] FCA is a modification of fluorescence correlation spectroscopy (FCS). The latter is a widely used and powerful tool that measures temporal fluctuations of the fluorescence. The major drawback of FCS is its insensitivity to discriminate between similar sized particles. FCA resolves heterogeneous samples based on differences in fluorescent intensity instead of temporal fluctuations as in FCS. FCA exploits information from higher moment analysis of the probability distribution of photon counts.[81] It therefore distinguishes molecular species by difference in their fluorescent intensity and not their diffusion coefficients. Combining the results from FCA with the liposome size distribution obtained from light scattering provides information about the average fluorescence or number of entrapped molecules in a liposome.

Chapter 3: Microfluidic Directed Liposome Formation of Controlled Size

3.1 Introduction

A new method to tailor liposome size distributions in a microfluidic format is presented. A method is described to engineer liposomes of a particular size distribution by changing the flow conditions in a microfluidic channel, obviating the need for post-processing. A stream of lipids dissolved in IPA is hydrodynamically focused between two sheathed aqueous streams in a microfluidic channel. The laminar flow in the microchannel enables controlled diffusive mixing at the two liquid interfaces where the lipids self-assemble into vesicles. The liposomes formed by this self-assembly process are characterized using asymmetric flow field-flow fractionation (AF^4) combined with quasi-elastic light scattering (QELS) and multi-angle laser light scattering (MALLS). It is observed that the vesicle size and size distribution are tunable over an average diameter from approximately 50 nm to 150 nm by adjusting the ratio of the buffer-to-alcohol volumetric flow rate ratio (FRR). Furthermore, it is observed that liposome formation depends more strongly on the focused alcohol stream width and its diffusive mixing with the aqueous stream than on the shear forces at the solvent-buffer interface.

3.2 Description of Experimental Procedures

3.2.1 Device Fabrication

Microfluidic channels are fabricated in a silicon wafer (76.2 mm (3 in.) diameter, 305 μm to 355 μm thick, Nova Electronics Materials, Inc., Carrollton, TX) with deep reactive ion etching (DRIE) using the Bosch process and sealed by anodic bonding to a borosilicate glass (BSG) wafer (75 mm diameter, 0.1 mm thick, Corning Pyrex 7740), as

described in the previous chapter. The microchannels in the multiple-inlet design (Figure 9b) have a rectangular cross section with a depth of 100 µm and a width of either 42 µm (center inlet channel) or 65 µm (side channel and mixing channel). A schematic of the assembled wafers and fluid-ports is depicted in Figure 11. PEEK capillary tubes (Upchurch Scientific, Oak Harbor, WA) with an inner diameter of 254 µm (0.01 in.) connect the Nanoports to a syringe. A 0.02 µm filter (Anatop, Whatman, NJ) is placed on the syringes to ensure that all fluids introduced to the microchannel network are dust-free to prevent clogging of the channels. Fluidic reagents are introduced to the microfluidic network from glass gastight syringes (Hamilton, Reno, NV) by syringe pumps (model PHD2000, Harvard Apparatus Inc., Holliston, MA).

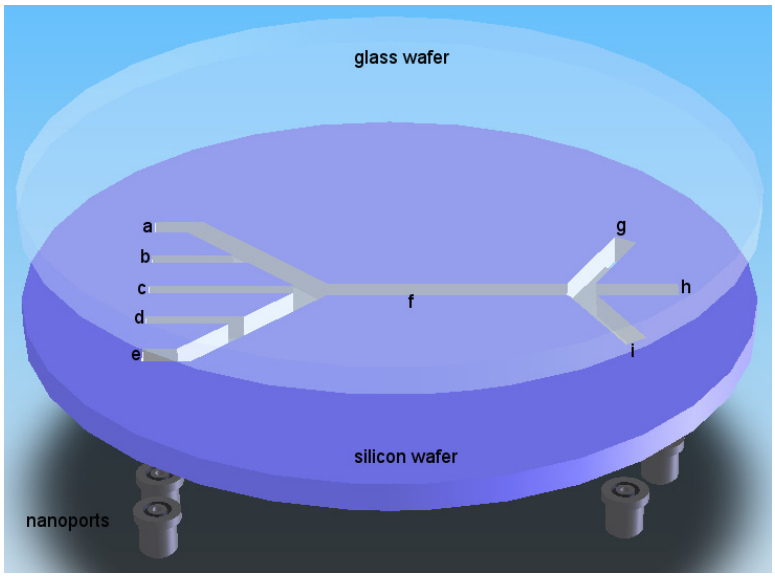

Figure 11 Schematic of the microfluidic device. Exploded view showing the fluid ports attached to the backside of the silicon wafer, the channel network etched into silicon with five inlet channels (a-e) on the left and three outlet channels (g-i) on the right, and the sealing with a glass wafer *via* anodic bonding.

3.2.2 Materials

Saturated 1,2-Dimyristoyl-sn-Glycero-3-Phosphocholine (DMPC), cholesterol (both Avanti Polar Lipids Inc., Alabaster, AL), and dihexadecyl phosphate (DCP) (Sigma-Aldrich) in a molar ratio of 5:4:1 are dissolved in dry chloroform (Mallinckrodt Baker Inc., Phillipsburg, NJ). The chloroform solvent is evaporated under a stream of nitrogen at room temperature to form a dry lipid film on the bottom of a scintillation vial. The scintillation vial is subsequently placed into a vacuum desiccator for at least 24 h to ensure complete solvent removal. The dried lipid mixture is resolubilized in dry IPA at a 5 mmol/L concentration of total lipid. Phosphate buffered saline (PBS) solution (10 mmol/L phosphate, 2.7 mmol/L potassium chloride, 138 mmol/L sodium chloride, pH 7.4, 3 mmol/L sodium azide) is used as a hydration buffer.

3.2.3 Liposome Formation

Unilamellar liposomes are prepared by injecting a lipid mixture dissolved in IPA into the center channel of the microfluidic network shown in Figure 11. PBS is injected into the oblique side channels intersecting with the center channel. The flow rate ratio (FRR), defined as buffer volumetric flow rate (Q_B) to IPA volumetric flow rate (Q_S), is varied from 10 to 60. Liposome formation at different shear forces is investigated by changing the total volumetric flow rate (Q_t) from 31 μL/min to 186 μL/min maintaining a constant FRR of 30.

3.2.4 Microscopic Imaging

The hydrodynamically focused flow in the microfluidic channel is imaged with a confocal laser-scanning microscope (LSM 510 Meta, Carl Zeiss, Thornwood, NY) with a 30 mW HeNe laser (excitation, 543 nm; power output, 18 %; objective LD-Achroplan, 20x/0.4; detector gain, 468; amplifier gain, 1.00 V; amplifier offset, 0.1 V; filter, LP 560; beamsplitter, MBS HFT 488/543; 12-bit image resolution; 1.6 µs pixel time; 94 µm pinhole). Vendor supplied image processing software is used (Carl Zeiss, Thornwood, NY). The alcohol concentration is determined by measuring the fluorescent intensity of sulforhodamine B (SRB) as a function of IPA concentration.

3.2.5 Cryogenic Transmission Electron Microscopy

Cryogenic transmission electron microscopy (cryo-TEM) involves the examination of a vitrified hydrated sample directly on a cryo stage in the TEM. Five microliter drops of liposome suspensions were placed on 1000-mesh copper electron microscope (EM) grid. Specimens were frozen by clamping each grid into spring-loaded forceps of a Leica KF80 freezing machine. The grid was blotted with filter paper to leave a thin film of liposome suspension just prior to plunging the grid into liquid ethane cooled to -180 ºC by liquid nitrogen. The frozen grid was then loaded under liquid nitrogen into a Gatan model 626 specimen holder and cryotransferred into an FEI CM120 transmission electron microscope (Philips) equipped with Gatan anticontaminator blades. Suitably thin specimen regions were imaged at a beam voltage of 120 kV and at an electron dose of less than 1000 electrons per square nanometer using a Gatan GIF100 post-column imaging filter equipped with a 1024x1024 pixel cooled CCD camera.

Contrast was enhanced by energy-filtering the transmitted electrons and by underfocusing the objective lens to about 500 nm.

3.2.6 Light Scattering and AF^4 Procedure

High-resolution size-based separation of the liposome population is carried out using asymmetric flow field-flow fractionation (AF^4) with multi-angle laser light scattering (MALLS) and quasi-elastic light scattering (QELS) detection and characterization (model DAWN EOS and QELS, Wyatt Technology, Santa Barbara, CA). A vendor-supplied spacer (250 μm thickness) is used to define the flow channel thickness with a 10 kg/mol MWCO (molecular weight cut-off) regenerated cellulose membrane (Millipore, Bedford, MA) for the cross-flow partition. PBS is used as the carrier liquid in the particle size separation. The flow is controlled with vendor-supplied software (Eclipse 2, Wyatt Technology, Santa Barbara, CA). A sample volume of 100 μL is injected with an auto-sampler at a flow rate of 0.2 μL/min and focused into a thin band in the separation flow-channel at a flowrate of 3 mL/min for 4 min. The injection step is followed by a second focusing step at 3 mL/min for 3 min. The cross-flow is ramped linearly from 3 mL/min to 0 mL/min over 60 min while eluting the separated particles at 0.8 mL/min. The radii of the eluted vesicle fractions are monitored using MALLS and QELS detection with data processing, using software supplied by the vendor (ASTRA, Wyatt Technology, Santa Barbara, CA). MALLS is measured at 15 angles simultaneously. The liposome sample is measured at 1 s and 5 s intervals for the MALLS and QELS, respectively. The autocorrelation function (ACF) of the QELS is fitted to a single-mode exponential decay model to determine the hydrodynamic radius

(R_h). A coated sphere model (*i.e.*, a spherical structure with two radial regions of differing refractive index) showing good fit with the MALLS data is applied for size analysis of the geometric radius (R_g) of the fractionated samples.

3.3 Results and Discussion

Hydrodynamic focusing in a microfluidic device allows for fast and controlled mixing of miscible liquids with the benefit of reduced sample consumption. In the microfluidic device presented in Figure 11, four aqueous buffer streams (channels a, b, d, and e) hydrodynamically focus a lipid tincture entering through the center channel (channel c) at the cross junction. Hydrodynamic focusing reduces the center channel stream width and consequently the diffusion length for liquids to mix. The sample stream injected into channel c is focused into a thin sheet. Simple mass flow balance within the microchannel can provide a theoretical model to estimate the absolute minimum continuum width of the focused sample stream

$$Q_S = v_f \cdot w_{fs} \cdot h = v_c \cdot D_c \cdot h \tag{3.1}$$

assuming a parabolic flow profile in the rectangular channel with

$$v_f = \frac{3}{2} \cdot v_c \tag{3.2}$$

so that

$$w_{fs} = \frac{2 \cdot D_f}{3 \cdot \left(1 + \frac{Q_B}{Q_S}\right)}, \tag{3.3}$$

where w_{fs} is the stream width of the focused sample stream in the center of channel f, Q_S and Q_B are lipid mixture and buffer volumetric flow rate, v_c and is the average flow

velocities of channel c and v_f the maximum flow velocity in the center of channel f, D_c and D_f are the widths of channels c and f, respectively, and h is the channel depth, which is constant for the entire microchannel network. The estimated focused stream width, w_{fs}, in eq. 3.3 idealizes the otherwise complicated system by assumimg that (1) all liquids entering the channels have the same density, (2) all liquids have a parabolic flow-profile across the width of the channel, and (3) diffusive mixing is negligible. It can be seen from eq. 3.3 that w_{fs} than only depends on the microchannel geometry and the buffer-to-solvent flow rate ratio (FRR). Because eq.3.3 does not consider molecular diffusion of IPA into PBS it really only provides an estimate of the focused sample streamwidth within the first 100 μm of the entrance of channel f of the hydrodynamically focused stream at low FRRs. The high flow velocities result in sub-millisecond residence time over a distance of 100 μm where diffusive spreading of the focused stream is minimal due to the short convective residence time. Although diffusion is neglected in eq. 3.3, it gives a rough estimate of the width of the focused stream in the entrance region of channel f. The estimated stream width roughly agrees with the measured stream width from Figure 12 for FRRs of 5 and 10. At higher FRRs IPA diffusion becomes substantial compared to the estimated stream width and diffusion must be considered for accurate streamwidth estimates. Figure 12 shows a confocal microscope image sequence of the IPA concentration across and along the center channel as a function of varying FRRs increasing from 5 (left) to 35 (right) in increments of 5.

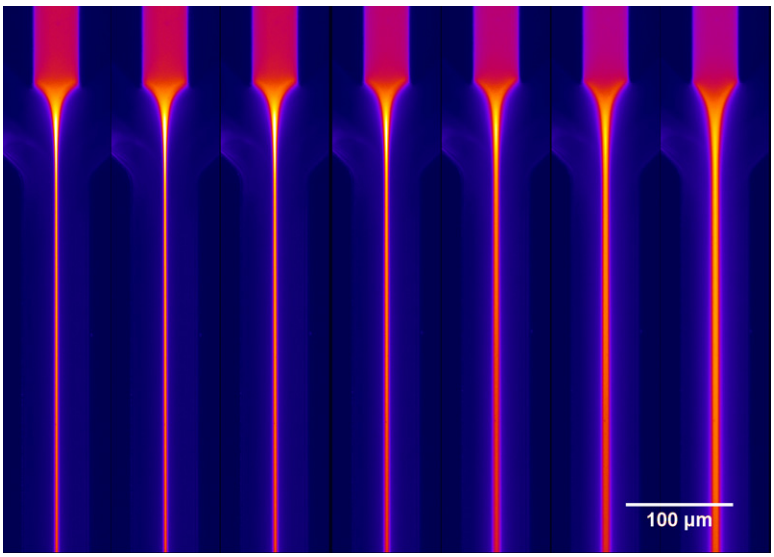

Figure 12 False color confocal microscope images showing hydrodynamic focusing of an IPA stream by two adjacent aqueous buffer streams (not visible). The focused IPA stream, containing sulforhodamine B for visualizing purposes, enters from the top. Shown are 7 different FRRs, increasing from 5 to 35 in increments of 5 from left to right at a constant Q_t of 100 µL/min.

As the FRR increases, the alcohol stream width decreases. A smaller alcohol stream width results in a shorter diffusion length, and therefore the IPA concentration decreases more rapidly. The hydrodynamic focusing process due to extensional flow is completed once the focused stream enters the mixing channel (channel f). While mixing in the focusing region is due to both convection and diffusion, in the mixing channel it is dominated by molecular diffusion.

Laminar flow conditions in the channel allow for mixing that is based entirely on molecular diffusion in a direction normal to liquid flow streamlines. At a critical alcohol-to-water ratio the lipid monomers in the alcohol stream become insoluble and spontaneously self-assemble into closed spherical structures concomitantly sequestering

the surrounding fluid. A smaller w_{fs} results in reduced diffusion lengths for mixing between the alcohol center stream and aqueous side stream, thereby reducing the distance downstream of the focusing region to reach the critical alcohol concentration where lipids spontaneously self-assemble into spherical vesicles. The effects of Q_t and FRR between sheath and sample flow on liposome formation are investigated using MALLS and QELS combined with AF^4.

3.3.1 Influence of Q_t and Shear Forces on Liposomes Formation

Figure 13 shows the liposome size distributions for six different Q_ts ranging from 30 μL/min (Re ≈ 6) to 180 μL/min (Re ≈ 6) at a constant FRR of 30. At a constant FRR, the width of the focused lipid/alcohol stream remains constant because the liquid is incompressible, and therefore the stream width, does not depend on the magnitude of the inlet and side channel volumetric flow rates but on the FRR. By maintaining a constant FRR and increasing the flow rates, the streamwidth and dilution rate remain constant; however, the shear forces at the interface of the two fluids increase. As Q_t increases 6-fold from 30 μL/min to 180 μL/min, the eluted liposomes are of approximately the same size and size distribution with a number weighted average geometric radius (R_g) of 29 nm and a distribution width of ±4 nm (≈3σ), as shown in Figure 13. This indicates that the absolute magnitude of the shear forces between the parallel layered streams has no significant impact on liposome size or size distribution. The increased noise in the data at a geometric radius less than 27 nm is due to lower concentrations and smaller sizes of particles, yielding a lower scattering intensity of the molecular solution.

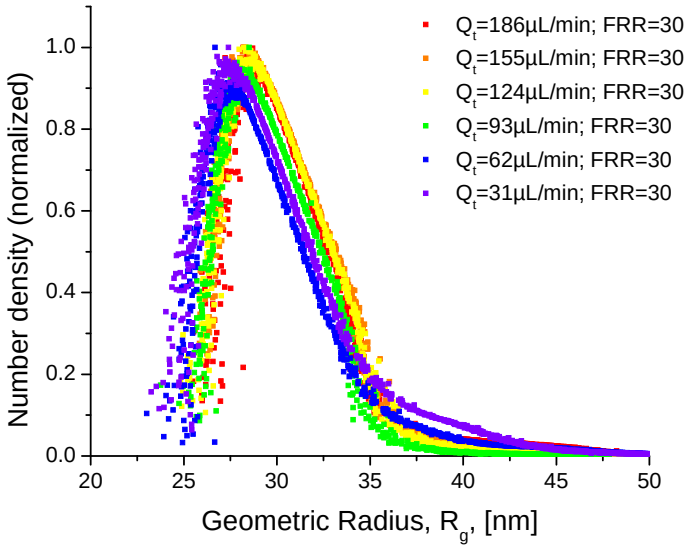

Figure 13 Liposome size and size distribution at a constant FRR of 30 and different Q_ts. Increasing Q_t 6-fold does not change the size distribution significantly. This indicates that the magnitude of shear stresses during liposome self-assembly has no or only little influence on the liposome size distribution.

3.3.2 Influence of FRR on Liposomes Formation

Figure 14 and Figure 15 show liposome size distribution at different FRRs. As the FRR decreases the mean liposome size increases and the size distribution broadens. One possible mechanism to explain this phenomenon is as follows: assuming that the lipids are homogeneously distributed in the alcohol stream, when the alcohol stream first comes into contact with the aqueous streams, the lipids at that interface will quickly reach the critical alcohol concentration and self-assemble into liposomes. The resulting liposomes have a markedly decreased diffusion coefficient and will convect along the stream lines of the fluid flow. It is then possible that as the alcohol continues to diffuse, the alcohol concentration will increase in a direction normal to the streamlines. If enough

alcohol is in the common alcohol-aqueous stream (*i.e.*, the alcohol portion of the stream is wide enough), it will cause the local alcohol concentration around the liposomes, that were formed at the initial interface, to increase above the critical concentration for liposome formation and the liposomes to partially disassemble. As the two streams continue to mix, the alcohol concentration near the initially formed liposomes will again decrease below the critical concentration, causing the liposome to reassemble. As the FRR decreases, the amount of alcohol introduced into the system and the alcohol stream width increase, causing the alcohol concentration to remain above the critical alcohol concentration for a longer length of the channel, and the magnitude of this phenomenon will increase. In contrast, as the FRR increases, the amount of alcohol in the system decreases, and fewer liposomes will experience alcohol concentrations high enough to induce this disassembly-reassembly phenomenon. Further increases in FRR lead to smaller changes in the stream width and the size and size distribution asymptotically approach limits, which depend on the maximum focusing of the center stream by the four buffer streams.

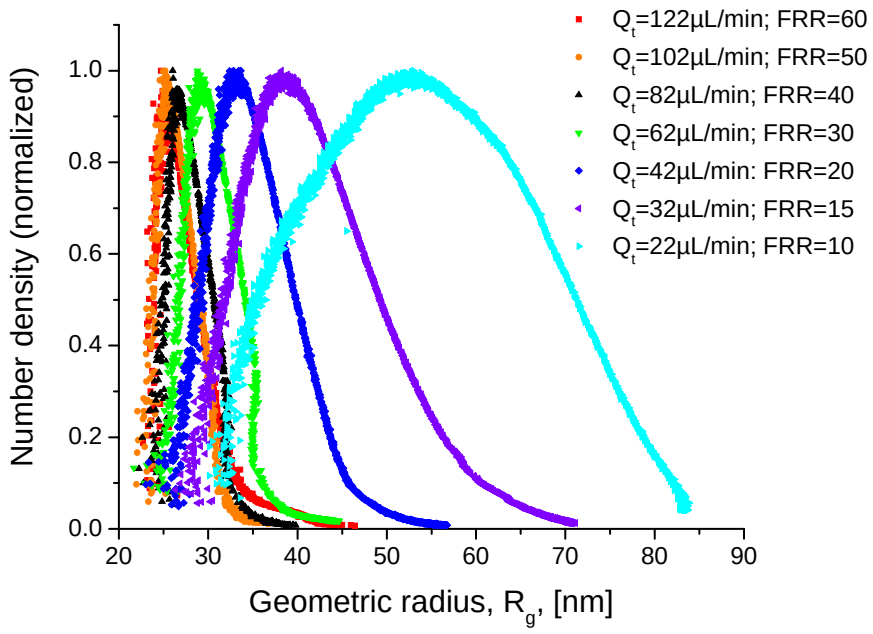

Figure 14 Liposome size distribution for different FRRs. Increasing FRR 6-fold reduces the liposome radius from approximately 55 nm to 25 nm and the size distribution from ±25 nm to ±5 nm (≈3σ).

The QELS measurements of the hydrodynamic radii of the liposomes produced at different FRRs as a function of time as the liposomes elute from the AF^4 channel is presented in Figure 15. QELS allows determining the diffusion coefficient of particles through the autocorrelation of its time-dependent fluctuations of scattered light. Typically, this is transformed into R_h through the Stoke-Einstein relation, where R_h represents the radius of a solid sphere that has the same diffusion coefficient as the measured particles. Measurement of R_h with QELS and R_g with MALLS allows for additional compositional characterization of the liposomes with respect to lamellarity.

From the data observed for R_h and R_g, it can be concluded that the liposomes are predominantly unilamellar.

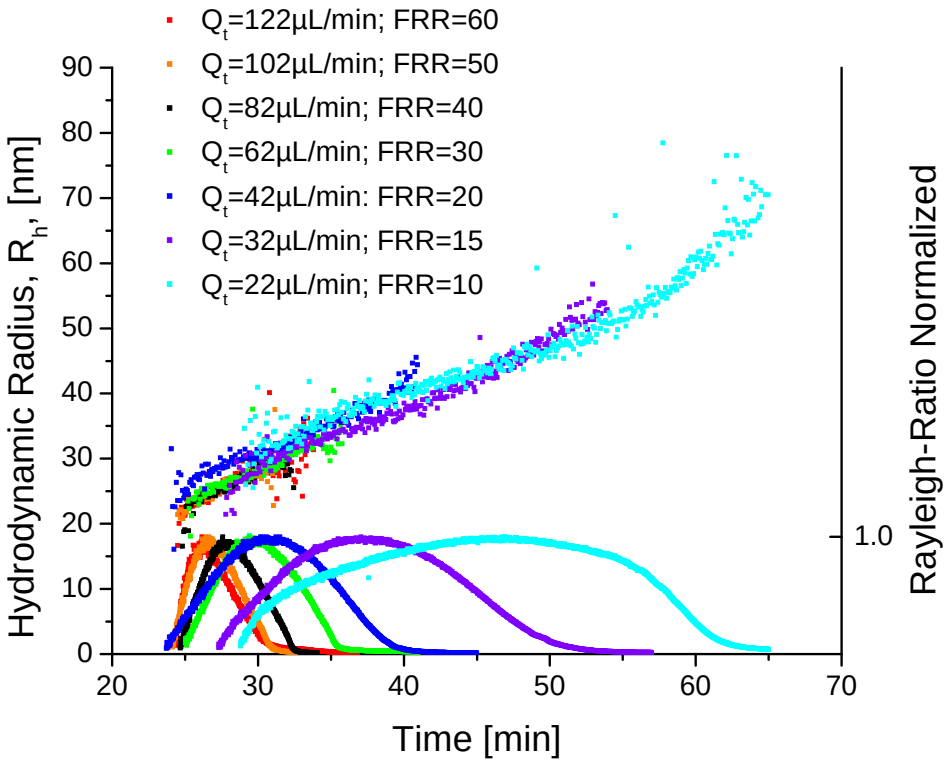

Figure 15 QELS measurements of the hydrodynamic radius R_h of liposomes at different FRRs as a function of time. A low FRR results in a rather broad liposome distribution with R_h varying between 30 nm and 70 nm. As the FRR increases (30 and higher) the average R_h decreases and the liposome size distribution becomes narrower with R_h varying between 22 nm and 27 nm. The excess Rayleigh scattering ratio of the liposomes which depends on the number of liposomes and liposome size is shown on the right axis. The Rayleigh-ratio or excess Rayleigh scattering is the excess of scattered light intensity of the liposome suspension above that scattered by the solvent itself.

Figure 16 shows a cryo-TEM image of approximately 100 nm diameter liposomes. Cryo-TEM allows studying the shape, size, and morphology of the vesicles. As can be seen in Figure 16 the larger vesicles prepared with microfluidic hydrodynamic focusing appear to be unilamellar which is in agreement with the light scattering data. However, it can also be seen in Figure 16 that the vesicles are not perfectly spherical, which is most likely due to the liposome sample preparation for the cryo-TEM measurements.

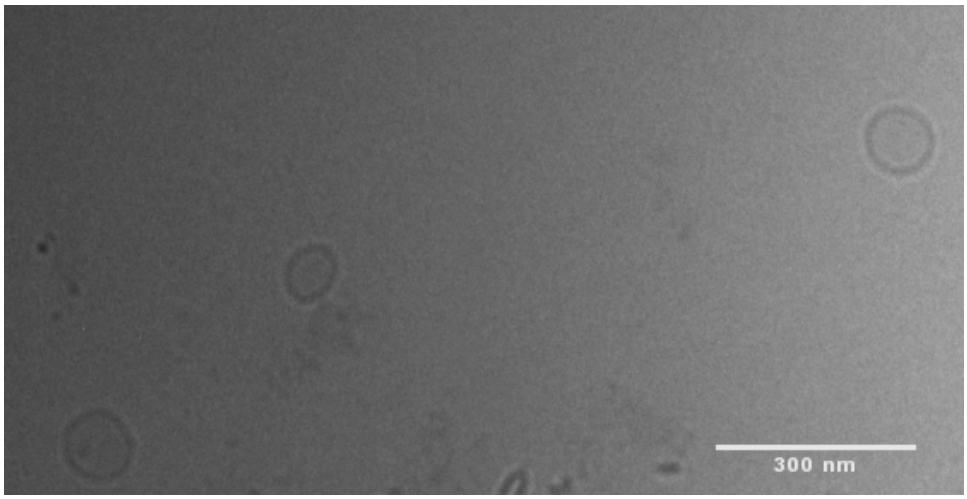

Figure 16 Cryo-TEM of unilamellar liposomes at 120 kV beam voltage and less than 1000 electrons per square nanometer electron dose. The image shows unilamellar liposomes produced by the microfluidic hydrodynamic focusing method.

3.4 Summary

The creation of liposomes using microfluidic techniques has been demonstrated to produce narrow liposome size distributions. The average liposome diameter can be controlled by adjusting the fluid flow rates of alcohol and buffer in the microfluidic network. Microfluidics allows for precise control of mixing over micrometer length-scales. Decreasing the sample streamwidth to micrometer length-scales allows for controlled and reproducible physicochemical conditions across the streamwidth, especially compared to more traditional bulk-phase preparation techniques (*i.e.*, test tubes and beakers). The laminar flow and precise fluidic control in a microchannel enables reproducible flow-fields for the self-assembly of lipids into liposomes in the sheathed flow-field. The lipid self-assembly strategy described here, could potentially open applications for on-demand liposome mediated delivery of point-of-care personalized therapeutics; thus, liposome-mediated drug delivery could eliminate procedure dependent liposome shelf-life limitations.

Chapter 4: Geometric and Hydrodynamic Aspects of Liposome Formation

The previous chapter showed that liposome size distributions can be controlled by varying the FRR between the solvent and aqueous buffer phase. Discussions at conferences often raised the question if geometric parameters of the microchannel could possibly influence the liposome size distribution. This chapter will show that similar liposome size distribution can be obtained from different microchannel geometries. Especially, the investigation of the microchannel geometry provided more detail and helped to further elucidate the liposome formation process. This chapter also describes that reducing the microchannel geometry provides a means to increase the liposome concentration without affecting the final size distribution. This is especially interesting in regards to increasing the encapsulation efficiency of compounds within liposomes.

4.1 Introduction

A more thorough investigation of microfluidic hydrodynamic focusing (MHF) shows that the vesicle size distribution is not only a function of the FRR as previously reported[47,48] but a rather complex function of multiple parameters. While the FRR suffices to describe vesicle formation in one channel size and at a single flow rate, it is not predicable between different mixing channel designs and flow rates. This chapter shows that the vesicle formation process depends strongly on the geometric parameters of the microchannel design (*i.e.* channel width and cross sectional area) and hydrodynamic parameters (*i.e.* FRR and flow velocity). The numerical simulation section summarizes the results for vesicle formation based on the concept of two mixing regions; convective-diffusive mixing in the focusing or transition region and diffusive mixing in the outlet or mixing channel.

It will be shown that microchannels with a smaller cross sectional area produce comparable average vesicle diameters at lower FRRs than wider microchannels. The findings indicate that neither the focused streamwidth nor the final alcohol concentration solely determine the vesicle formation process. In certain flow regimes the flow velocity provides an additional parameter to modulate the vesicle diameter distribution. Numerical simulations of the experimental parameters that influence the mixing of alcohol with water show that liposome formation with MHF, though relatively simple experimentally implemented, is a complex system of mass and momentum transfer as well as self-assembly. Additionally, batch-to-batch consistency is evaluated, which turns out to be another hallmark of the MHF method and strengthens its future applicability in drug delivery and point-of-care applications

4.1 Description of Experimental Procedures

4.1.1 Device Fabrication

Two different channel intersection layouts with varying microchannel widths are prepared. The first design consists of a double-cross intersection in which two oblique side channels intersect with the corresponding end of the central channel at an angle of 45 º. The slanted inlet configuration is fabricated as described in the previous chapter. The microchannels have rectangular cross-sections as a result of the chosen dry etching technique (DRIE) with a depth of 120 μm, a center inlet width of 42 μm, and mixing channel width of 65 μm. The side channel width is either 65 μm (Figure 17a) or 42 μm (Figure 17b). The second design consists of two orthogonally intersecting microchannels with a rectangular cross section with a depth of 36 μm and a width of 10 μm (Figure 17c). The latter design is fabricated in a similar manner as previously described with the microchannels on one side of the silicon wafer and the fluid access ports on the opposite side. Fluidic reagents are introduced into the central microchannel using a gastight glass syringe (Hamilton, Reno, NV) and into the oblique side microchannels with standard syringes (BD, Franklin Lakes, NJ) by syringe pumps (model PHD2000, Harvard Apparatus Inc., Holliston, MA). All fluids are filtered with 0.2 μm pore sized filters (Anatop, Whatman, NJ) to prevent particulate contamination and clogging of the microfluidic device.

a)

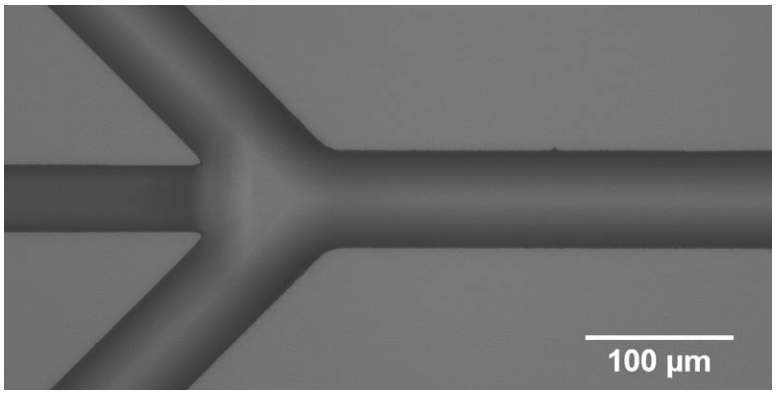

b)

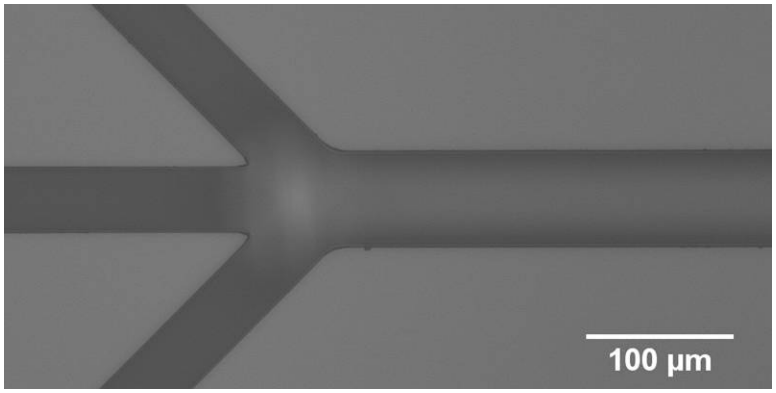

c)

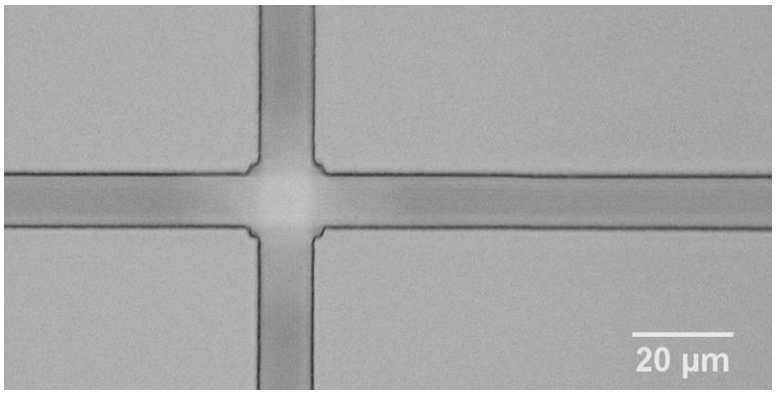

Figure 17 Microscope images of the different channel layouts. (a,b) All micro-channels are 120 µm deep, the left center inlet channel is 42 µm wide, the right mixing channel is 10 mm long and 65 µm wide, and the oblique side channels are (a) 65 µm and (b) 42 µm wide. (c) All channels are 10µm wide and 36 µm deep.

4.1.2 Materials

The lipid-blend (DMPC:Cholesterol:DCP in a molar ratio of 5:4:1) is prepared identical as described in the previous chapter. The dried lipid blend is resolubilized in IPA at a 5 mmol/L concentration of total lipid. PBS solution as previously described is used as a hydration buffer.

4.1.3 Liposome Formation

Unilamellar liposomes are prepared by injecting a lipid-blend dissolved in IPA at a concentration of 5 mmol/L into the center channel of the microfluidic network shown in Figure 17a-c. PBS is injected into the two oblique side channels intersecting with the center channel. The buffer-to-solvent flow rate ratio (FRR) is varied from 12 to 48 and from 6 to 36 in the 65 μm wide and 10 μm wide microchannels, respectively. The average flow velocity in the mixing channel of the 65 μm and the 10μm device is held constant at 0.25m/s, when comparing the FRR. Additionally, liposome formation at three different Q_ts (25 μL/min, 50 μL/min, and 100 μL/min) is investigated for different FRRs of 14, 19, 29, and 49 in the 65 μm wide microchannel design.

4.1.4 Light Scattering and AF^4 Procedure

High-resolution size-based separation of each liposome population is carried out using AF^4 with MALLS and characterization (model DAWN EOS, Wyatt Technology, Santa Barbara, CA) as described in the previous chapter. The injected sample volume is 120 μL.

4.2 Results and Discussion

It is important to point out that the scaling of the devices is not ideal. The aspect ratio between channel depth and nozzle width is approximately 3 for the 65 μm wide outlet channel (Figure 17a and b) and 3.6 in the 10 μm wide channel design (Figure 17c). The side channels in the 10 μm channel layout are perpendicular to the center channel, whereas in the in the 65 μm device they are at an angle of 45º. The maximum average Reynolds number (Re) is approximately 3 in the 10 μm channel and approximately 20 in the 65 μm channel. Nevertheless, the following results will show that the different channel layouts can be compared with each other. The liposome size distribution for 65 μm (Figure 17a) and 42 μm (Figure 17b) wide side channels is nearly identical, as is shown in Figure 18. Similar FRRs between the two designs mean that the flow velocity in the 42 μm side channels is higher than in the 65 μm, while the average flow velocities in the mixing and lipid injection channel are about equal. As can be seen from Figure 18 a minor deviation between the liposome size distributions is apparent at a low FRR of 12. Due to the increasing sensitivity of the liposome size distribution towards low FRRs the small deviation may not be attributed to a different side channel width but may be an artifact of a slight variation at the low FRR.

The very similar size distributions shown in Figure 18 suggest that the width of the side channel and the minor change in the area of the transition region where the lipid/IPA stream is focused do not strongly impact the liposome size distribution. At similar FRRs, both designs produce comparable liposome size distributions. With a Re of less than 40 at a maximum Q_t of 200 μL/min in the mixing channel inertial effects are small. Hence, mixing of the focused stream with the surrounding fluid should be independent of the angle between the side channels and the outlet channel.[82] From these

results a comparison between the 65 µm (with 65 µm wide side channels) and 10 µm device is justified.

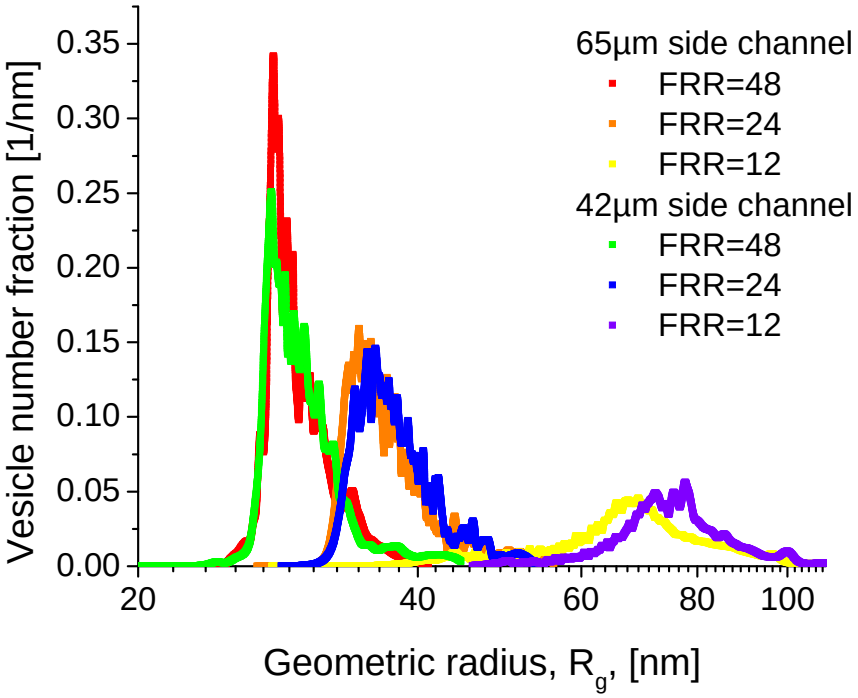

Figure 18 Comparison between 65 µm and 42 µm wide side channels at identical FRRs and a constant v_m of 0.25 m/s. The inlet channel width (42 µm) and mixing channel width (65 µm) is identical for both designs.

4.2.2 Influence of Microchannel Geometry on Liposome Formation

A lipid blend resolubilized in IPA is injected through the center inlet channel and hydrodynamically focused into a narrow stream by two oblique buffer streams. The total average flow velocity (v_m) is held constant and is limited to 0.25 m/s for both channel geometries to ensure complete mixing of the focused IPA by the sheathing PBS streams before exiting the mixing channel. Figure 19a and Figure 19b show the distribution of R_g for liposomes produced with the 10 μm and 65 μm wide mixing channels, respectively.

Decreasing FRR from 36 to 6 in the 10 μm wide channel design produces peak vesicle number fractions with R_gs ranging from approximately 25 nm to 74 nm, while decreasing the FRR from 48 to 12 in the 65 μm wide channel design produces peak vesicles number fractions with R_gs ranging from about 28 nm to 70 nm. The 10 μm channel geometry produces comparable liposome size distributions at about half the FRR of the 65 μm channel and hence about double the final alcohol concentrations in the liposome suspension. Furthermore, it can be seen from Figure 19a and Figure 19b that the distribution shape changes from a skewed distribution to a more symmetric distribution as the FRR increases.

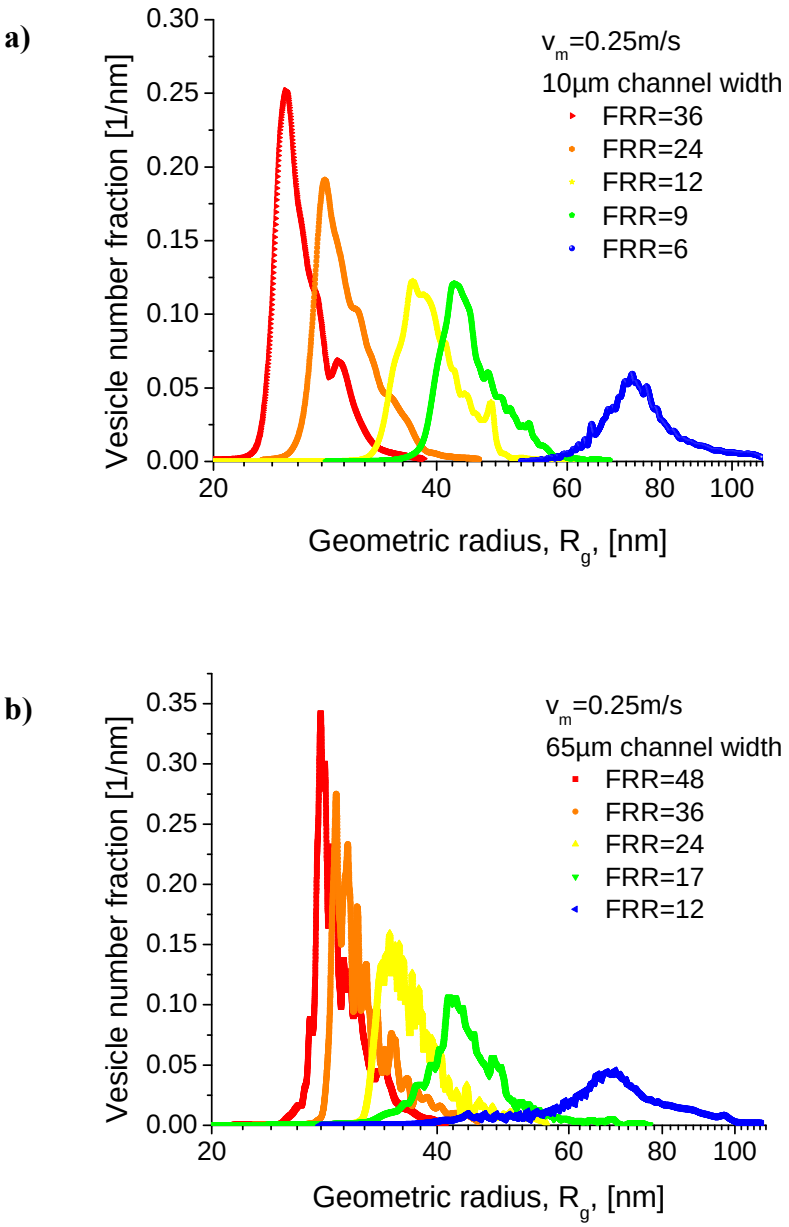

Figure 19 Distribution of the average geometric radius (R_g) of liposomes produced at different buffer-to-solvent flow rate ratios, FRR, and constant total flow velocity v_m=0.25 m/s. Liposome size distribution produced in a 10 µm wide and 36 µm deep channel (a) and in a 65 µm wide and 120 µm deep channel (b).

The results indicate that liposome formation is not solely dependent on focused stream width or on the final solvent concentration in the sample, in contrast to previous results where the injection of a larger amount of lipid-alcohol into pure buffer solution gives a larger polydispersity[39]. Neglecting a slightly flattened parabolic flow profile in the channel due to a higher solvent viscosity, the focused stream width scales linearly with the mixing channel width, so that the focused stream width is approximately 6.5 times larger in the 65 μm channel than in the 10 μm channel at a given FRR. For an arbitrary FRR of 6 in the 10 μm device and 44 in the 65 μm device the focused stream width equals to approximately 1.4 μm in both mixing channels. As can be seen from Figure 19 the liposomes size distributions vary significantly for these two cases. Although no liposome size distribution is shown for a FRR of 44 in the 65μm device, the liposome size distribution must be between that of a FRR of 36 or 48. This can be explained by the fraction of convective-diffusive mixing of the focused alcohol-lipid stream with the sheathing buffer streams that occurs in the focusing region versus the diffusive mixing region in the outlet channel.

4.2.3 Influence of Q_t on Liposome Formation at High and Low FRRs

In the previous chapter it was shown that the vesicle size distribution remains nearly unaffected by Q_t at high FRRs.[47,48] While Q_t has little impact on the average vesicle size at high FRRs (*i.e.* FRR > 30 in the 65 μm wide channel), its affect on the vesicle geometric radius increases noticeably towards lower FRRs (*i.e*. FRR < 20 in the 65 μm wide channel), as seen in Figure 20. Figure 20 a shows that decreasing Q_t results in smaller vesicle radii and increasing homogeneity apparent by the increasing peak height. Furthermore, it clearly shows that increasing Q_t changes the shape of the vesicle distribution from a skewed distribution to a more symmetric distribution, similar to decreasing FRR. From Figure 20a it can be seen that a FRR of 14 at a Q_t of 25 μL/min produces a peak number fraction of the vesicle R_g at about 40 nm similar to a FRR of 19 and a Q_t of 100 μL/min (Figure 20 b). However, a higher FRR produces a narrower vesicle radii distribution. Figure 20b suggests that increasing Q_t beyond 100 μL/min at a FRR of 19, can possibly produce larger and more homogenous liposomes than is possible with a lower FRR. However, substantially increasing Q_t beyond 100 μL/min at low FRRs requires a longer channel; otherwise mixing of IPA with PBS will be incomplete within the mixing channel. Although the width of the vesicle radii distribution changes slightly, the peak height increases towards lower Q_t at low FRRs, indicating an improving homogeneity. As the FRR increases, the vesicle radii distribution changes only subtly with Q_t. Since Q_t does not affect the vesicle size distribution at high FRRs it provides a means to increase the vesicle production rates. Figure 21 shows that the same trend is apparent in the 10 μm wide channel design.

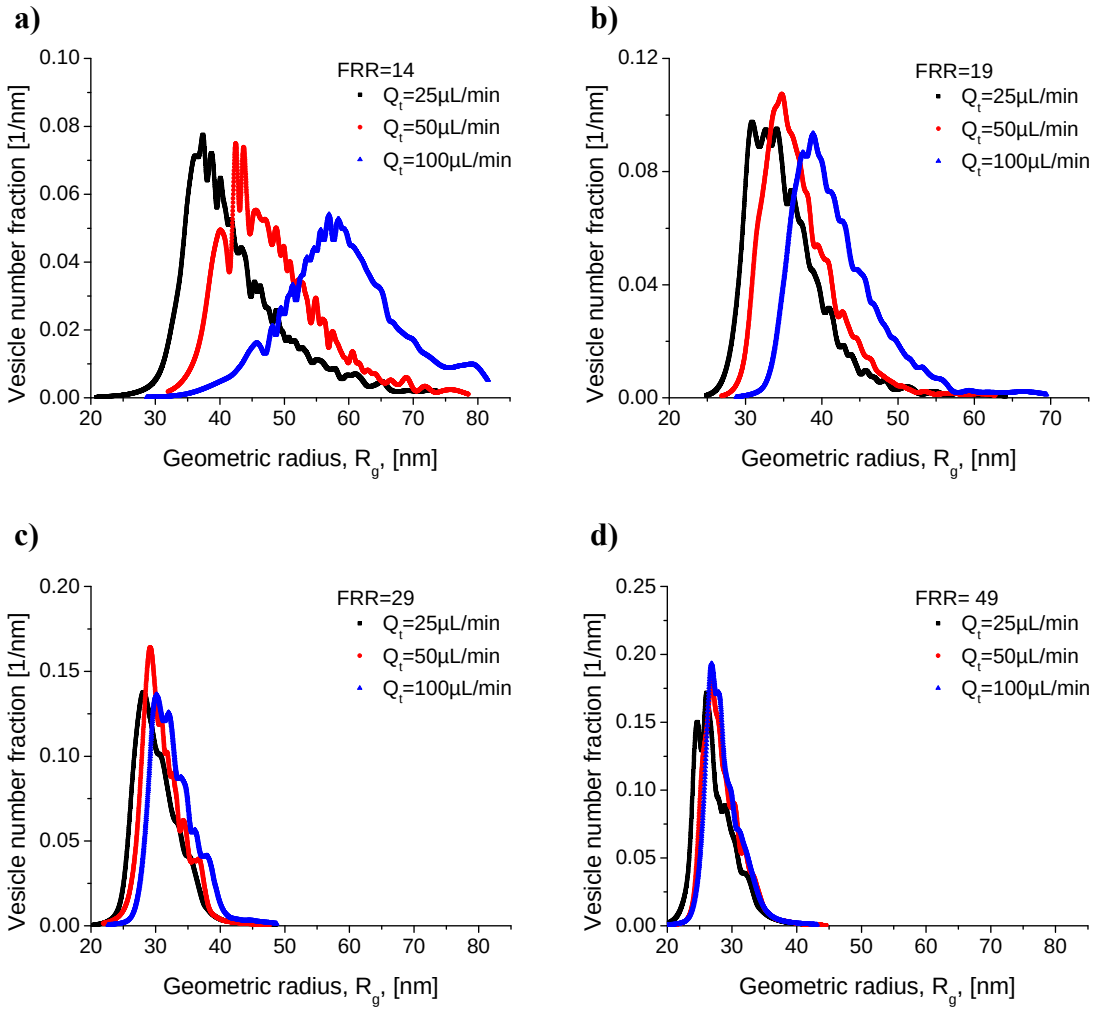

Figure 20 Liposome size distributions are determined with MALLS. Increasing Q_t from 25 µL/min to 100 µL/min at a constant FRR in the 65 µm wide channel increases the average liposome diameter. The velocity dependence is subtle at high FRR of 49 and increases noticeably towards low FRR of 14 in the 65 µm wide microchannel while only slightly affecting the vesicle homogeneity.

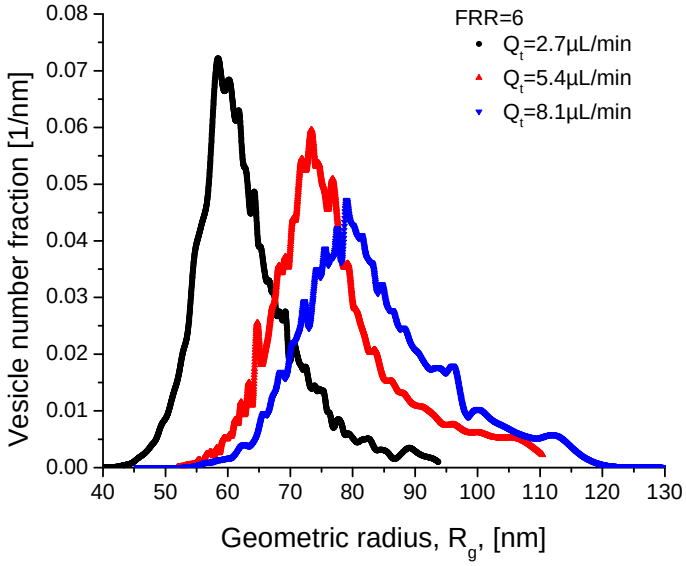

Figure 21 Liposome size distribution determined with MALLS. Increasing Q_t from 2.7 µL/min to 8.1 µL/min at a constant FRR of 6 increases the average liposome diameter in the 10 µm wide channel noticeably.

4.2.4 Influence of Diffusive and Convective Mixing on Liposome Formation

MHF does play an important role in applications that require short mixing times and low sample consumption. In the MHF method a central stream is sandwiched between two adjacent streams and focused into a thinner stream, thereby reducing the mixing length, according to the FRR between the miscible center and adjacent streams. The width of the focused stream is proportional to the width of the mixing channel and inversely proportional to the FRR, neglecting a slightly flattened flow profile that deviates from a parabolic flow profile due to the different viscosities between IPA and water.[48] The laminar flow in the microchannel makes this system very suitable for numerical analysis.[83,84] The mixing of IPA with water is investigated by simulating the experimental flow conditions. The obtained vesicle size distribution for the a FRR of 14

and 49 at a Q_t of 25 μL/min and 100 μL/min (Figure 20a and d) and FRR of 6 at a Q_t of 2.7 μL/min and 8.1 μL/min (Figure 21) is explained on the concept of two mixing regions, the convective-diffusive transition region and the diffusive region in the outlet channel to explain the different vesicle size distribution.

The concentration distribution of IPA sheathed by two adjacent water streams is simulated with a 2-dimensional model in FEMLAB 3.4 (Comsol, MA). The simulation couples the convective and diffusive mass transfer of IPA with the full Navier-Stokes equation for incompressible flow, considering spatially varying viscosity that depends on the local IPA/water volume fraction. The mass diffusivity of IPA and water results from the mass flux due to diffusion and the concentration gradient at the diffusive IPA/water interface. The directionality of the mass flux occurs from high concentration towards low concentrations of the respective solute. This means IPA diffuses from high concentration of IPA towards the aqueous phase whereas the water diffuses towards the focused IPA stream. The model approximates flow at the vertical midplane with two-dimensional flow simulations which is an idealization of the three-dimensional channel flow in the microchannel. The following state equations are solved iteratively,

$$-\nabla \cdot \eta\left(\nabla \bar{u} + (\nabla \bar{u})^T\right) + \rho \bar{u} \cdot \nabla \bar{u} + \nabla p = 0 \tag{4.1}$$

$$\nabla \cdot u = 0 \tag{4.2}$$

$$-\nabla \cdot \left(-D\nabla c + c\bar{u}\right) = 0 \tag{4.3}$$

where η is the dynamic viscosity, u is the velocity with components u and v in the x and y directions, ρ is the density, p is the pressure, D is the diffusivity, and c is the concentration of IPA.

Equations 4.1 - 4.3 are subject to the following boundary conditions:

$$\bar{u}(x_w) = 0 \tag{4.4}$$

$$\nabla c \cdot \hat{n} = 0 \tag{4.5}$$

where x_w denotes the location of the wall and n is the wall unit normal vector. Equation 4.4 accounts for the no-slip condition and no penetration boundary condition at the wall, while equation 4.5 enforces the condition of zero diffusional flux at the walls.[85] The boundary conditions at the inlets and outlets are as following (Table 1):

	Center-inlet	Side-inlet	Outlet
Concentration	c=1	c=0	Convective flux $(-D\nabla c)\cdot n = 0$
Velocity u: in x-direction v: in y-direction	average velocity $u=u_0$ v=0	average velocity u=0 $v=v_0$	outlet flow, pressure p_0=0 Pa $\eta\left(\nabla u + (\nabla u)^T\right)\cdot n = 0$

Table 1 Inlet and outlet boundary conditions for the momentum and mass-diffusion analysis.

At the outlet, the diffusive mass transport is neglected in the normal direction of the microchannel cross-section and the mass-transport is mainly driven by convection. The convective flux boundary condition in regards to mass transport at the channel outlet eliminates concentration gradients in the flow direction; it is an appropriate boundary condition for convection dominated mass balances where the outlet concentration is unknown as in this simulation. The average velocities in x- and y-direction are determined by the volumetric flow-rate (Q_t) at the respective buffer-to-solvent flow rate ratio (FRR) across the respective inlet channel cross-section. The center- and side-inlet channel length of the simulated geometry is approximately twice as long than the minimum channel length required for a constant velocity to develop into a parabolic flow profile according to Shah and London[86]

$$L_e \approx D_h \cdot \left(\frac{0.6}{1 + 0.035 \cdot \mathrm{Re}_{D_h}} + 0.056 \cdot \mathrm{Re}_{D_h} \right), \tag{4.6}$$

where L_e is the entrance length, D_h is the hydraulic diameter of the channel, and Re_{Dh} is the Reynolds number for the respective hydraulic diameter. Hence, it can be safely assumed that a parabolic flow-profile is completely developed before the different fluids intersect at the channel intersection.

In order to build a memory efficient model an unstructured mesh is chosen with low node numbers or low mesh densities far from the focused center stream and high node numbers (*i.e.* high mesh densities) within and in the immediate vicinity of the hydrodynamically focused stream. The reasoning being that the concentration gradient is

the steepest in the immediate vicinity of the mixing interface and therefore requires a higher mesh density to reduce the error across the mesh elements. Furthermore, the convective term leads to instabilities in the solutions; therefore a fine mesh is required to obtain a stable solution for the concentration field. The minimum mesh element quality of 0.47 is above the acceptable value of 0.3. Overall the mesh element quality is close to 1. In the incompressible Navier-Stokes application mode a triangular Lagrange p2-p1 element is used. Here, the velocity components are modeled with second-order Lagrange elements while the pressure is modeled with linear elements. The final mesh and geometry are shown in Figure 22

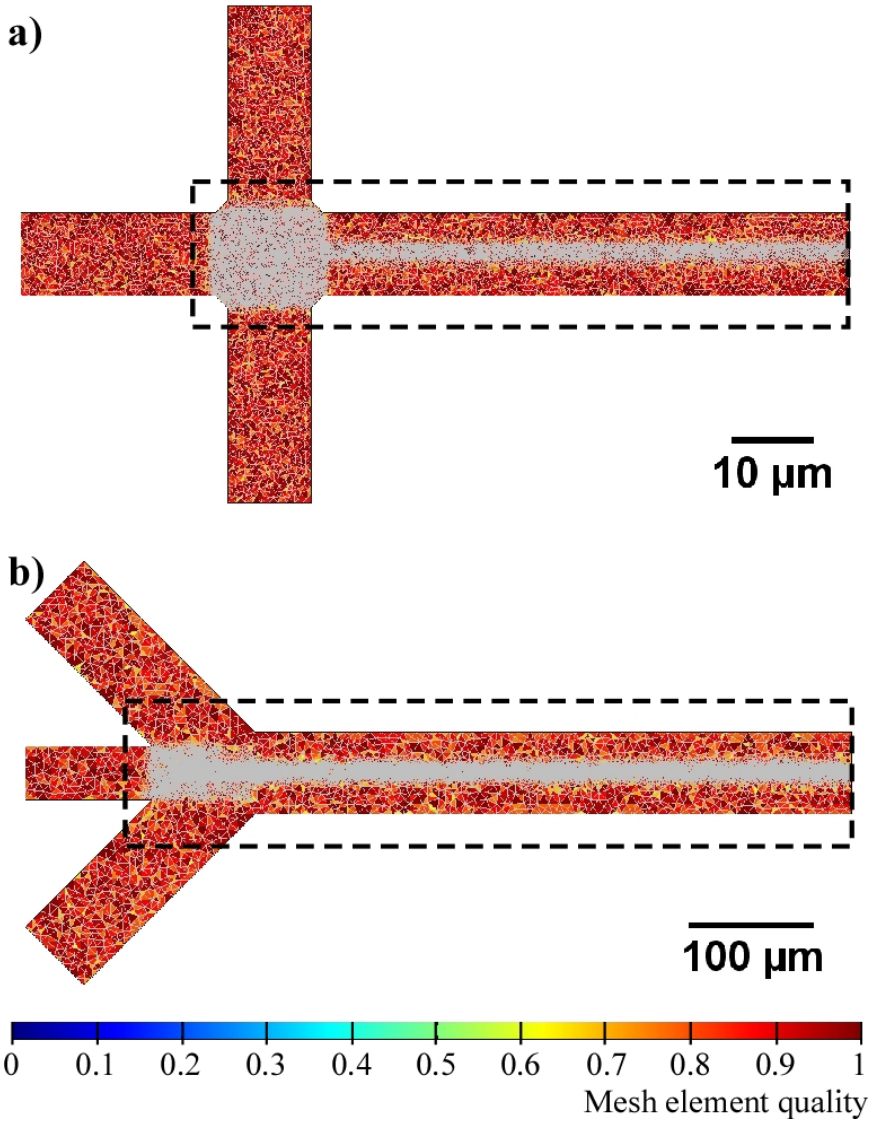

Figure 22 Shown are the respected meshes for the 10 µm (a) and 65 µm (b) wide microchannel geometries. The discontinuous rectangle in a) and b) show the truncated region for which the simulation results are shown in the following figures. The mesh of each geometry contains approximately 26.000 mesh elements, with higher mesh densities at the diffusive interface region between alcohol and water.

Homogenous mixing of IPA with water at the molecular scale is assumed in the simulation thereby neglecting micro-heterogeneities due to alcohol cluster formation[64,65,68], which showed that the motion of water molecules is strongly correlated with those of alcohol in alcohol rich mixtures above 50 mol % and alcohol cluster formation below 20 mol %. Viscous anisotropy due to mixing of IPA and water is accounted for by a fifth-order polynomial function fitting empirical data for the viscosity and mutual diffusion coefficient (D_{12}) at different volume fractions reported by Pratt et al.[67] (seeFigure 23).

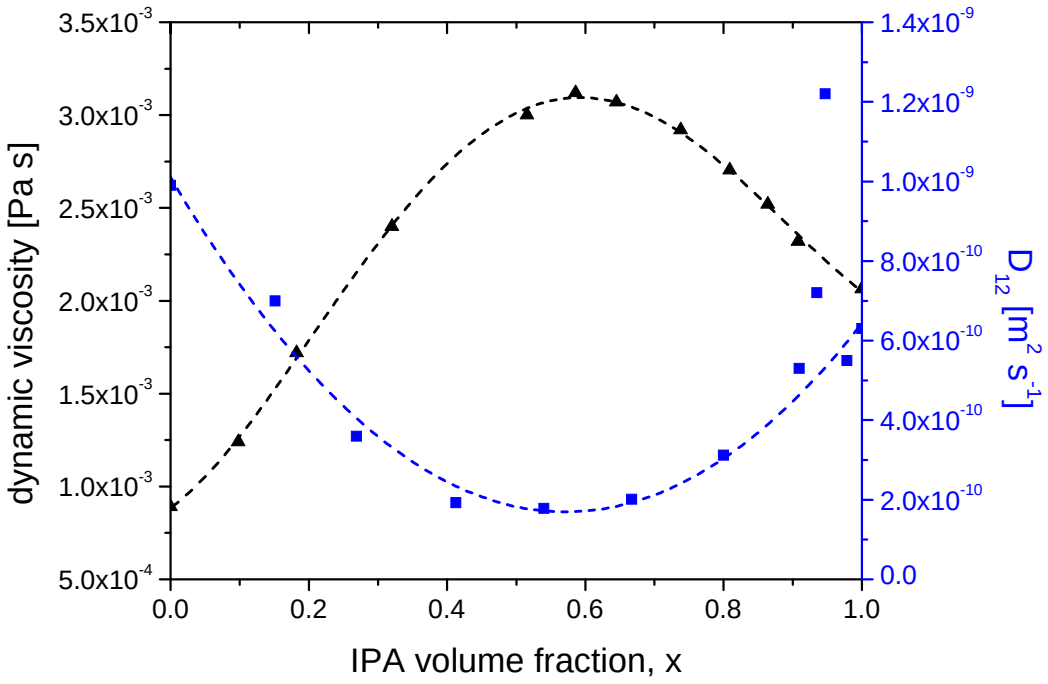

Figure 23 Experimental data for the dynamic viscosity (▲) and the mutual diffusion coefficient for IPA/water mixtures (■) are obtained from Pratt et al. for a temperature of 25 ºC. The dashed curves represent fifth-order polynomial fits to the experimental data for the dynamic viscosity (- - -) and the mutual diffusion coefficient (- - -) that are applied to the simulation model.

The following simulations show the resulting IPA concentration profile and the corresponding diffusive flux qualitatively for two different FRRs and Q_ts in the 10 µm (Figure 24) and 65 µm (Figure 25) wide channels, respectively. It is pointed out that the length of the focusing region between the 10 µm and the 65 µm channel design differs substantially. The length of the focusing region is with 10 µm in the 10 µm device approximately 9 times shorter than in the 65 µm device, while the average flow velocity is about the same in both devices.

It can be seen from Figure 24a and Figure 24c that a higher FRR causes a stronger focused stream at a specific Q_t. As the FRR increases the volume of the focused stream in the transition region decreases, while the surface area at the buffer-solvent interface increases. The result of the inverse relationship between decreasing volume and increasing interface area at increasing FRR is, that the lipid depletion rate due to self-assembly is higher than at lower FRRs. The more lipid molecules are depleted within the convective-diffusive transition region, the less lipid molecules are available to form larger liposomes in the diffusion dominated mixing channel. Conversely, at low FRRs the jet volume increases and the interface area decreases in the transition region resulting in a lower depletion rate of lipid molecules as a result of their self-assembly into liposomes. The fraction of lipid self-assembly in the mostly diffusion dominated mixing channel increases compared to the liposomes formed in the convective-diffusive focusing region, resulting in a greater amount of larger liposomes.

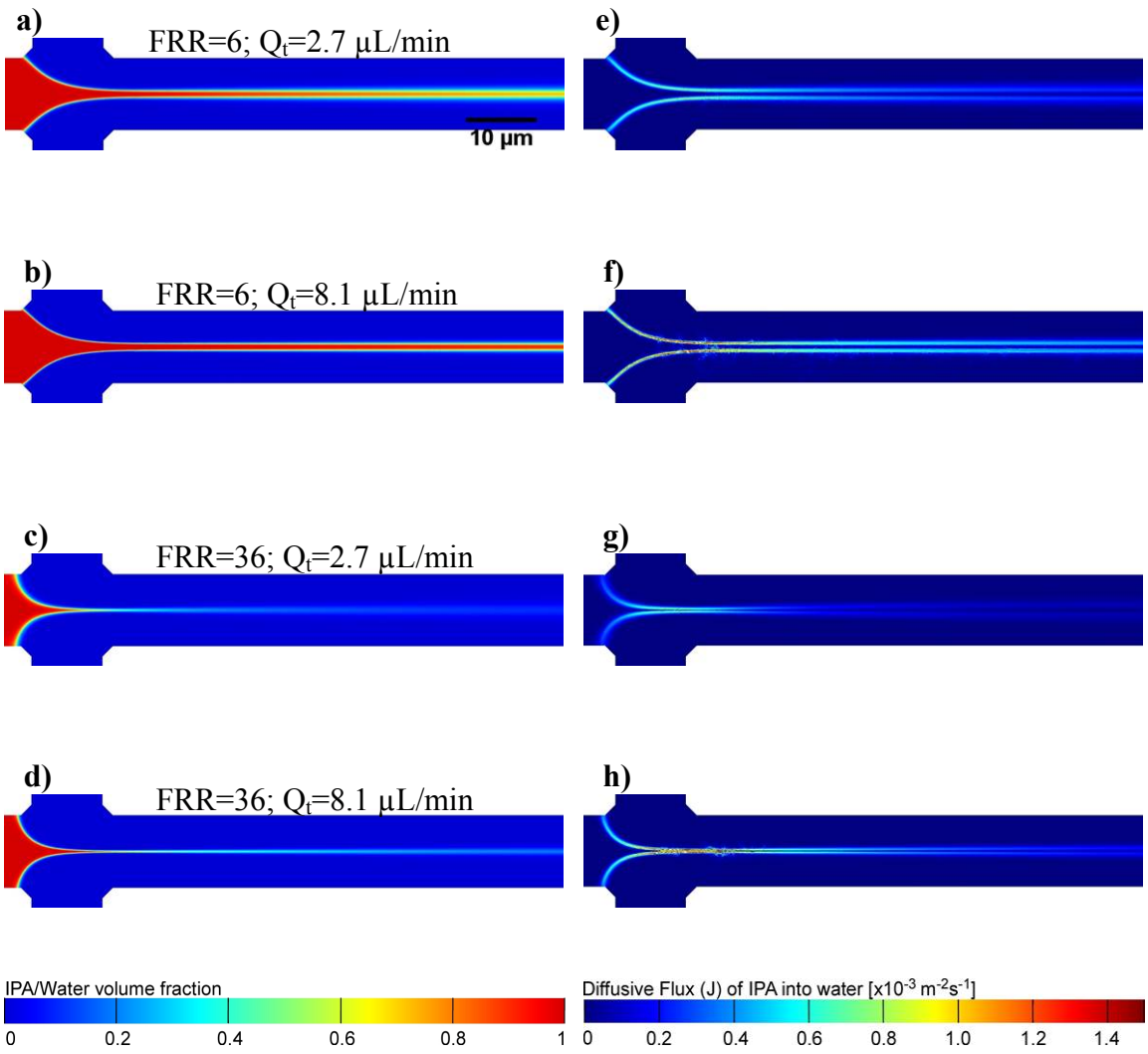

Figure 24 Simulated IPA concentration (a-d) and diffusive flux (e-h) profiles of the focused stream at a low FRR of 6 and a high FRR of 36 for a volumetric flow rate Q_t of 2.7 µL/min and 8.1 µL/min in the 10 µm wide channel device.

Modulating Q_t affects the convective-diffusive mixing of IPA and water in the focusing region as well as in the outlet channel section resulting in varying concentration profiles of IPA in water. A decrease of Q_t from 8.1 µL/min to 2.7 µL/min at a constant FRR of 6 for the 10 µm channel device results in a steeper IPA concentration gradient (Figure 24a and c). Figure 24 shows the diffusive flux at low Q_t, where a large fraction of the total diffusive flux is concentrated in the convective-diffusive transition region (Figure 24e). On the contrary, as Q_t increases a high diffusive flux can be seen over an extended region in the mixing channel (Figure 24f). The shape of the focused stream changes only minutely, considering a slightly different flow profile due to a different mixing and hence viscosity profile. This means that the surface-to-volume ratio does remain approximately constant at varying Q_t and constant FRR. Similar to decreasing Q_t, increasing the FRR increases the amount of mixing of the focused stream in the focusing region. At a high FRR of 36 IPA in the focused stream is strongly diluted within the focusing region and most of the diffusive flux occurs within or close to the convective-diffusive mixing region, as can be seen in Figure 24c and Figure 24g. Increasing Q_t only slightly shifts the diffusive flux into the solely diffusive region in the outlet channel (Figure 24h). Furthermore, the high focusing (high surface-to-volume ratio) depletes the lipid molecules due to self-assembly into liposomes at a higher rate. Hence, the remaining lipid-molecules in the diffusive mixing region form not as many larger liposomes. The same applies to the 65 µm wide channel and can be seen qualitatively in Figure 25.

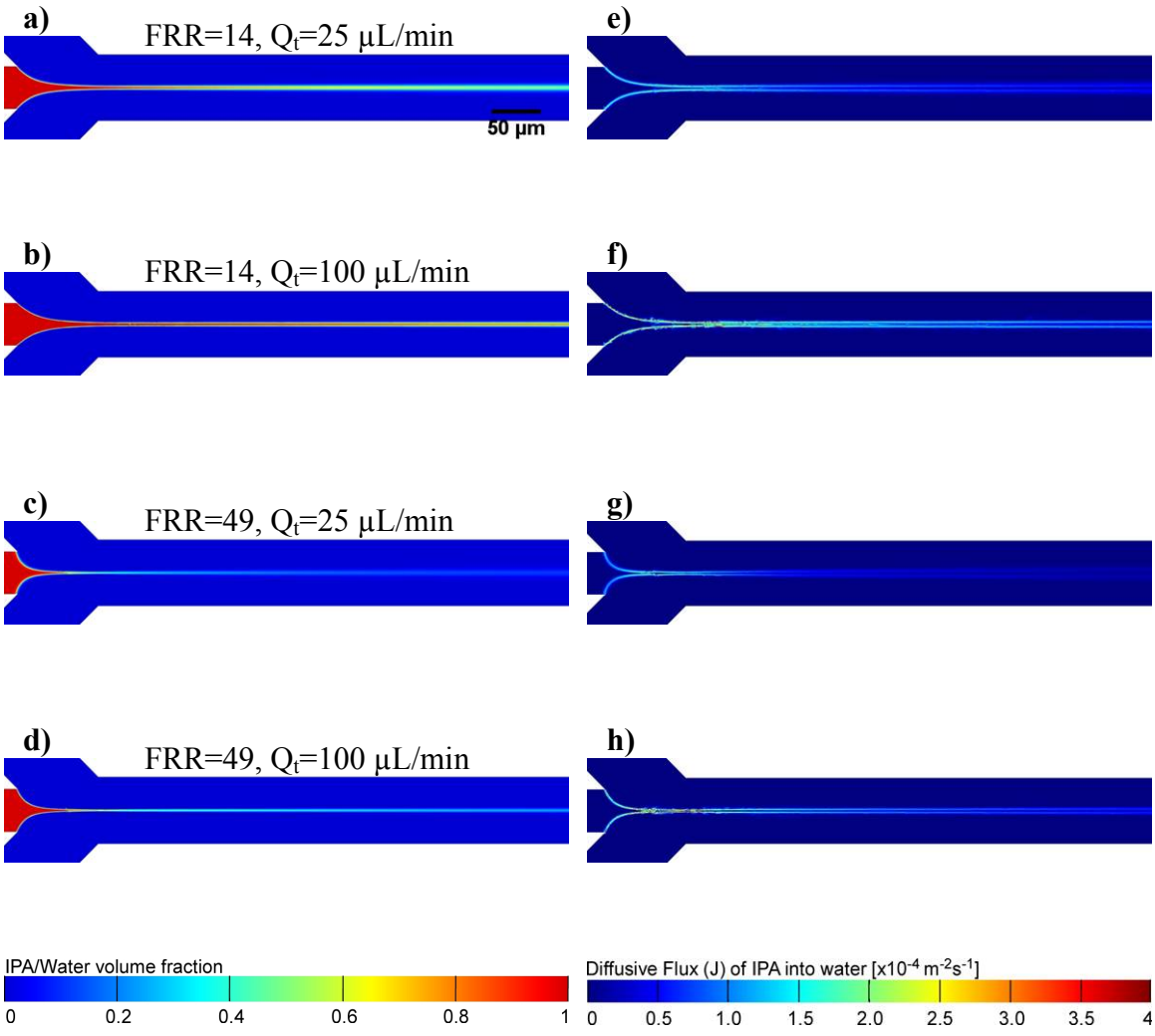

Figure 25 Simulated IPA concentration profiles of the focused stream at the lowest FRR of 6 and the highest FRR of 36 for a volumetric flow rate Q_t of 2.7 µL/min and 8.1 µL/min in the 65 µm wide channel (a-d) and their respective diffusive flux (e-h).

The following image sequence in Figure 26 shows a comparison of the focused IPA stream in a the 65 µm wide microchannel imaged with a fluorescence microscope and the 2-dimensional model simulation for the respective FRRs of 14 and 49 and Q_ts of 25 µL/min and 100 µL/min. It also shows that the shape of the focused IPA stream is represented correctly in the simulation. A measurement of the width of the focused stream is not possible as IPA and water continuously interdiffuse along the interface.

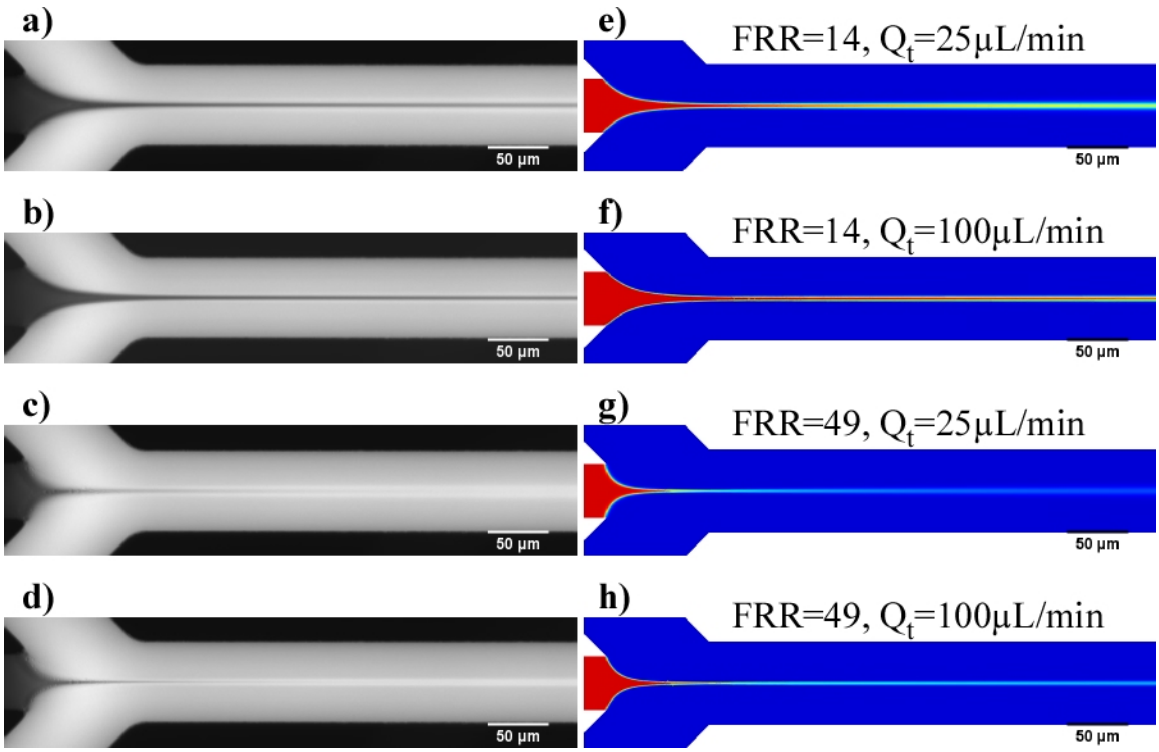

Figure 26 A comparison of the fluorescent microscope image (a-d) with the respective simulation (e-h) shows a very good correlation in the shape and the approximate width of the focused stream. This shows that the 2-dimensional model qualitatively represents the 3-dimensional experimental system. The fluorescence microscope images are obtained with 30 µmol/L SRB dissolved in PBS injected from the oblique side channels and IPA injected through the center inlet channel at the respective FRRs and Q_ts shown in the images (e-h).

The results show that similar vesicle size distribution can be obtained in both channel geometries, despite the fact that lipid molecules convect through different concentration gradient per time along the symmetry line. This suggests that the lipid self-assembly time scale is shorter than the convective time scale for lipid molecules to convect along the steep concentration gradient in the 10 μm channel. A high ratio of diffusive flux within the transitions region tends to produce smaller more homogeneous liposomes, while a higher fraction of the diffusive flux in the mixing channel region produces vesicles with a larger average R_g and broader size distribution. The qualitative description of IPA/water mixing and depletion along the interface and the separation of the vesicle formation into two different mixing domains provide a unifying concept to explain the obtained vesicle size distributions at different flow conditions and geometries. From the results of both channel designs it can be concluded that increasing the FRR and thereby increasing the focusing of the IPA stream increases the fraction of lipid self-assembly in the convective-diffusive transition region *versus* the diffusive mixing channel. Figure 19 shows that a higher FRR results in smaller liposomes, suggesting that they are primarily formed in the transition region before the focused jet enters the mixing channel. In contrast, a low FRR results in larger liposomes, which are primarily formed in the diffusively dominated mixing channel. The results clearly indicate that the lipid self-assembly strongly depends on the solvent-buffer interface and not solely on the final solvent concentration or focused stream width.

4.2.5 Reproducibility of Liposome Formation with MHF

The ability to produce similar average liposomes diameter with the same FRR and Q_t repeatedly suggests a fundamental underlying mechanism and rules out that the formation occurs after the microchannel exit, where mixing is uncontrolled. Figure 27 shows the vesicle size distributions at a FRR of 19 and 49 and a Q_t of 50μL/min, and 150μL/min prepared on three different days with a complete new set of reagents. The dynamic and static light scattering instruments have an accuracy of 2 % to 5 % for their respective particles size range (MALLS 10 nm to 500 nm, QELS 1 nm to 30 nm in flow mode) and obtain reproducibility between measurements of better than 1 %. As can be seen in Figure 27, the average liposome geometric radius shows only minor variations that are within less than 10 % of the number-weighted average radii for each set of experiments. It can also been seen that the weighted average radii varies less than 5 % for liposomes formed at a high FRR of 49. The number-weighted average radii of liposomes prepared on different days but with the focus on applying similar conditions vary less than 10 % for larger vesicles and less than 5 % for smaller vesicles. Variations in the sample preparation procedure such as desiccation time and the use of dry IPA *vs.* regular IPA reduce the batch-to-batch consistency especially for liposomes obtained from a less focused stream. Batch-to-batch consistency is especially affected by the use of proper inline filters. It is advisable to use syringe-filters with low to no dead volume and carefully wet them, paying specific attention to the removal of entrapped gas bubbles. Entrapped gas bubbles in the filter can induce oscillations during focusing and hence affect the liposomes size distribution in consecutive runs.

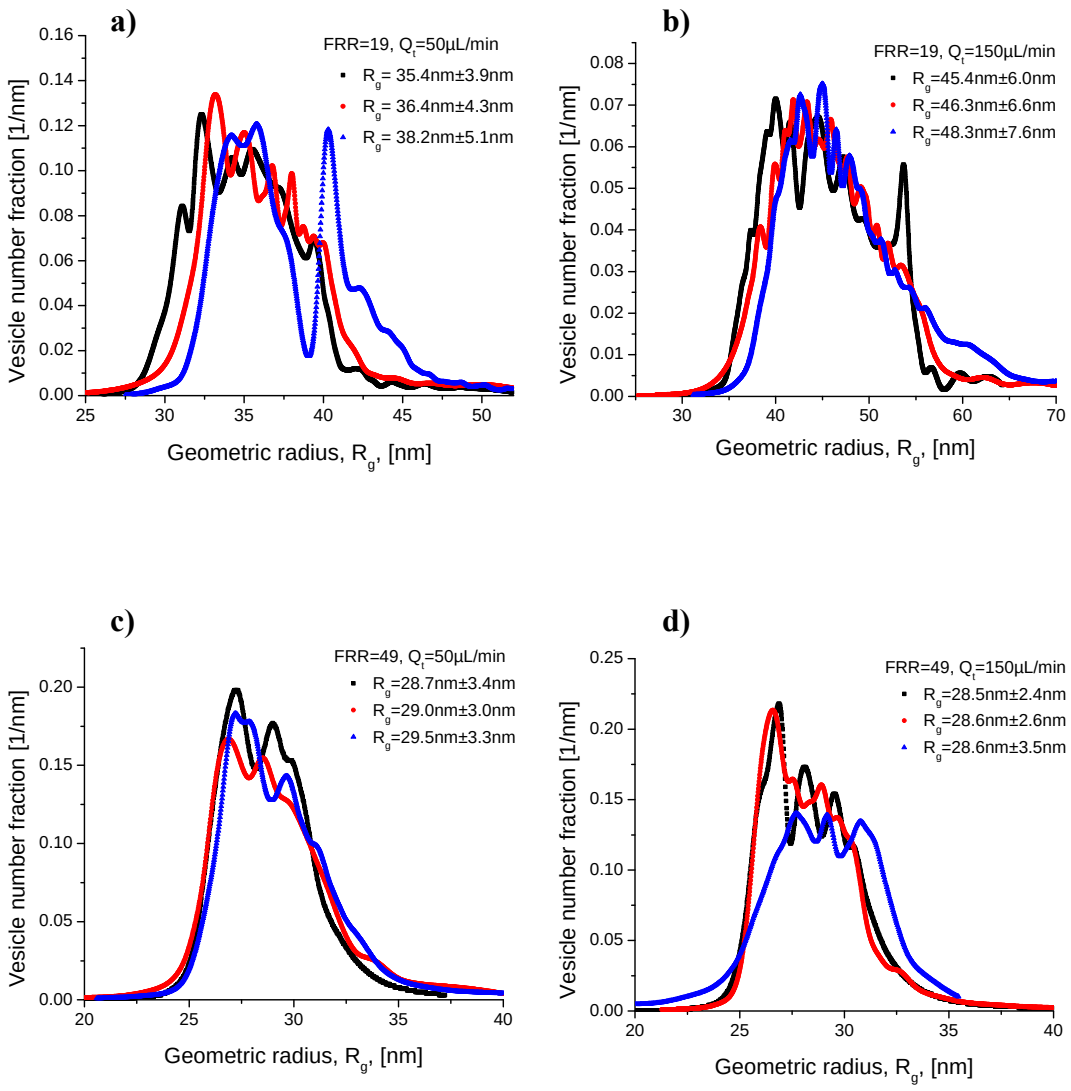

Figure 27 Shown are liposome size distribution of liposomes prepared in the 65 µm wide multiple-inlet channel design on three different days under various flow conditions; (a) FRR=19 and Q_t=50 µL/min, (b) FRR=19 and Q_t=150 µL/min, (c) FRR=49 and Q_t=50 µL/min, and (d) FRR=49 and Q_t=150 µL/min.

4.3 Summary

The results of these experiments are used to elucidate several phenomena related to microfluidic directed liposome formation including the effects of focused stream width, alcohol concentration gradients, and flow velocity. The combined effect of the technological advances and improved understanding of formation processes will potentially facilitate on-chip integration of this technique as well as its use in point-of-care medical treatment. Using a narrower channel width, the channel length can be reduced due to smaller focused stream width and shorter mixing times, reducing the footprint of the device for on-chip integration. The smaller microfluidic device presented produces comparable liposome size distribution that are slightly narrower particularly between 60 nm to 80 nm liposome geometric radii, and higher liposome concentrations for a given size distribution due to lower buffer-to-solvent flow rate ratios.

Changing the device geometry provides a simple means to increase the liposome concentration in a sample. A higher vesicle concentration in the smaller channel geometry should therefore allow higher encapsulation efficiencies and may increase the applicability of liposome formation with MHF for drug delivery applications. Reproducibility measurements demonstrate that microfluidic liposome formation allows for consistency beyond that of other techniques, which is essential for the integration and application of this technique.

The laminar flow conditions prevalent in MHF allows simulating mass and momentum transport and enables a more thorough investigation of the vesicle formation process. The combined experimental and simulation results suggest that the obtained liposome size distribution can be correlated in a first approximation by considering the

formation in the convective-diffusive focusing region and the diffusive mixing channel region.

The results discussed herein provide directions to be used in numerical simulation to improve channel design and optimize vesicle size distributions to hopefully provide very narrow vesicle size distributions of larger vesicles in the future. The facile control of liposome formation with MHF provides a means to systematically investigate the liposome formation process. A complete understanding of the formation process requires further investigation including viscous anisotropy of alcohol/buffer systems and the polarity and chemical potential of different alcohols.

Considering the viscous anisotropy and polarity of various alcohols is a next step that may help to understand the different vesicle size distributions obtained with other solvent-water combinations such as ethanol or methanol in water. Another effect not yet investigated experimentally but through simulation is viscous anisotropy. The viscosity of an IPA-buffer mixtures increases from the viscosity of pure IPA, peaks at about 3 times the viscosity of water, and decreases to the viscosity of water in the absence of IPA. This viscous anisotropy retards molecular diffusion at the IPA/water interface and can have a pronounced effect on the lipid self-assembly into liposomes. A big role to further elucidate the lipid self-assembly process could come from molecular dynamics simulations combined with mass and momentum transport simulation.

Chapter 5: Controlled Encapsulation of a Model Drug in Nano-Liposomes

The previous chapter focused on details of the liposomes formation process of with microfluidic hydrodynamic focusing (MHF). It was demonstrated that geometric aspects regarding the channel design and hydrodynamic aspects such as FRR and Q_t influence the final liposome size distribution. This chapter focuses on the encapsulation characteristic of liposomes formed with MHF.

5.1 Introduction

Nanoparticles can either be used for drug delivery applications to achieve selective and sufficiently high localization of "active" drug at the disease site, or as container for single molecules studies. A promising candidate for both spectra, high loading as in drug delivery applications as well as encapsulation of single or few molecule, are liposomes. While selective localization by means of passive and active targeting is not in the scope of this work, the encapsulation characteristic of compounds into liposomes is. In order to successfully apply liposomes in drug delivery applications it is important to controllably load the compounds (*i.e.* drugs, vaccines, therapeutics, etc.) of interest into liposomes. This can be achieved by passive or active loading. In the microfluidic approach as discussed in this work, the loading of liposomes is facilitated by passive means. In conventional passive loading techniques, liposomes are formed in a bulk aqueous solution containing a homogenous concentration of water-soluble encapsulant. Unfortunately, due to the formation method only a small fraction of the compound is eventually encapsulated and a large fraction of non-encapsulated compound needs to be recycled for further use. In contrast to macro-scale batch liposome formation

and loading, microfluidics allows minimizing the amount of non-encapsulated compound by confining it solely to the immediate vicinity where liposomes formation and concomitant encapsulation occurs.

A common approach to determine the amount of encapsulated compounds requires one to measure the liposome concentration, lyse the liposomes, and measure the fluorescence intensity of the new solution.[76,87-89] This approach has several shortcomings. First, the characterization process destroys the sample; second, lysing the liposome sample requires the addition of a surfactant (Triton X-100, etc) which itself typically shows strong fluorescent properties; finally, this approach assumes one can measure the absolute concentration of a liposome sample or that the concentration in a liposomes equals that in the initial medium[90,91]. Techniques such as direct counting, used for cellular analysis, will not work for nanometer-sized liposomes and scattering experiments require model dependent parameters to estimate the true particle concentration. These models can lead to large uncertainties in absolute particle numbers.

The fluorophore sulforhodamine B (SRB) serves as a hydrophilic drug simulant that is encapsulated into liposomes to investigate the loading characteristic with MHF. The number of encapsulated SRB molecules is determined with fluorescence fluctuation analysis, which is a non-destructive technique.[92-94] Specifically, we combine FCS analysis with the first two cumulants of the fluorescence intensity fluctuations to quantify the number of encapsulated SRB molecules. In the analysis it is not assumed that the liposomes in a given sample are equally bright, but rather, the number of SRB molecules per liposome follows a Poissonian. This allows analyzing the number of encapsulated

SRB molecules at low dye concentrations where the average number of encapsulated dye molecules is less than one.

The ability to control the entrapped amount of compound by adjusting the flow parameters in the multiple-inlet microfluidic channel network is discussed. Additionally, it is demonstrated that in the applied passive continuous-flow microfluidic encapsulation strategy, the number of encapsulated molecules depends on the liposome size and the compound concentration in the mobile phase. It is shown that the microfluidic system allows controlling the number of encapsulated SRB molecules while minimizing the compound consumption.

5.2 Description of Experimental Procedures

The multiple-inlet microchannel design is used to investigate the loading characteristics of liposomes with MHF. The fabrication of the microchannel is according to the previous chapters. Briefly, the microchannels have a rectangular cross section due to DRIE. The width of the center inlet channel is 42 μm, the mixing channel and the oblique side channels for PBS are 65 μm, and the two inner side channels for the compound to be encapsulated are 42 μm wide. All microchannels are 120 μm deep.

High resolution separation of the liposome population according to their hydrodynamic radius and subsequent size distribution analysis was performed using AF^4 with multi-angle laser light scattering (MALLS) and quasi-elastic light scattering (QELS) (model DAWN EOS and QELS, Wyatt Technology, Santa Barbara, CA) as described in the previous chapters.

5.2.1 Materials

The lipid-blend composed of DMPC:Cholesterol: DCP at a molar ratio of 5:4:1 is prepared as described previously. Sulforhodamine B (SRB) was dissolved in PBS at multiple concentrations ranging from 500 nmol/L to 500 µmol/L. Polyethyleneglycol with a molecular weight of 6 kDa (from hereon referred to as PEG-6000) is mixed into a liposome sample at a concentration of 10 % by weight to determine if fast fluctuation measured with FCS stem from background SRB or encapsulated SRB.

5.2.2 Liposome Formation

A lipid mixture dissolved in IPA is injected into the left center channel of the microfluidic network, SRB dye is dissolved in PBS at a concentration of 0.5 mmol/L and injected into the two inner side channels, and PBS without SRB dye into the two outermost side channels all intersecting with the center channel, as is shown in Figure 28. Encapsulation studies to reduce the amount of non-encapsulated SRB were performed with a constant FRR of 35 and a Q_t of 200 µL/min. The total SRB dye content in the system was varied between 5 v/v % to 40 v/v % of the total liquid volume by adjusting the volumetric flow rate of the outer and the inner side-channels, respectively. A volume of 500 µL of the liposome effluent was collected from the outlet channels of the microfluidic network and subsequently filtered through a polyacrylamide column with a MWCO of 6 kDa to remove non-encapsulated SRB. In order to determine if gel filtration affects the liposome size distribution, multiple liposomes samples are prepared at a Q_t of 100 µL/min and 200 µL/min and at FRRs of 19, 29, and 39. The samples are measured before and after gel filtration. The number of SRB molecules encapsulated into

liposomes is investigated with vesicles prepared at a Q_t of 100 µL/min and two FRRs of 19 and 49; all side channels contained SRB dissolved in PBS at concentrations varying from 500 nmol/L to 250 µmol/L.

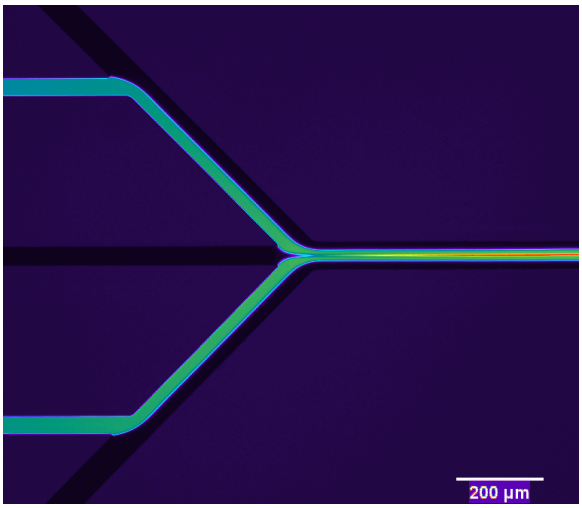

Figure 28 False color confocal fluorescence micrograph of the microchannel network showing the fluorescent intensity of 0.5 mmol/L SRB in PBS injected into the left two inner side channels. PBS without SRB dye is injected into the left two outer side channels, and lipid mixture is injected into the left center channel.

5.2.3 Fluorescence Fluctuation Spectroscopy

The experimental work is performed on a confocal fluorescence microscopy setup built upon an inverted microscope (Axiovert 200, Carl Zeiss, Germany), as shown schematically in Figure 29. A frequency doubled Nd:YAG laser (SLM-532-50, Crystalaser, Reno, NV) operating in continuous wave mode at 532 nm is sent through the back aperture of a 63x, 1.2 NA, water-immersion microscope objective (Carl Zeiss, Germany). The laser beam underfills the back aperture of the objective to create an

excitation volume greater than the diffraction limited volume. The laser power measured after the light passes through the microscope objective is 150 μW. A constant laser power is maintained by manually adjusting the polarization optics to eliminate intensity fluctuations between sample runs (on the order of 10 minutes).

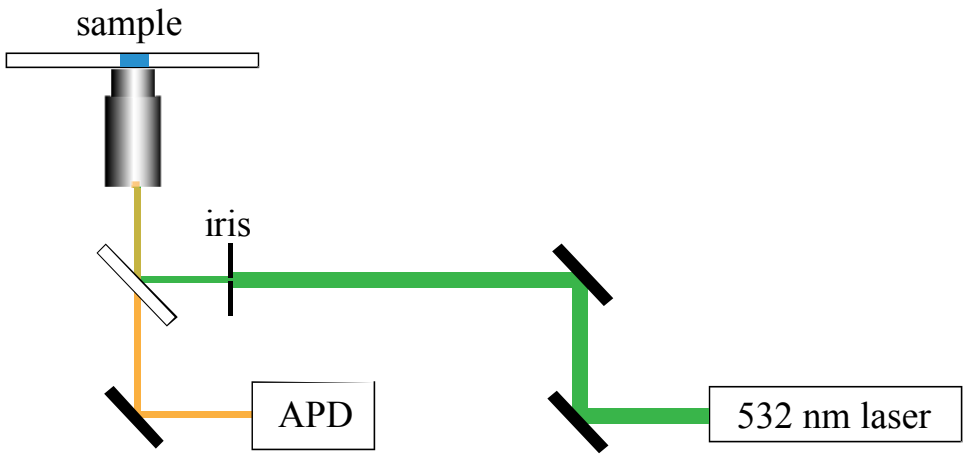

Figure 29 A schematic drawing of the experimental setup. Not all lenses and mirrors are shown. The adjustable iris before the microscope objective shutters down the input beam in order to increase the excitation volume. The fluorescent light is sent back through the objective and passes through a dichroic mirror and is directed into the single photon counting module (APD). TTL pulses from the APD are sent to a computer for processing.

A chamber for the 100 μL of the sample solution (liposomes and free SRB dye) is made by drilling a 1 cm hole through a microscope slide and sealing both sides of the microscope slide with a #1.5 glass coverslip using vacuum grease. Fluorescence light from the sample is focused down onto a 100 μm pinhole, appropriate dichroic mirrors and optical filters (Omega Optical, Brattleboro, VT) direct the fluorescence light of

interest onto the active area of an avalanche photodiode (AQR-SPCM-14, Perkin Elmer, Ontario, Canada). Most photon arrivals create transistor-transistor logic (TTL) pulses that are sent to a peripheral component-interconnect (PCI) hardware counting card (PCI-6602, National Instruments, Houston, TX).

The TTL pulses are counted and analyzed with a homemade software (Labview 8.0, National Instruments) multi-tau correlator having a temporal range from 4 μs to 2 s.[95] The software bins the number of photons arriving within 16 μs integration time to create a photon counting histogram (PCH). The ACF and PCH is stored every 10 s. Typically, 30 data sets are collected for each sample from which the first two moments along with standard deviations are calculated. Deadtime and afterpulsing effects are corrected for following a method described elsewhere.[94] Occasionally, large photon bursts occur from a cluster of liposomes diffusing through the laser beam. Any 10 s data-set that leads to a value greater than 4 standard deviations from their respective means for either of the first two fluorescence moments is discarded. All results are reported with standard error bars at the 95 % confidence interval.

The fluorescence properties of the detection system are calibrated with 1 nmol/L SRB in PBS. A stock solution of 1 nmol/L SRB in PBS is prepared and 100 μL of it is measured before and after each liposome sample. From the calibration data three parameters of interest are extracted; the free SRB diffusion time, $\tau_{D(SRB)}$, the ratio of the axial extension and waist of the excitation volume, z/w, and the molecular brightness of a single SRB molecule, x_{SRB}. The measurements result in a laser exaction volume and standard deviation of 11.2±0.5 fL, corresponding to a full beam waist w_0 of 1.4 μm and a

diffusion coefficient D of 4 x 10^{-10} m^2/s. The brightness of a single SRB molecule is determined with a photon counting histogram as following,

$$x_{SRB} = \frac{\langle \Delta P^2 \rangle - \langle P \rangle}{\langle P \rangle}. \tag{5.1}$$

A non-systematic error of 5%-10% is present in the values for x_{SRB} throughout the course of the day. This drift is not dependent on laser power fluctuations because it is monitored before and after each sample run, and is stable during the measurement time of approximately 2-3 minutes. There are also no moving parts in the laser path (*e.g.*, flipper mount mirrors). Therefore, this error is propagated as a standard deviation throughout all the relevant calculations.

The autocorrelation of each liposome sample is used to extract the average number of background SRB molecules, N_{SRB}, contained within the laser excitation volume. It is assumed that the liposomes are non-interacting and point-like (no significant contribution of Brownian fluctuation from encapsulated SRB). For this type of system, Qian et al. developed relationships between the mean and variance of the number of photon counts detected per unit time from this arrangement and the brightness, x_i, and number, N_i, of the fluorescent species within the excitation volume.[96]

$$\langle P \rangle = \sum_{i=1}^{k} N_i x_i + \langle P_B \rangle, \tag{5.2}$$

$$\langle (\Delta P)^2 \rangle - \langle P \rangle = \sum_{i=1}^{k} N_i x_i^2, \tag{5.3}$$

where $\langle\ \rangle$ is a time average, $\langle P \rangle$ is the average number of photons detected per unit time, and $\langle P_B \rangle$ is the average background count rate (count rate for a sample with no fluorescent species) which we assume to be Poissonian.

Each liposome in a given ensemble contains an integer number, *n*, of SRB dye molecules (*n* = 0, 1, 2, …). Liposomes containing *n* SRB molecules will be *n* times brighter than a free SRB molecule as long as the concentrations are within the non-self-quenching regime of SRB. The number of encapsulated SRB molecules across the liposome population is described with the brightness probability distribution, $\Pi(n)$, defined as the probability for a given liposome to contain *n* fluorescent SRB molecules. It is assumed that not all SRB in our sample is sequestered into the liposomes, but rather, some amount of SRB is freely diffusing in the exterior of the liposomes. For an ensemble of liposomes, each having an integer number of SRB molecules, the first two cumulants of the fluorescent signal can than be rewritten from eq. 5.2. and 5.3 as,

$$\langle P \rangle = N_{SRB} \cdot Q_{SRB} + N_{lip} \cdot x_{SRB} \cdot [n] + \langle P \rangle_B \text{ and} \tag{5.4}$$

$$\langle (\Delta P)^2 \rangle - \langle P \rangle = N_{SRB} \cdot x_{SRB}^2 + N_{lip} \cdot x_{SRB}^2 [n^2] \tag{5.5}$$

where, x_{SRB} is the free SRB dye molecular brightness measured in the number of detected photons per molecule per unit time, N_{lip} and N_{SRB} are the average number of liposomes and free SRB dye molecules (independent of *n*) within the laser excitation volume, $\Delta P = P - \langle P \rangle$ are the fluctuations about the mean number of detected photons per unit time, and

$$[n^x] = \sum_n \Pi(n) n^x \ , \tag{5.6}$$

where [ ] represents and average over the brightness probability distribution. Combining eq. 5.4 and 5.5 results in the following expression,

$$J = \frac{[n^2]}{[n]} = \frac{\langle(\Delta P^2)\rangle - \langle P\rangle - N_{dye}\cdot x_{SRB}^2}{x_{SRB}\cdot\left(\langle P\rangle - \langle P\rangle_B - N_{dye}\cdot x_{SRB}\right)}. \tag{5.7}$$

Assuming all liposomes in a given sample are equally bright (a common assumption) is equivalent to setting $[n^2] = [n]^2$ and $J = [n]$ equals the average number of dye molecules contained per liposome. A more realistic assumption is that the number of molecules per liposome is given by a Poisson distribution ($[n^2] = [n]^2 + [n]$). From this distribution we find an expression for the average number of molecules per liposome,

$$[n] = J - 1. \tag{5.8}$$

Equation 5.8 is a critical result, namely a proper assumption of the brightness distribution function, $\Pi(n)$, will avoid overestimates of encapsulated SRB in liposomes. This observation becomes especially important in the low concentration limit ($[n] < 1$).

5.3 Results and Discussion

5.3.1 Liposome Size Distribution after Gel Permeation Chromatography

Before analyzing the fluorescence intensity of the liposomes the non-encapsulated SRB in PBS must be removed. This is accomplished by filtering 500 µL of the sample containing liposomes and non-encapsulated SRB through a 6 kDa MWCO polyacrylamide gel column. A major concern during gel-filtration is the possible interaction of liposomes with the gel matrix of the column and thereby a change of the original liposome size distribution. Figure 30 shows the liposome size distribution for two different sets of liposomes before and after gel permeation chromatography.

a)

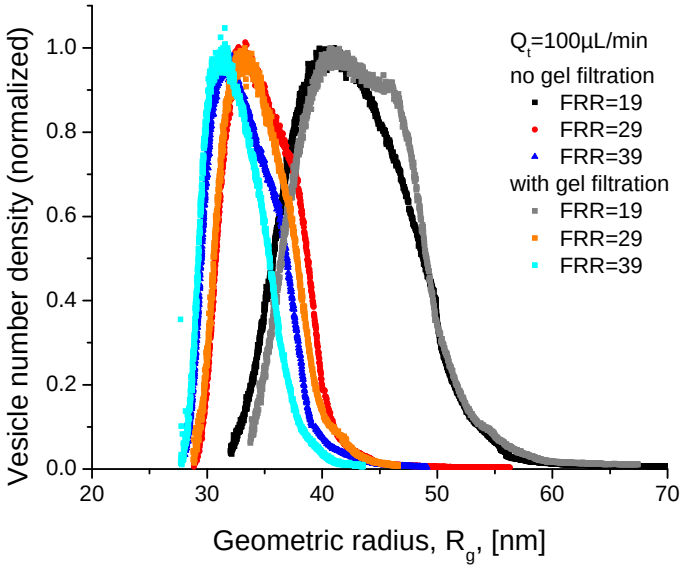

b)

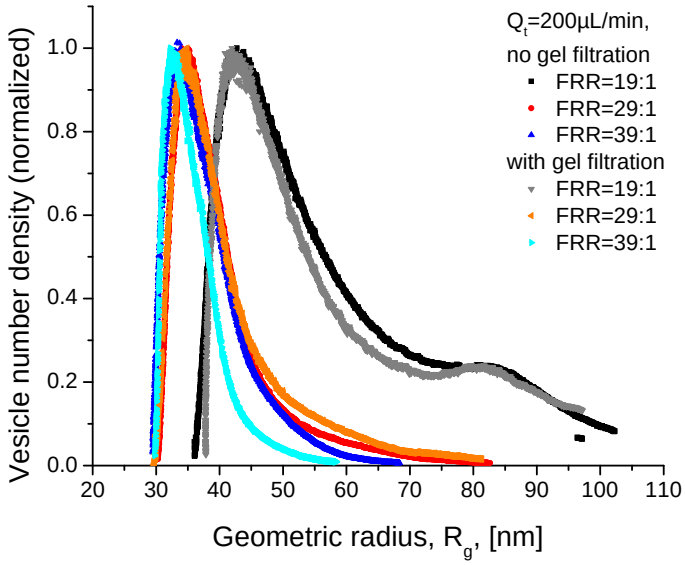

Figure 30 Shown are the liposome size distributions before and after gel permeation chromatography for liposome prepared at a FRR of 19, 29, and 39, at a Q_t of 100 µL/min (a) and 200 µL/min (b).

It can be seen from Figure 30 that the liposomes size distributions remain nearly unaffected after the gel filtration process within the investigated liposome diameter, ranging from approximately 60 nm to 90. The results show that no artificial selection for a particular vesicles diameter occurs during the filtration process and the filtered liposome sample represents the liposome size distribution obtained during the formation process in the microchannel.

5.3.2 Free SRB Dye Fluctuations

The gel filtration process is sufficient for removing free SRB from the liposome sample. Nevertheless, a small quantity of free SRB is often detectable. The fluorescent contribution of the free SRB is negligible when the liposomes encapsulate a large number of SRB molecules. However, in the case of low SRB loading into the liposomes, the background SRB component can become significant, as is shown in Figure 31. As mentioned before, FCS allows extracting the background SRB concentration. To estimate the free SRB concentration it is important to ensure that the fast component of the FCS measurement truly originates from external SRB in PBS and not from internal fluctuation of SRB inside liposomes as the vesicles translate across the focal volume.

In order to prove that the background SRB concentration in our FCS measurements originates from freely diffusing SRB in PBS outside the liposomes and not from fluctuations of SRB inside the liposomes we add PEG-6000 at a concentration of 10 % by weight to the sample. PEG-6000 does not permeate through the liposome membrane; hence, it will increase the viscosity of PBS only outside but not inside the liposomes.

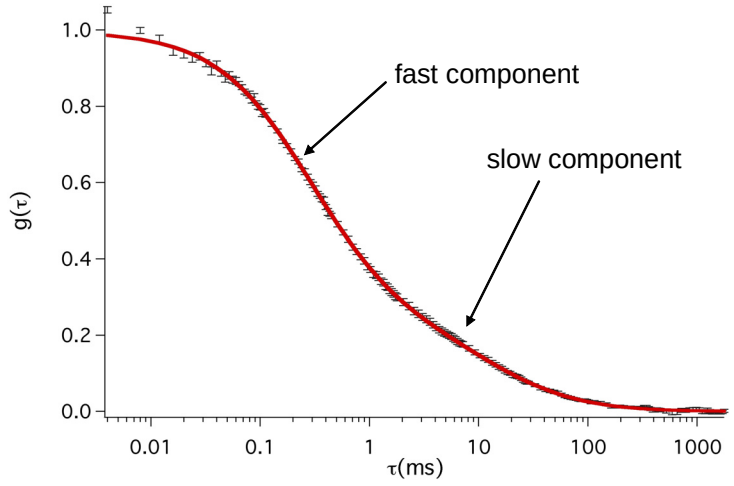

Figure 31 ACF from FCS measurements of liposomes with low SRB concentration fitted to a two component fit.

Figure 32a shows the fast dye component FCS data for free SRB in PBS and with addition of PEG-6000 to PBS at a concentration of 10% by weight. The addition of PEG-6000 increases the viscosity of the exterior PBS and increases the diffusion time of the contained particles. An FCS measurement is performed on a liposome sample before and after the addition of the PEG-6000. It can be seen from Figure 32b that the liposome solution fit before the PEG addition has a fast component that matches the same time constant as the free dye in solution. The liposomes after the PEG addition shows the fit is best performed with the slow diffusion component. This is direct evidence that the fast component in the FCS measurement of the liposome sample indeed stems from background dye diffusing in the exterior PBS and is not due to fluctuations of SRB encapsulated within liposomes.

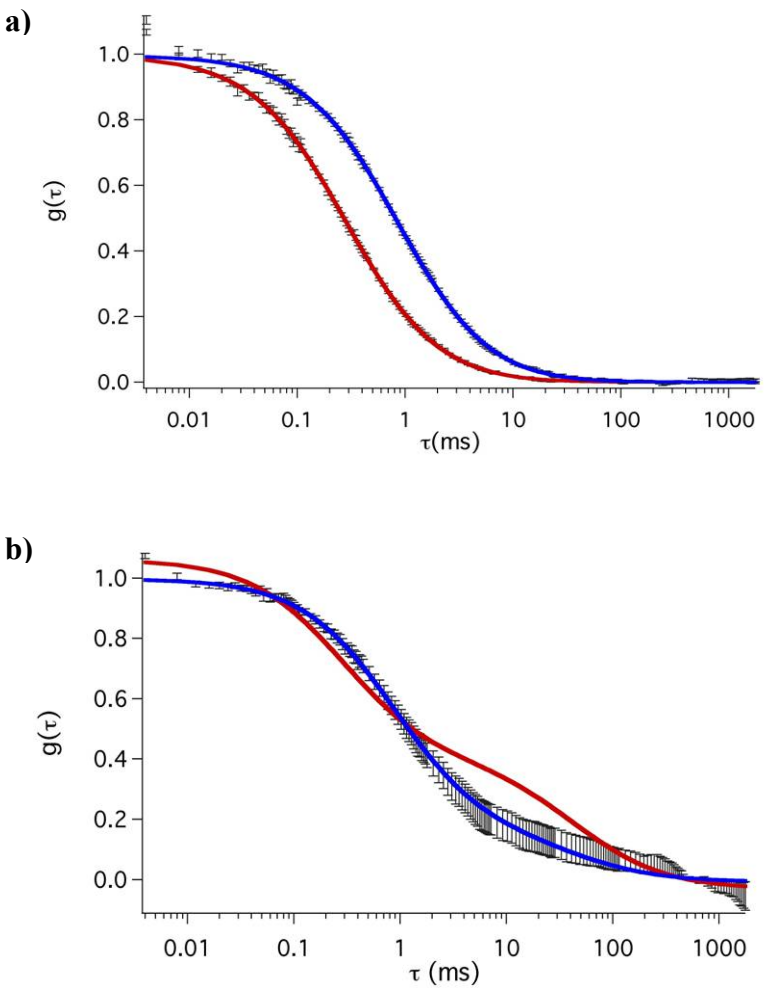

Figure 32 (a) Free SRB in PBS at 1 nmol/L concentration (red curve with τ=280 µs) and mixed with PEG-6000 at 10% by weight (blue curve with τ=850 µs). The addition of PEG-6000 increases the viscosity and therefore decreases the diffusion of SRB. (b) Liposomes formed at a SRB concentration of 500 nmol/L in PBS and subsequently mixed with PEG-6000 at a concentration of 10 % by weight. The data is fit with a fast component (red curve with τ=280 µs) and slower component (blue curve with τ=850 µs). The fit strongly suggests the fast dye component is affected by PEG-6000, which suggests that the fast component originates from free SRB and not from SRB encapsulated inside liposomes.

5.3.3 High Encapsulation of Low Concentrated SRB in Nano-liposomes

The encapsulated SRB concentration in liposomes versus the SRB concentration dissolved initially in PBS was investigated for 60 nm and 80 nm vesicles at initial SRB concentration in PBS ranging from 500 nmol/L to 250 µmol/L. SRB is a is membrane impermeable zwitterionic fluorophore with a net charge of zero at neutral pH (~7.4).[97] The maximum non-selfquenching SRB concentration is limited to about 1 mmol/L of SRB in PBS. The maximum SRB concentration is a result of increasing background SRB after gel filtration and a maximum brightness of the liposomes measurable with the used avalanche photo diode (APD). Higher concentration can certainly be encapsulated but require an optical density filter that reduces the fluorescence signal to avoid damage of the sensitive avalanche photo diodes. Furthermore, SRB quenching needs to be considered at higher loading concentrations. Figure 33 the liposome size distribution is shown for the 60 nm and 80 nm vesicles produced at a FRR of 19 and 49.

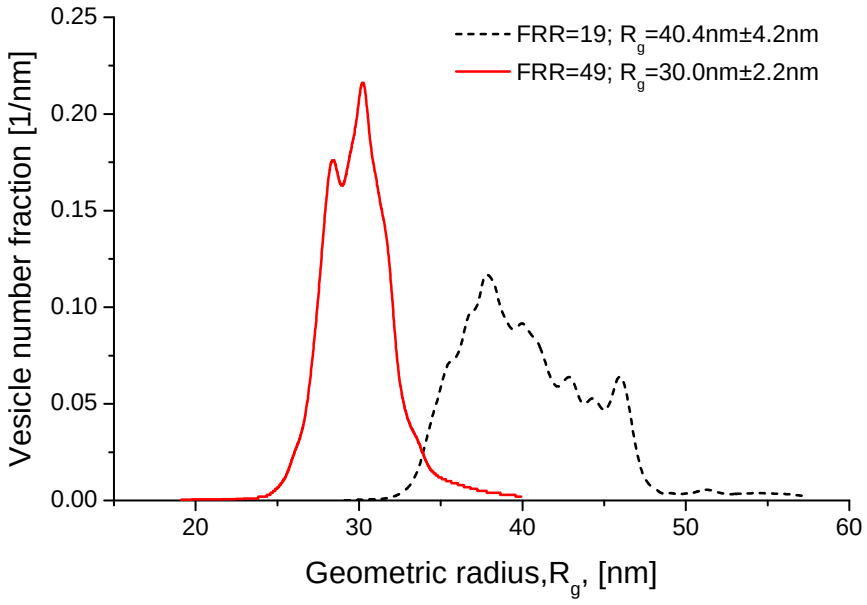

Figure 33 Vesicle size distributions obtained at a Q_t of 100 µL/min and a FRR of 19 and 49.

It can be seen from Figure 34a, that the SRB concentration in the 80 nm vesicles amounts to approximately 39 % of the initial SRB concentrations within 10mmol/L and 100 µmol/L dissolved in PBS. In between we can see that the concentration of encapsulated SRB is slightly higher but always below the starting concentration of SRB in PBS. However, as can be seen in Figure 34b, the 60 nm vesicles show an unexpectedly high SRB concentration that exceeds the starting concentration of SRB dissolved in PBS at SRB concentrations below 100 µmol/L. Notice the experimental data approaches zero, which suggests the Poissonian loading assumption is valid and also, that the molecular brightness is unaffected by being encapsulated in the liposomes. A single encapsulated SRB molecule appears as bright as a single free SRB molecule in PBS.

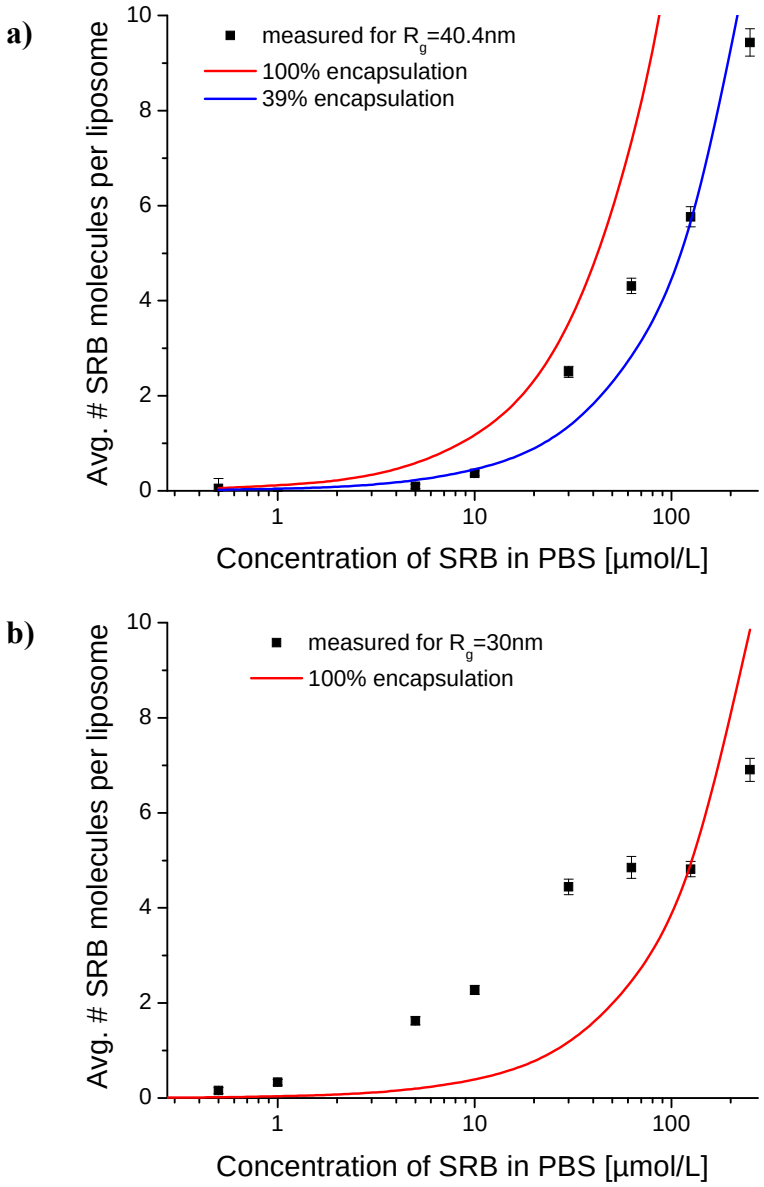

Figure 34 Average number of encapsulated SRB molecules in 80 nm (a) and 60 nm (b) diameter vesicles. The red curve represents the number of encapsulated SRB molecules where the concentration in the liposome equals the starting concentration of SRB in PBS. The blue curve is the best weighted fit for encapsulated SRB that amounts to 39 % of the SRB concentration in PBS. The error bars show the 95% confidence interval calculated by multiplying the error propagated standard deviation by 1.96 and dividing by the square root of number of 10-second intervals measured for a given loading concentration (generally 25 sets).

The higher SRB concentration in the smaller vesicles, although not yet confirmed, may be due to a spatial SRB concentration enhancement induced by viscous anisotropy and partitioning of SRB in the microchannel as IPA mixes with aqueous solutions. The number of encapsulated SRB molecules generally increases with increasing SRB concentrations. The fluorescence measurement show that liposomes with a diameter of 80 nm encapsulate a slightly larger average numbers of SRB molecules than 60 nm liposomes at concentrations of SRB in PBS > 100 μmol/L. This seems obvious considering that 80 nm diameter vesicles have an approximately 2.5-fold larger interior volume than 60 nm vesicles. Despite the larger aqueous interior of the 80 nm vesicles the number of encapsulated SRB molecules is only 50 % higher than that of the 60 nm vesicles (within the measured range) and therefore results in an overall lower SRB concentration than the SRB concentration in PBS for the larger vesicles. Considering the larger volume of the 80 nm vesicles it is surprising that the 60 nm vesicles encapsulate more SRB molecules when the SRB concentration in PBS falls below 100 μmol/L. From the simulation it can be seen in Figure 35 that the mixing of IPA and PBS in the sheathed flow results in a viscous anisotropy across the two mixing streams that is highly non-linear. The viscosity increases three-fold from the viscosity of PBS as it mixes with IPA. This viscous anisotropy and a possible partitioning of SRB between IPA and PBS could manifest in an SRB enhancement in the highly viscous region where the diffusion coefficient of SRB reaches a minimum. Investigations are currently underway to further validate this phenomenon.

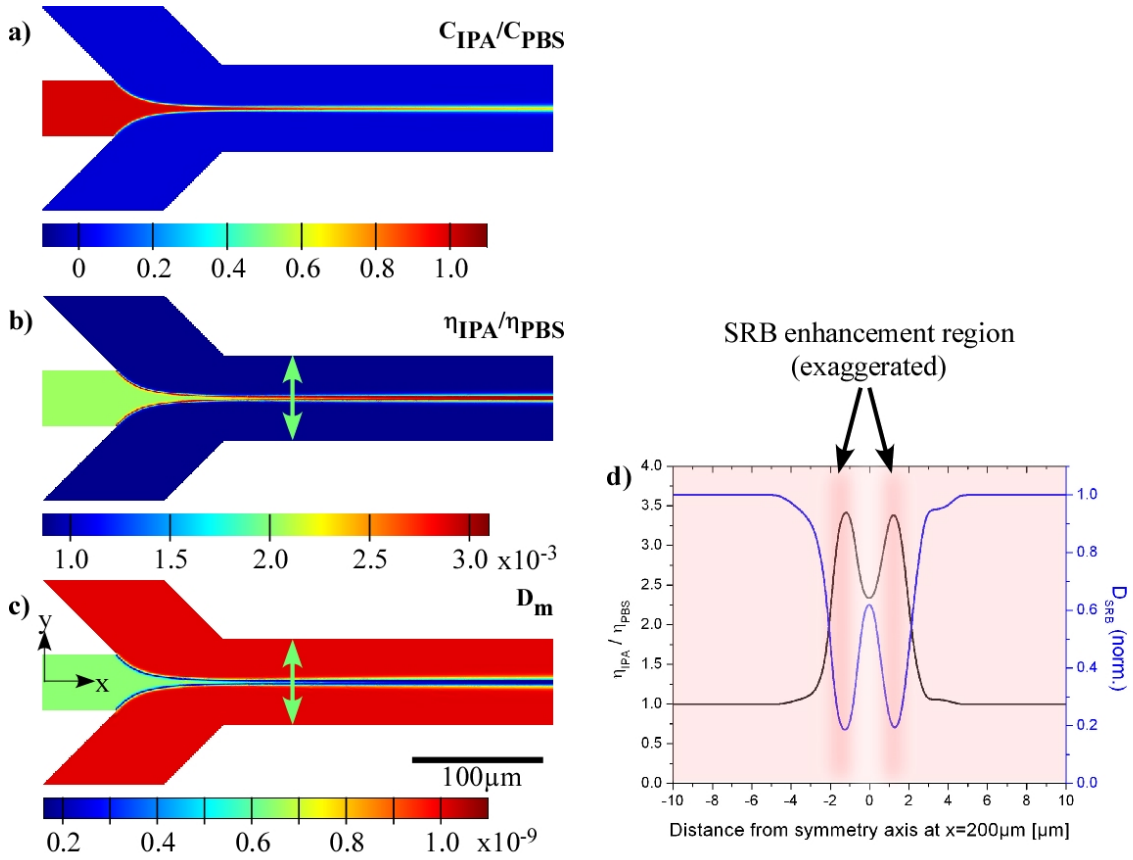

Figure 35 Simulation of IPA and PBS mixing during hydrodynamic focusing. The resulting concentration profile (a), viscosity distribution (b) and mutual diffusion coefficient (c) are shown for the mixing of IPA and PBS. The viscosity ratio and normalized diffusion coefficient for SRB within of the simulation in (b) and (c) are shown in the graph in (d). Greatly exaggerated shown is the enhancement of SRB as a results of viscous anisotropy and possible partitioning between IPA and PBS.

5.3.4 Reducing the Amount of Non-Encapsulated SRB with MHF

Control of the number of encapsulated SRB into liposomes was studied by injecting different volume fractions of SRB (2.5 v/v %, 5 v/v %, 10 v/v %, 20 v/v %, 30 v/v %, 40 v/v %) with a total VFR of 200 μL/min. The confocal fluorescence images in Figure 36 illustrate the fluorescence intensity of SRB for various PBS-to-SRB flow rate ratios. It can be seen that increasing the volumetric flow rate of SRB, while keeping the overall PBS flow rate constant, reduces the amount of mixing of SRB prior to the focusing region (see Figure 36). The degree of mixing between SRB and the adjacent PBS depends on the flow velocity, SRB-to-PBS flow rate ratio, and length of the channel section between the SRB injection and the center inlet channel over which mixing can occur. Figure 36d illustrates a side channel that is completely filled with SRB, which would be analogous to encapsulation with the batch solvent injection method, in which the buffer contains a homogenous distribution of the solute to be encapsulated into the liposomes. In addition to controlling the number of molecules loaded into the liposomes, a reduced volume fraction of SRB was determined that allowed encapsulation without adversely affecting the SRB concentration in the liposomes. Figure 37 shows the liposome size and size distribution obtained during the encapsulation studies. It further demonstrates the high reproducibility of liposome formation achievable in a microfluidic format.

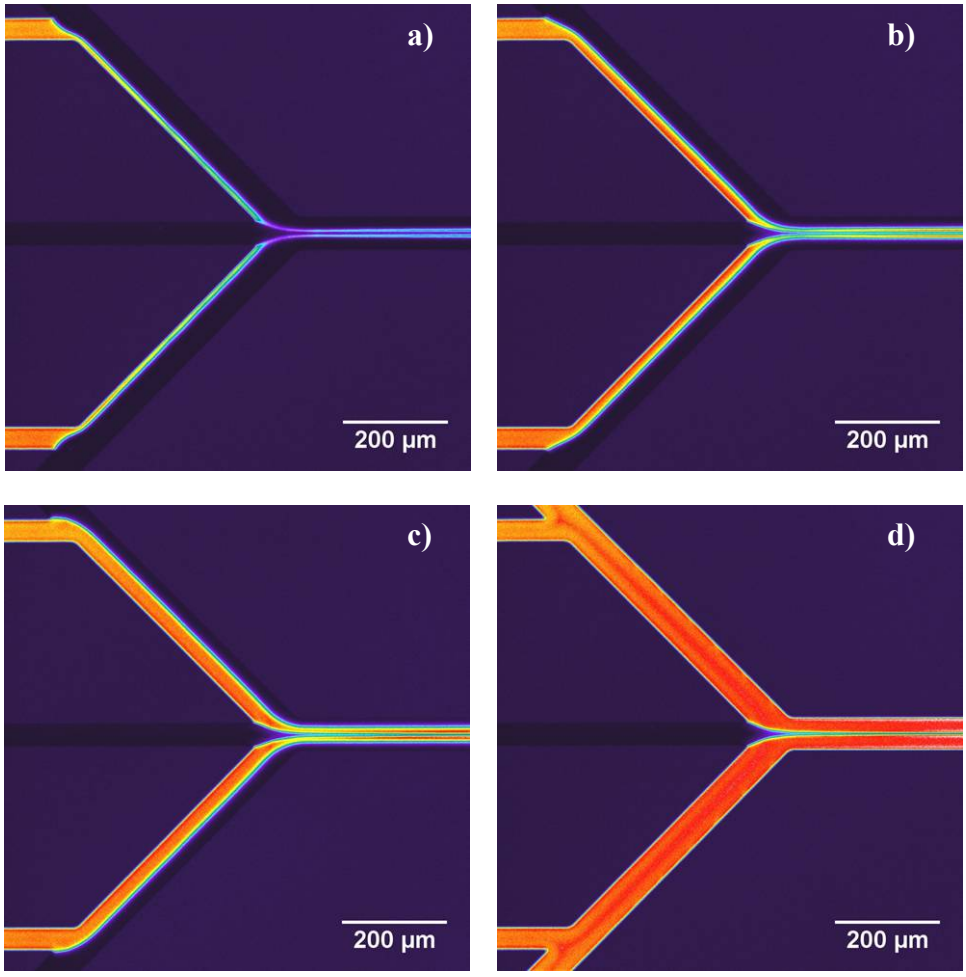

Figure 36 False-color confocal fluorescence micrograph of the microchannel network showing the fluorescent intensity of 0.5 mmol/L SRB in PBS injected into the left two inner side channels. PBS without SRB dye is injected into the left two outer side channels, and lipid mixture is injected into the left center channel. The total Q_t is 200 µL/min and the FRR is constant at 9. The SRB volume fractions shown are 5 % (a), 25 % (b), 50 % (c), and 100 % (d).

Figure 37 shows the normalized vesicle size distribution for a FRR of 35 and a Q_t of 200 µL/min at different volume fractions of SRB. It can be seen from Figure 37 that the vesicle size distributions remains approximately constant and the largest fraction of the vesicles have a geometric radius, R_g, which varies slightly between 29 nm and 32 nm.

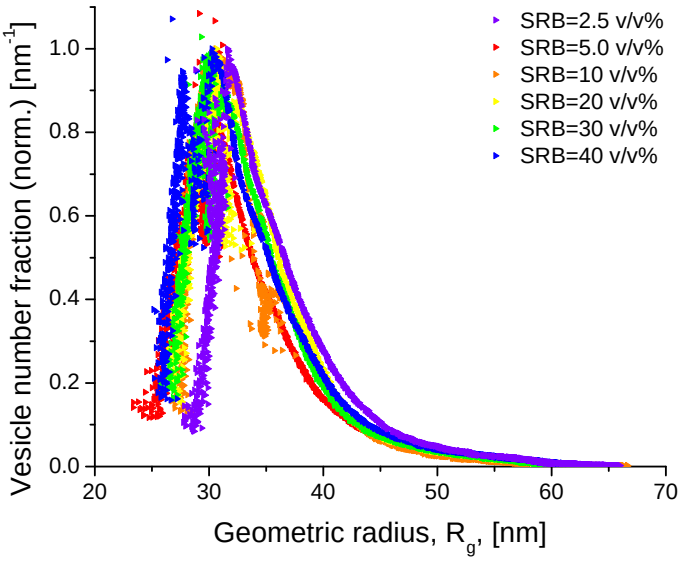

Figure 37 Similar liposome size and size distribution at constant Q_t of 200 µL/min and FRR of 35 for 6 different volume fractions of SRB in the total sample volume.

Figure 38 shows that the volume fraction of SRB can be reduced significantly before a moderate change in the amount of encapsulated SRB is detected. A 40-fold reduction in SRB content reduces the total number of encapsulated SRB molecules by about a factor of 2. In contrast to common batch fabrication methods, microfluidics has the ability to spatially localize the encapsulant to the immediate vicinity where encapsulation is expected and thereby reduce the encapsulant waste substantially without

adversely affecting the concentration of compound inside the liposome. Control of the encapsulated SRB concentration in liposomes can be achieved below 20 v/v % of SRB of the total sample volume. This allows for tuning the concentration of compound encapsulated in the liposome from an initial SRB concentration.

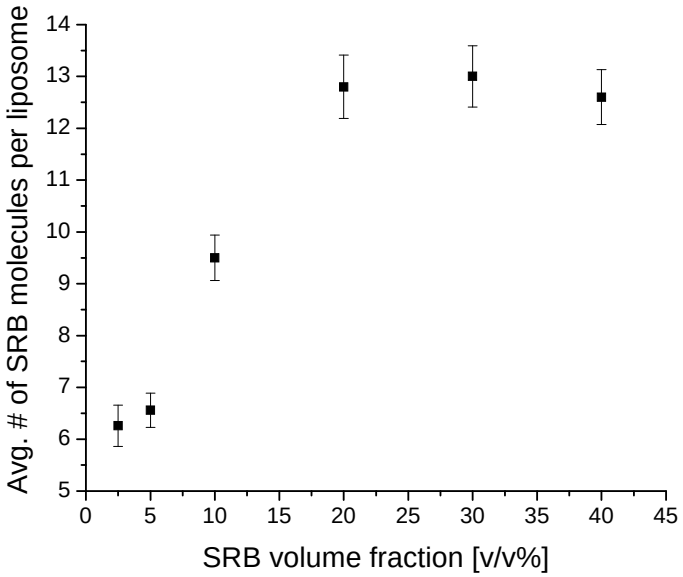

Figure 38 Data shows the number of SRB molecules per liposome along with the 95 % confidence interval. Reducing the SRB volume fraction reduces the number of encapsulated SRB molecules from about 14 to 7. Maximum encapsulation is already achieved at 20 % volume fraction of SRB in the channel, reducing the SRB waste by almost 80 %.

Varying SRB concentrations inside the liposomes are facilitated by the laminar flow conditions in the microchannel which enables controlled diffusive mixing at the liquid interfaces prior to mixing with the center stream. In macro-scale batch-processing

this can only be achieved by replacing the entire buffer volume. Filling all side-channels with PBS containing SRB is representative of common batch processing.

In addition to reduced sample consumption, which is desired from an economical standpoint, the continuous-flow microfluidic approach allows controlling the concentration of the substance to be encapsulated from an initial starting concentration *via* controlled diffusive mixing. This enables facile control of the concentration of encapsulated SRB into liposomes.

5.4 Summary

The formation of liposomes and encapsulation of a hydrophilic drug simulant (SRB) has been demonstrated using a microfluidic technique. Microfluidics enables reproducible and fine control over liposome size and size distribution, tunable loading of liposomes, and substantially reduced encapsulant consumption, without adversely affecting the encapsulation. The waste of compound (SRB) can be reduced significantly by confining it to the immediate vicinity where liposome formation and concomitant encapsulation occurs. The perturbation of the liposome size distribution after gel permeation chromatography is minute. Additionally, results showed an unexpectedly high loading of low concentrated SRB for small vesicles produced at high FRRs. It is hypothesized that viscous anisotropy and partitioning of SRB, as a result of the mixing between IPA and PBS, leads to diffusive retardation at locally high viscosities at the diffusive liquid-liquid interface and therefore spatial concentration enhancement of SRB. This new technique could yield an improvement over the generally low encapsulation efficiencies of liposomes observed with passive loading methods, especially with a

smaller channel design which increases the liposome concentration and thereby could further enhance the encapsulation efficiency.

The simplicity of this liposome formation and drug encapsulation strategy could allow for implementation in point-of-care drug encapsulation, eliminating shelf-life limitations of liposome preparation and reducing encapsulant consumption. Furthermore, fluorescence correlation spectroscopy in combination with fluorescence cumulant analysis provides a non-destructive approach to determine average loading efficiencies and has the potential for integration in future lab-on-a-chip applications and for online liposome characterization.

Chapter 6: Summary and Future Work

This dissertation demonstrates a novel microfluidic method to continuously produce liposomes with an average diameter in the range of 50 nm to 150 nm and controllably encapsulate a hydrophilic drug simulant. The liposome size range is relevant for drug delivery applications from the standpoint of clearance rate by the mononuclear phagocyte system and permeation through for example fenestrated tumor vasculature. Furthermore, the achievable liposome size range is also interesting for nanometer-scale confinement strategies in single molecule studies. A single or a few molecules can be compartmentalized in nanometer-scale liposomes which can be subsequently tethered to a surface while enabling free Brownian motion of the entrapped molecules. This is in contrast to common single molecules studies where the molecule of interest is tethered to a surface to facilitate long observation times.

The narrow liposome size distributions obtained with MHF do not require size-altering post-processing procedures which often decrease the yield of the liposome sample through further dilution. A comparison of liposome size distributions obtained with different methods is shown in Figure 39. It shows the liposome size distribution obtained with MHF without any further post-processing, after 11 cycles of membrane extrusion through a 100 nm pore filter at elevated temperatures, and with the cross-flow method by Wagner et al.[41].

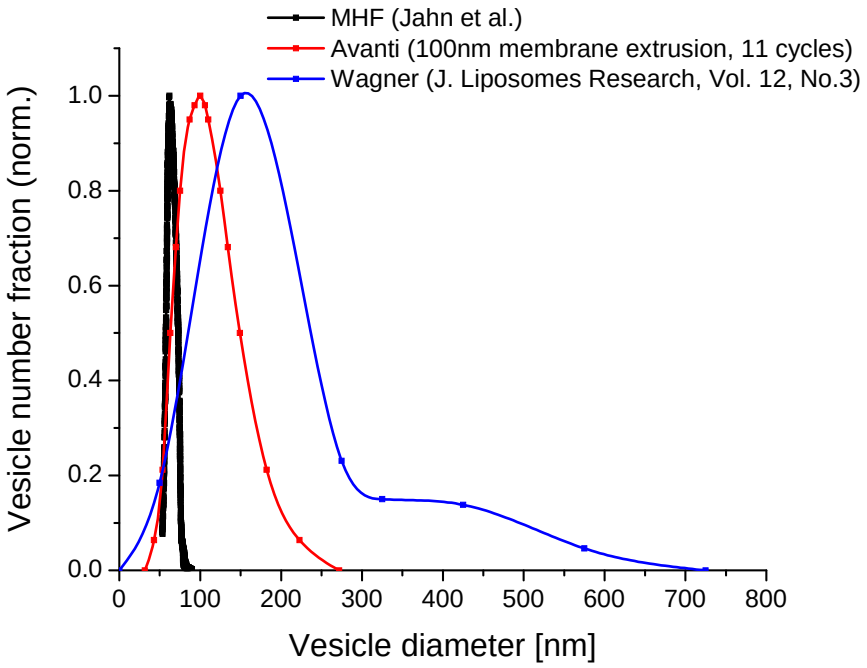

Figure 39 A comparison of liposome size distribution obtained with different methods.

The continuous-flow approach maintains a stable solvent/buffer concentration distribution. This is in contrast to the standard solvent injection method where the solvent concentration changes continuously during the injection process until the entire desired amount of solvent/lipid mixture is injected into the beaker. The liposome size distribution remains constant for a particular flow condition and channel geometry and can be continuously collected. The MHF method allows facile control over the liposome diameter by adjusting the FRR or Q_t that has not been reported with any other method.

A non-destructive methodology was developed to determine the true concentration of encapsulated SRB in liposomes using fluorescence fluctuation

spectroscopy. This technique can potentially be integrated into a microchip format and hence, can enable real-time on-chip characterization for purposes of quality control. It was shown that the encapsulation depends on the concentration of the compound in the mobile phase as well as the size of the liposomes. The loading behavior of the liposomes can potentially contribute to understanding the self-assembly process in the solvent injection method with MHF.

The comparison of different channel geometries and fluid dynamic parameters revealed that the liposome concentration can be increased by reducing the channel widths without affecting the liposome size distribution. The investigation of the channel geometry resulted in the distinction of liposome formation in convective and diffusive mixing regimes. Increasing the liposome concentration is especially interesting in regards to improving the encapsulation efficiency of compounds into liposomes. In addition, reducing the footprint of the microchannel network makes it more amenable to integration in lab-on-a-chip devices.

The MHF method pushes the benchmark in regards to reproducible liposome formation. Liposomes of constant diameter can be formed over extended periods of time as long as the hydrodynamic parameters are not varied, with the time only being limited to the size of the containers or syringes that contain the buffer and solvent.

Liposome formation with MHF provides predictable momentum and mass transport due to laminar flow and enables the investigation of non-observable parameter with fluid dynamics and mass transport simulations. A continuation towards molecular dynamics simulation may eventually elucidate the assembly process on a molecular scale.

The investigation of fundamental parameters instead of process parameter can help to increase the understanding of lipid self-assembly.

The facile control of lipid self-assembly into liposomes with MHF combined with highly sensitive (single molecule detection) fluorescence fluctuation spectroscopy showed an unexpected encapsulation behavior at low compound concentrations. The concentration of encapsulated compounds exceeds the initial concentration in the mobile phase. The origin of this phenomenon is not yet clearly understood and requires further investigation.

6.1 Future Work: Functionalizing Liposomes

The successful formation of liposome and encapsulation of compound was demonstrated with this technique. Future work will focus on two topics; (a) entrap medically relevant drugs into liposomes with MHF and conduct cell-uptake studies of these liposomes *in vitro* as well as with animal studies, (b) reconstitute membrane proteins into the lipid bilayer during the lipid self-assembly process with MHF.

Membrane proteins are key factors in many vital functions of the cell and their investigation is essential to understanding their ligand and signaling pathways which are fundamental for a wide spectrum of physiological processes.

The goal of the second project is to develop a microfluidic method for the screening of membrane protein inhibitors in a solution-based format. As an example of this screening of inhibitors of the cell surface receptor CD47 is envisioned. CD47 will be reconstituted into liposomes created by the MHF technique[47,48]. One of CD47 natural ligands is thrombospondin 1 (TSP-1); currently known as the only protein-ligand relationship that blocks physiologic nitric oxide (NO) signaling.[98] The control of the

regulatory function of TSP-1 on NO signaling is of paramount importance for the recovery from ischemic injuries and to overcome a deficit NO-responsiveness in aging.[98]

Microfluidically engineered liposomes carrying the reconstituted CD47 will be exposed to potential blocking agents; as the agent interacts with CD47 it will prevent the interaction of CD47 (and the liposomes attached to it) with a surface bound CD47 agonist of a liposome binding assay.[99] Currently, screening of potential therapeutic agents that block NO-signaling *via* CD47 is accomplished with cell culture assays[100] which lack efficiency and consistency, often cause false positives, are very elaborate, and add complexity because of the variable and somewhat uncontrolled nature of primary vascular cells. Engineered liposomes that have a controlled size, a high concentration of encapsulated marker, and that only display the membrane receptors for a specific application would provide a sufficient and simplified cellular mimic for a microfluidic binding assay.

The continuous-flow microfluidic chip shown in Figure 40 will be produced in low-fluorescence cyclic olefin copolymer (COC). COC is a halogen-free, high purity plastic that is known to be useful in diagnostic and medical devices.[101] Precision micro-milling of COC allows rapidly designing and optimizing a microchannel layout. Exposure of the COC microchannel network to O_3 allows it to easily bond to a glass microscope slide patterned with several molecules including CD47 blocking antibodies, TSP-1, or signal-regulatory protein α (SIRPα).[102]

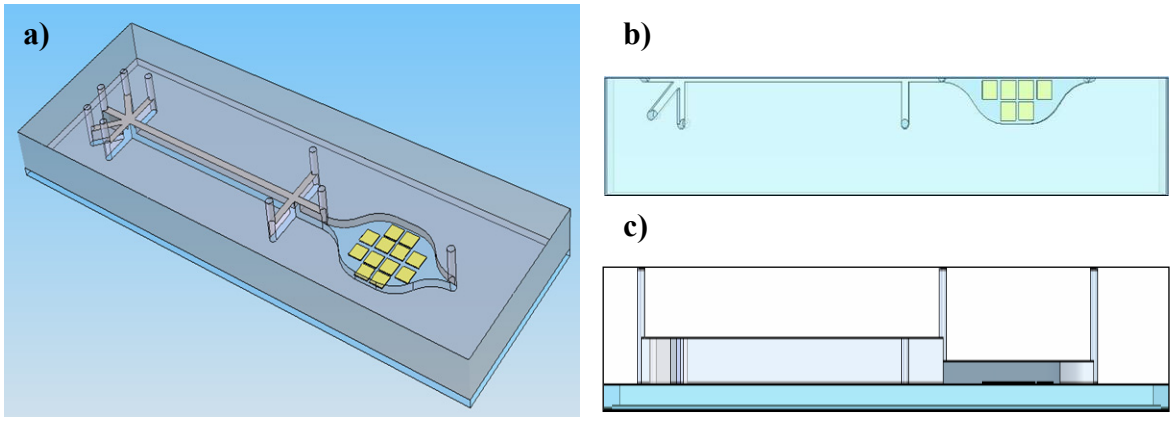

Figure 40 (a) Schematic of a microfluidic immunoassay that combines liposome formation, liposome functionalization with membrane bound proteins, immobilization of the liposomes to a specific target printed on a glass microscope slide, and fluorescent evaluation of fluorescent laden liposomes immobilized to its therapeutic agent. (b) Bottom view through the microscope slide of the assembled COC microchannel. (c) Cross section view along the symmetry line, showing the lower channel height in the immobilization chamber.

Two continuous-flow microfluidic methods are proposed to functionalize liposomes with CD47. CD47 is reconstituted either into preformed liposomes (two step process) or reconstituted during the lipid self-assembly into liposomes (one step process). The inhibition of CD47 is addressed by producing fluorescent/biotinylated liposomes from a lipid blend and reconstitute purified CD47 (readily available through the laboratory of Dr. David Roberts at NCI, NIH, Bethesda, Maryland)[100] in the lipid membrane. A schematic of the functionalized liposome containing either entrapped SRB or membrane intercalated biotin is shown in Figure 41.

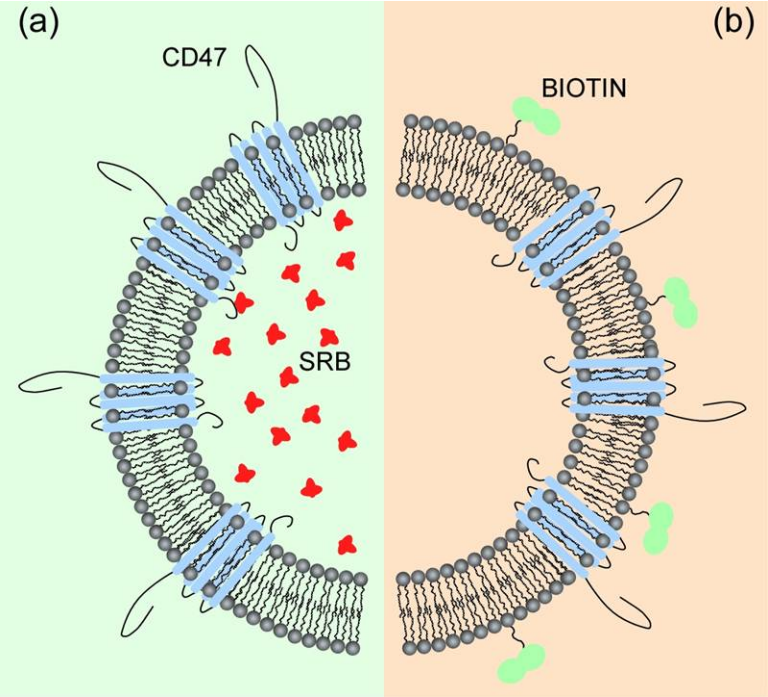

Figure 41 Liposome with reconstituted CD47 and encapsulated fluorophores (SRB) for fluorescent readout. (c) Liposome-CD47 complex with biotinylated lipids to which a horseradish peroxidase-streptavidin complex can be attached for a subsequent colorimetric readout.

In the two step process fluorescent liposomes with controlled average diameters from 50 nm to 150 nm are formed separately in a continuous-flow microfluidic device as previously demonstrated[47,48] and injected into the two inner side channels at the star-like intersection of the flow focusing device shown in Figure 40.

Secondly, phosphate buffered saline (PBS) containing soluble CD47 and a low concentration of a mild detergent (to prevent the aggregation of CD47), n-octyl-D-glucopyranoside (OG) is injected into the center channel and sheathed between the two adjacent buffer streams containing fluorescent liposomes. Alternatively, CD47 is

solubilized in the outer sheath-flow and the liposomes are injected into the center stream. The narrow streamwidth in both scenarios rapidly dilutes OG into the surrounding buffer solutions, similar to the detergent dialysis methods, originally developed for the reconstitution of membrane proteins with OG[103], to achieve subsequent intercalation of CD47 into the lipid membrane.

In the one step procedure a lipid tincture is injected into the center channel of the flow-focusing device and PBS containing soluble CD47 and a low concentration of OG is injected adjacent to the center lipid stream. CD47 reconstitution into the liposomes occurs during the lipid self-assembly process and can be optimized by either injecting PBS containing CD47 into the inner or the outer two side channels of the microfluidic device shown in Figure 40.

Incorporation of CD47 into the lipid membrane and determination of the binding constant will be evaluated with epi-fluorescence microscopy or colorimetrically as liposomes bind to surface tethered CD47 antibodies, TSP-1, SIRPα, or agonist peptides, *i.e.,* 7N3 or 4N1K[104,105].

A liposome binding assay will be used to optimize the process parameters for the reconstitution of CD47 into liposomes with microfluidics. For the colorimetric readout of the liposomes binding assay the lipid blend contains a low molar fraction of biotinylated lipids which are incorporated into the liposome during the lipid self-assembly process. CD47 antibodies, TSP-1, or SIRPα are adsorbed to a commercially available polystyrene microtiter plate according to standard protocols. The surface is then treated with (i) liposomes functionalized with CD47 and biotin that bind to the surface adsorbed proteins of interest and unbound liposomes are washed away; and (ii) a

solution containing the peroxidase-streptavidin complex. After the unbound enzyme-complex is washed away substrate is added to the wells. The product formation can be monitored colorimetrically. For the fluorescent readout SRB dissolved in PBS will be encapsulated into the aqueous interior of the liposome.

Highly fluorescent functionalized liposomes are suitable for future high-throughput screening of NO-signaling blocking agents in the volume-limited microfluidic domain where binding events will be evaluated with epifluorescent microscopy. Once the optimal parameters to reconstitute CD47 are developed the liposome-CD47 complex will be tested against a therapeutic agent to determine its functionality. This will be achieved with a liposome binding assay in which TPS-1, SIRPα, or CD47 antibodies are tethered to the surface of a polystyrene titer plate and functionalized liposomes as well as the therapeutic agent are added.

Appendix A

Gel Permeation Chromatography

Gel permeation chromatography is a method that allows separating molecules of different dimension based in their relative abilities to penetrate into a suitable stationary gel matrix. The stationary matrix consists of very small, uncharged porous particles and is packed into a column. Based on the pore size of the stationary phase different levels of separation can be achieved. In the context of this dissertation gel permeation chromatography is used to separate non-encapsulated fluorescent dye molecules from a sample containing vesicles with encapsulated dye. A mixture sample containing non-encapsulated fluorophores and vesicles with encapsulated fluorophores are added to the top of a column. As the mixture passes through the column the much smaller fluorophores penetrate into the porous gel beads and follow a convoluted pass through the bead while the larger vesicles remain in the mobile solvent phase and hence elute faster than the fluorophores. Figure 42 shows a cartoon of the separation process where the larger particles elute faster compared to the small fluorophores that are slowed down by their convoluted pass through the porous beads.

The technical grade fluorophore sulforhodamine B (SRB) (Sigma Aldrich) with a molecular weight of 580.6 g/mol is separated from the vesicles through a 5 mL polyacrylamide column with an exclusion limit for globular proteins of 6 kDa MWCO (Pierce, Rockford, IL, USA). The polyacrylamide column has a void volume of 1.75 mL and a wet bead diameter of 90 µm to 180 µm. The columns are flushed with 60 mL (at least 5 column volumes) of PBS at a flow rate of 150 µL/min to equilibrate the column. To obtain an optimal sample separation the sample size should not exceed 10 % of the

column volume. A sample of 500 µL is collected from the outlet of the microfluidic network and subsequently filtered through the polyacrylamide column. 2mL of pre-filtered PBS solution (PBS is filtered with a 0.2 µm filter) is added to the column after the 500 µL of sample has entered the gel. The initial 500 µL effluent is discarded as waste because it will not contain any vesicles since the column size has a volume of 1.75 mL of which 500 µL are sample. This approach reduces the dilution of the sample after gel permeation chromatography. The remaining 1.5 mL is collected in black 1.5 mL volume centrifugation tubes (Daigger, Vernon Hills, IL, USA) to prevent photobleaching of SRB by ambient light. After the separation is completed the columns are equilibrated with 60 mL of PBS to separate subsequent samples.

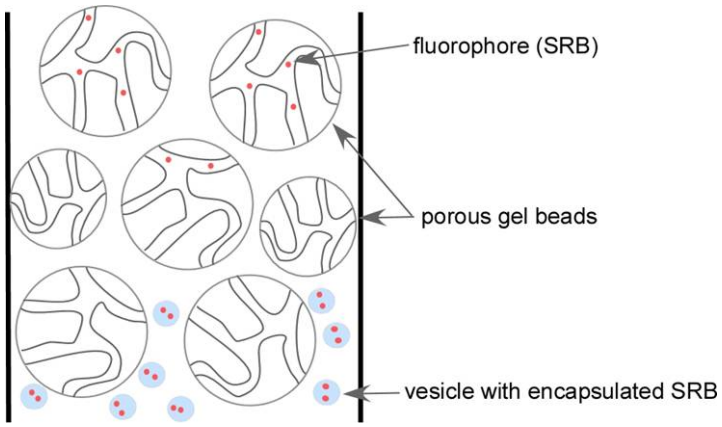

Figure 42 Schematic of the separation of a mixture of fluorophores and vesicles with encapsulated fluorophores based on their size.

Lightscattering

A variety of measurement methods exist to determine the average vesicle size. While the repertoire of methods is manifold, only few accurate and convenient methods that do not require assumptions about the fundamental nature of the particle size distributions are available. Transmission Electron microscopy (TEM) (e.g., cryo- and freeze fracture-TEM), sedimentation field-flow fractionation, nuclear magnetic resonance (NMR) spectroscopy, and static and dynamic light scattering are among these methods. TEM can introduce artifacts and is destructive of the liposome sample whereas sedimentation field-flow fractionation requires a complex centrifugation apparatus. Size exclusion chromatographic methods require column calibrations, often standards whose molecular weight values have been previously measured with light scattering.[74] Nondestructive methods based on dynamic light scattering and NMR can yield accurate average vesicles sizes but require user input of the size distribution functional form. The lack of complete understanding of the vesicle size distribution shape that results from various synthesis methods does not allow to measure the vesicle size distribution unambiguously with DLS or NMR.[106] However, combining a separation method, asymmetric flow field-flow fraction (AF^4) with continuous-flow multi-angle laser light scattering (MALLS), provides a convenient non-destructive method for measuring absolute vesicle size distributions without any prior assumptions about the nature of the distribution function form.

A great advantage of light scattering over other technologies for particle size analysis such as optical and electron microscopy, sedimentation, centrifugation, filtration, diffusion, size exclusion chromatography is that the system under study can be observed in situ without significant perturbations. The theory permits reduction of the data directly

to the final result without the need of secondary calibration schemes as often required in size exclusion chromatography. The measurements are almost instantaneous and can be recorded continuously so that rate processes may be followed.[107] Particle analysis by light scattering requires that the particles are randomly positioned in space and hence the system must be sufficiently dilute. The result of this dilution is that the scattering of an array of particles is incoherent, meaning that the phase shift of the scattered light by the particles is random and the scattering intensities are simply added. This assumption allows using the scattering function or form factor corresponding to an isolated particle.

Quasi-Elastic Light Scattering

Quasi-elastic light scattering (QELS), also known as dynamic light scattering, is a method to determine the average radius of a sample of vesicles in solution. In QELS rapid time-intensity fluctuation in the scattered light by the suspended vesicles are analyzed, which are a result of the Brownian motion of the vesicles in solution. The rate of the time-intensity fluctuations is directly related to the translational diffusion coefficient of the vesicles. Figure 43 shows schematically that the rate of the time-intensity fluctuations is inversely proportional to the vesicles size, in that smaller vesicles produce higher time intensity fluctuations and vice versa. While the analysis of QELS data is straightforward for monodisperse samples, it becomes more complicated for unfractionated polydisperse samples. Major limitations of QELS are its sensitivity to large vesicles in the dispersion and that it requires a priori assumptions of the size distribution of the vesicles in the sample.[108] It has been demonstrated by Wong et al., that if a dispersion containing 10 % or more of larger vesicles of a mixture of 20 nm and

90 nm diameter vesicles, the size detected by QELS is that of the larger 90 nm vesicles.[109] Due to successive improvements of computational analysis of intensity fluctuations, a priori assumption of the vesicle diameter distribution are not required anymore. However, the results remain still biased in favor of the larger vesicles in a polydisperse sample.[108] The size determined with QELS is therefore most meaningful if the sample is either monodisperse or fractionated according to the vesicle size before the measurement.

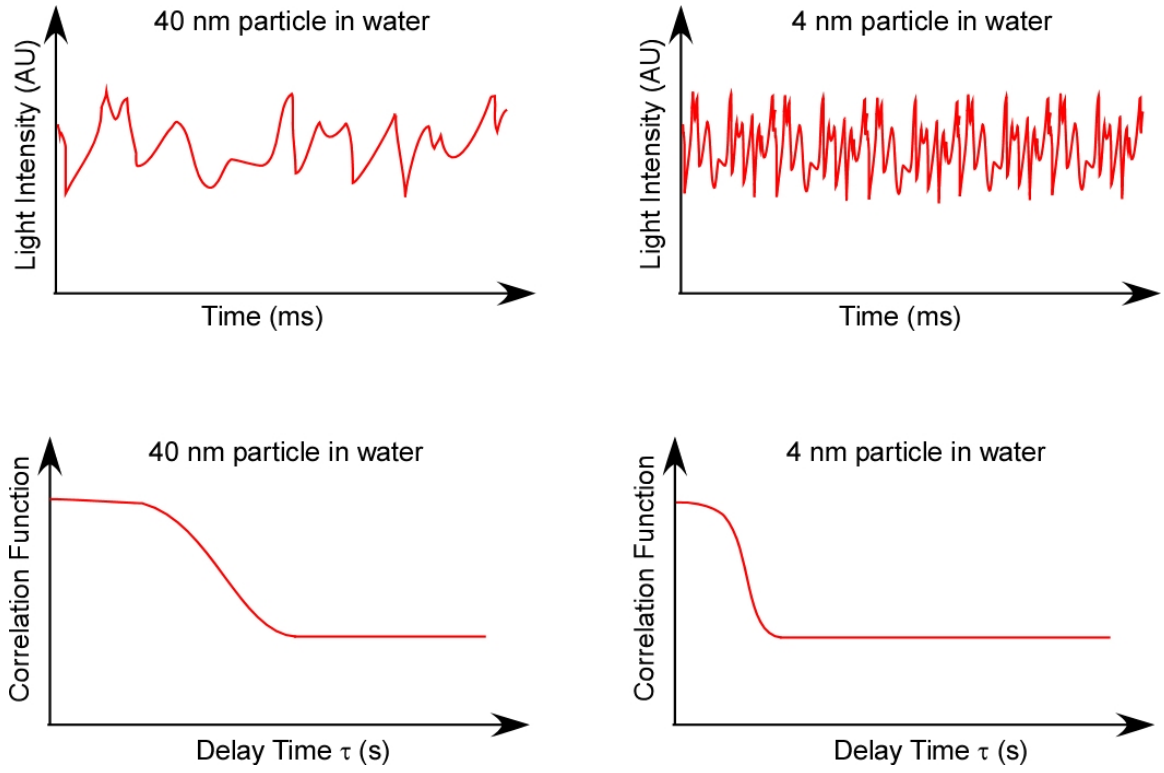

Figure 43 Schematic graphs of the light intensity fluctuations of 40 nm (a) and 4 nm (b) diameter vesicles in water showing the higher intensity fluctuation rate for the smaller vesicles. The graphs in (c) and (d) schematically show the respective auto-correlation function on a log time scale from which the diffusion coefficient can be derived.

The result of a QELS measurement is a second order correlation function

$$g(\tau) = \frac{\langle I(t) \cdot I(t+\tau) \rangle}{\langle I(t) \rangle^2}, \tag{6.1}$$

where *I(t)* is the scattered light intensity at a time *t*, and the brackets indicate averaging over all *t*. The correlation function *g(τ)* embodies all the information regarding the diffusion of vesicles within the sample being measured. It depends on the delay time τ, which is the amount that a duplicate intensity trace is shifted from the original before the averaging is performed. Fitting eq. 6.1 to an exponential decay function allows extracting the diffusion coefficient

$$g(\tau) = \beta + \alpha \cdot e^{-2q^2 \cdot D \cdot \tau}, \tag{6.2}$$

where β is the baseline of *g(τ)* at infinite delay, α is the correlation function amplitude at zero delay τ, *D* is the diffusion coefficient of the vesicles, and *q* is the scattering vector

$$q = \frac{4\pi \cdot n_0}{\lambda_0} \sin\left(\frac{\theta}{2}\right) \tag{6.3}$$

where n_0 is the refractive index of the solvent, λ_0 is the vacuum wavelength of the incident light, and θ is the scattering angle. A schematic representation of the auto-correlation function of a scattering intensity fluctuation is shown in Figure 40 where smaller particles have a shorter diffusion time and vice versa. The hydrodynamic radius R_h for a diffusing sphere is then interpreted from the diffusion constant *D via* the Stoke-Einstein equation

$$R_h = \frac{k_B \cdot T}{6\pi \cdot \eta \cdot D}, \tag{6.4}$$

where k_B is the Boltzman constant, *T* is the temperature, and η is the dynamic viscosity.

The integrated on-line WyattQELS instrument (Wyatt Technology, Inc., Santa Barbara, CA) applied in the continuous-flow system allows determining the hydrodynamic radii of vesicles ranging from 2 nm to 30 nm. The upper limitation of the hydrodynamic radius to 30 nm is due to the short residence time of the particles in the observation volume as they flow through the flow cell. While smaller particles below 2 nm generate a highly fluctuating intensity profile that can be auto-correlated within the short residence time in the observation volume, larger particles do not produce intensity fluctuation long enough to properly fit an autocorrelation function. Figure 44 shows the schematic of the QELS arrangement. The sample flows at a defined velocity through the bore of the flow cell. The laser is aligned such that the incident laser light passes through the same bore. The hydrodynamic radius is derived from the scattered laser light intensity fluctuations of the vesicle and is detected at a user-defined angle.

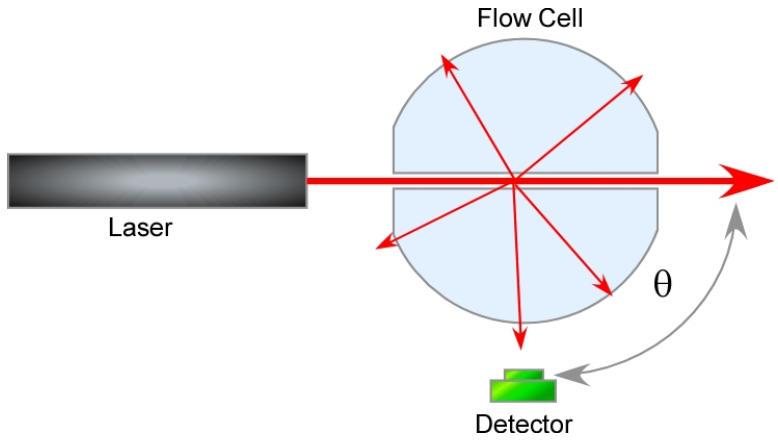

Figure 44 Schematic of the QELS detection configuration.

Multi-angle Laser Light Scattering

Multi-angle Laser light scattering (MALLS) is also known as static light scattering (SLS) and allows the determination of the size, shape, mass, and vesicle-solvent interaction of vesicles in solution. Instead of measuring the scattered light-intensity fluctuation rates as in QELS, MALLS measures the angular excess Rayleigh ratio of the laser light scattered from a dilute suspension of vesicles. The angular dependence of the excess Rayleigh ratio scattered by particles smaller than the wavelength of the incident light is described by the Rayleigh-Gans-Debye (RGD) approximation.[74] An expression for the vesicle size distribution can be derived from the expression of Zimm (1948) based on the fluctuation theory of light scattering[110],

$$R(\theta) = K \cdot M_v \cdot c_v \cdot P(\theta) \cdot \left[1 - 2 \cdot A_2 \cdot M_v \cdot c_v \cdot P(\theta)\right], \tag{6.5}$$

where $R(\theta)$ is the excess Rayleigh scattering (excess of scattered light intensity of the molecular solution above that scattered by the solvent itself), θ is the detector angle, M_v is the vesicle molecular weight, $P(\theta)$ is the vesicle scattering function (it relates the vesicle size and shape to the angular dependence of scattered light intensity), c_v is the vesicle concentration, A_2 is the second virial coefficient (it is a measure of the solute-solvent interaction), and K^* is a scattering coefficient for vertically polarized laser light,

$$K^* = \frac{4 \cdot \pi^2 \cdot n_0^2}{N_A \cdot \lambda_0^2} \cdot \left(\frac{dn}{dc}\right)^2 . \tag{6.6}$$

In eq. 6.6, dn/dc is the differential refractive index increment with respect to a change in vesicle concentration, n_0 is the refractive index of the solvent, N_A is Avogadro's number, and λ_0 is the vacuum laser wavelength.

The RGD approximation embodies the two basic principles of light scattering; (a) the intensity of light scattered is directly proportional to the product of the vesicle molecular weight and the vesicle concentration,

$$I_{scattered} \propto M \cdot c \cdot \left(\frac{dn}{dc}\right)^2, \tag{6.7}$$

and (b) the angular variation of the scattered light is directly related to the size of the molecule. The measurable quantity of light is the intensity (*I*), which is proportional to the square of the electric field amplitude (*E*), i.e., $I \propto |E|^2$. This RGD approximation is only valid if the incident wave remains essentially unaffected by the scattering molecule. This includes two important conditions:

1. The scattering molecule must be effectively indistinguishable from the refractive index of the solvent

$$|m-1| << 1, \tag{6.8}$$

where *m* is the refractive index of the solvated molecule to that of the solvent ($m=n/n_0$).

2. The scattering molecule must not disturb the phase of the incident laser light wave as it passes through the scattering molecule

$$\left[(4 \cdot \pi \cdot r \cdot n_0)/\lambda_0\right] \cdot |m-1| \cdot \sin(\theta/2) << 1, \tag{6.9}$$

where *r* is the characteristic radius of the molecule and λ_0 is the laser wavelength in vacuum.

The intensity of light scattered at a particular angle increases rapidly with particle size up to a maximum value and then oscillates in a complicated fashion as the size increases further. From this it follows that unless the particles are known to be isotropic

scatterers (particles that are smaller than the size at which the intensity becomes oscillatory with the angle of observation), a single measurement of the scattered intensity will not suffice to determine the particle size. This leads to the arrangement of multiple detectors circularly arranged in one plane around the observation volume, as is shown in Figure 45.

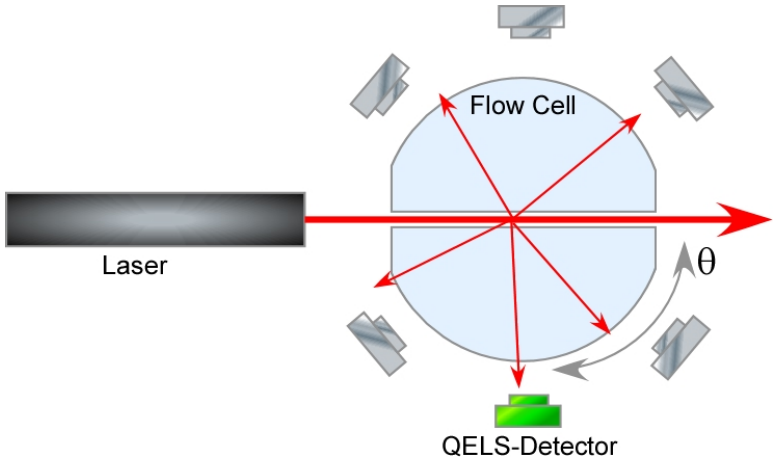

Figure 45 Schematic of the MALLS detection configuration showing one detector for QELS intensity fluctuation rate measurements. Multiple detectors for MALLS allow determining the scattering intensity as a function of the scattering angle.

Depending on the shape of the particle, different form factors $P(\theta)$ have been derived that describe the angular dependence of scattered light of a particle. The form factor $P(\theta)$ depends on the size of the particle, the wavelength of the light, and the observation angle. This means that particle size information can be obtained from the scattering intensity alone and no information of the concentration or *dn/dc* of the solute is nessecary.[74] Generally, to calculate the angular distribution of scattered light it is necessary to integrate over the contributions of each of the scattering centers (an extended particle can be visualized as a number of scattering centers distributed over a

center of mass). From the integration of the mass distribution over an extended particle the root mean square radius R_G (R_G is determined by integrating over the mass elements of the molecule with respect to the center of gravity of the molecule) can be obtained. If the shape of the particle is known (*i.e.*, sphere, rigid rod, random coil, etc.) than the R_G can be used to compute the geometric radii (R_g) or dimension. If the particle is much smaller than the wavelength of the incident light, less than 10 nm for 690 nm wavelength light, there will be no measurable angular variation of the light intensity in the plane perpendicular to the polarization axis. Particles this small can no longer be accurately measured in size but the molar mass can still be accurately determined.[74]

The form factor for a coated sphere model (Kerker 1969[107]) is,

$$P(\theta)=\left[\frac{3}{q^3\left(R_o^3-R_i^3\right)}\cdot\left(\sin qR_0-qR_0\cos qR_0-\sin qR_i+qR_i\cos qR_i\right)\right]^2, \tag{6.10}$$

where q is the scattering vector,

$$q=\frac{4\pi n_0}{\lambda_0}\sin\left(\frac{\theta}{2}\right), \tag{6.11}$$

and R_i and R_0 are the inner and outer vesicle radii.

Assuming a vesicle coating or bilayer thickness allows fitting the analytical formula of eq. 6.10 to light scattering data and determining the outer radius R_0 of the vesicle. Alternatively, a Zimm or Debye formalism can be applied, in which a polynomial is fitted to the light scattering data and allows determining the R_G, M_v, and A_2 of the suspended particles. The *rms* radius depends on the internal mass distribution of the molecules and is not generally a measure of the molecule's external geometry. Knowledge of the shape of the vesicle allows then to transform the *rms* radius into a conventional geometric radius (R_g).

Calibration

The scattered light results in a specific detector voltage, which is proportional to the light intensity. In order to measure the excess Rayleigh scattering $R(\theta)$ the detector voltages need to be calibrated with a solvent of known Rayleigh ratios to determine a configuration specific calibration constant (A_{CSCC}) that accommodates, for the laser wavelength, laser power, scattering volume, material and geometry of the flow cell, and solid angle of the detector with respect to the scattering volume. The calibration is performed at the 90º angle detector with reagent grade toluene filtered through a 0.02 µm pore filter. Toluene is a solvent that is very well characterized and the highest Rayleigh ratio of any comment solvent with 1.406×10^{-5} cm^{-1} at a wavelength of 632.8 nm.[111] The constant of A_{CSCC}, which depends on the solvent type and cell type (refractive index and geometry of the K5 flow cell), is automatically combined with an instrument constant that accounts for the geometry and material of the flow cell. It eventually provides a means to calibrate with a known Rayleigh scatterer and subsequently measure the Rayleigh ratio of different solute-solvent systems.

Normalization

In order to make meaningful measurements about the angular dependence of the scattering intensity, all detectors need to be normalized to the previously calibrated 90º detector, which by definition has always a normalization coefficient of 1. The normalization is performed with an isotropic scatterer (an isotropic scatterer scatters light equally in all directions) with a radius of less than 10 nm. Since the scattering angle is a function of the solvent refractive index, the normalization needs to be performed in the

same solvent as the samples that are analyzed. The normalization procedure with an isotropic scattered relates each detector's geometrical factor and sensitivity to the calibrated 90º angle detector. The normalization is generally performed with 5 kDa dextran dissolved in phosphate buffered saline.

Asymmetric Flow Field-Flow Fractionation

Asymmetric Flow Field-Flow Fraction (AF^4) separates particles based on size. AF^4 is a type of liquid chromatography, in which the separation takes place in a laminar flow without the use of a column media. The separation is caused by a field of force. In the method used the field of force is generated by a fluid cross-flow, in which the separation power can be adjusted with the magnitude of the cross flow. This method allows separating particles from about 1 nm to several 1000 nm thereby covering the size of liposomes under investigation. The application of AF^4 allows determining the true particle size distribution and characterization from MALLS as it can separate a polydisperse vesicle population into monodisperse fraction subsequently analyzed with MALLS. It is a non-destructive method that generates only minimal shearing and perturbation of the particles. Figure 46 shows a schematic of the AF^4 channel.

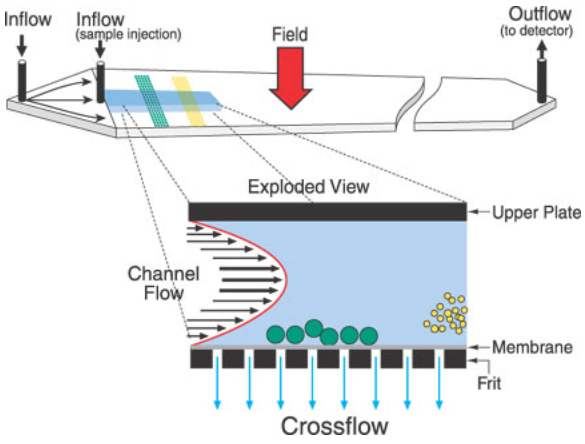

Figure 46 Schematic separation geometry of the flow field-flow fractionation channel. The smaller particles having a greater diffusion coefficient diffuse further into the parabolic flow stream and elute first.[112]

The channel consists of a 250 µm thick PEEK spacer and a top and bottom plate that are bolted together. The upper channel plate is impermeable, while the bottom channel is made of a permeable porous frit material. A thin cellulose membrane with a size barrier of 10 kDa covers the bottom plate and retains the vesicles while the mobile phase can permeate through.

The pressure driven flow in the channel produces a parabolic laminar flow field across the spacer height with the maximum velocity at the center of the spacer height and decreasing flow velocities towards the upper and lower channel plate. As the perpendicular flow force field is applied to the longitudinal laminar stream, the vesicles are driven towards the lower plate or "accumulation wall" by a drag force exerted by the perpendicular flow field according to Stoke's law. Diffusion of the particles associated with the Brownian motion creates a counteracting motion. The particles will reach an equilibrium height in the channel, which depends on the sum of the two forces. Smaller particles, which have a higher diffusion coefficient, tend to reach an equilibrium position higher up in the channel and therefore at a higher longitudinal flow velocity in the channel than larger particles. The parabolic flow velocity profile inside the channel then separates different sizes of vesicles and smaller vesicles elute earlier than larger vesicles. The separation can be divided into three basic steps; a) sample introduction, b) sample relaxation, and c) sample separation. Figure 47 shows each individual step and the respective signal for a fractionated sample schematically.

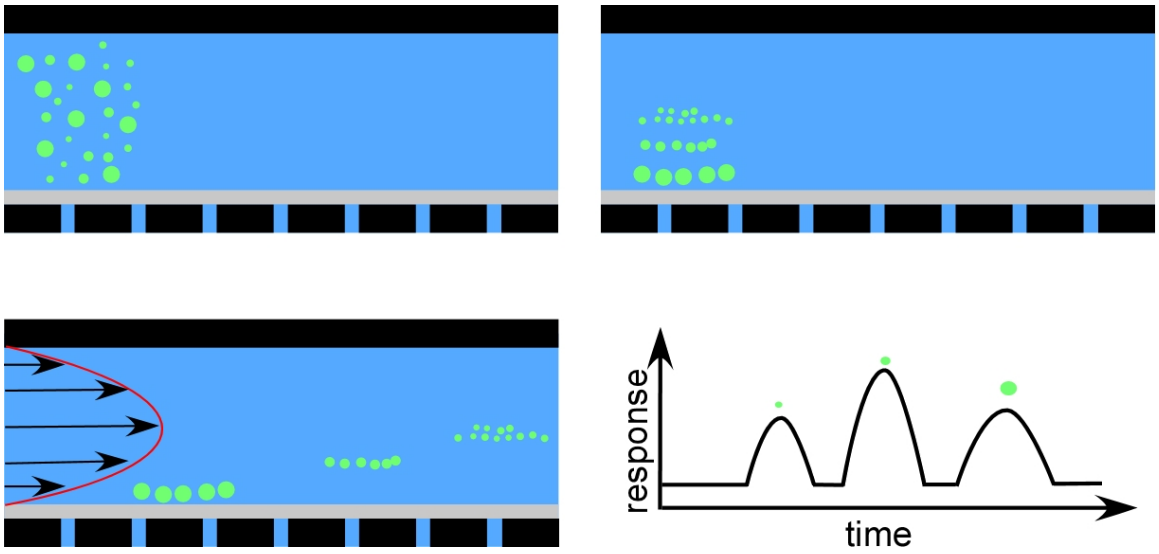

Figure 47 Schematic of the separation principle. a) The sample is introduced; b) the vesicles reach a equilibrium height over the lower wall; c) the elution speed correlates with the equilibrium height according on the force balance; d) smaller vesicles elute prior larger vesicles.

While AF4 allows one to determine the diffusion coefficient and hence the hydrodynamic radius based on the retention time of the eluting samples, it is solely applied to fractionate an initially polydisperse sample according to the vesicle size. The size analysis of the monodisperse vesicle fractions is subsequently performed with static and dynamic light scattering.

Separation Method with AF^4

High-resolution size-based separation of the liposome population is carried out using AF4 with multi-angle laser light scattering (MALLS) and quasi-elastic light scattering (QELS) detection and characterization (model DAWN EOS and QELS, Wyatt Technology, Inc., Santa Barbara, CA). A vendor-supplied spacer (250 µm thickness) is

used to define the flow channel thickness with a 10 kg/mol MWCO regenerated cellulose membrane for the cross-flow partition (Millipore, Bedford, MA). Phosphate buffered saline (PBS) (10 mmol/L phosphate, 2.7 mmol/L potassium chloride, 138 mmol/L sodium chloride, pH 7.4, 3 mmol/L sodium azide) (Sigma Aldrich) solution is used as the carrier liquid in the separation. The flow is controlled with vendor-supplied software (Eclipse 2, Wyatt Technology, Inc., Santa Barbara, CA). The flow control parameters for the separation are shown in Figure 48. Prior to the separation the flow channel is cleaned from particulates of a previous run and a cross flow of 3 mL/min. A cross flow of 3mL/min is sufficiently high to exert a large enough drag force that even the smallest vesicles (*i.e.*, vesicle with a geometric radius of about 20 nm) do not elute prematurely. A sample volume of 100 µL is injected at a flow rate of 0.2 µL/min while focusing at 3 mL/min for 4 min. To ensure that the entire sample is injected into the separation channel 3 to 4 times the sample volume needs to be injected. The cross-flow is ramped linearly from 3 mL/min to 0 mL/min over 90 min while eluting the separated particles at 1.0 mL/min.

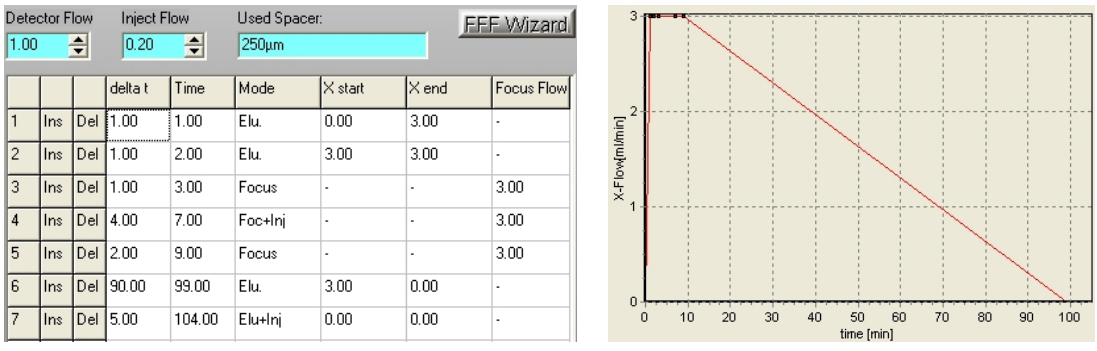

Figure 48 AF^4 injection and separation profile.

The radii of the eluted fractions are monitored using the MALLS and QELS detectors with data processing using software supplied by the vendor (ASTRA, Wyatt Technology, Santa Barbara, CA). MALLS intensity is measured at 15 angles simultaneously. The sample is measured at 1 s intervals for the MALLS and 5 s intervals for the QELS. The autocorrelation function of the QELS is fitted to a single-mode exponential decay model to determine the hydrodynamic radius. A coated sphere model (*i.e.*, a spherical structure with two radial regions of differing refractive index) showing good fit with the MALLS data is applied for size analysis of the geometric radius of the fractionated samples.

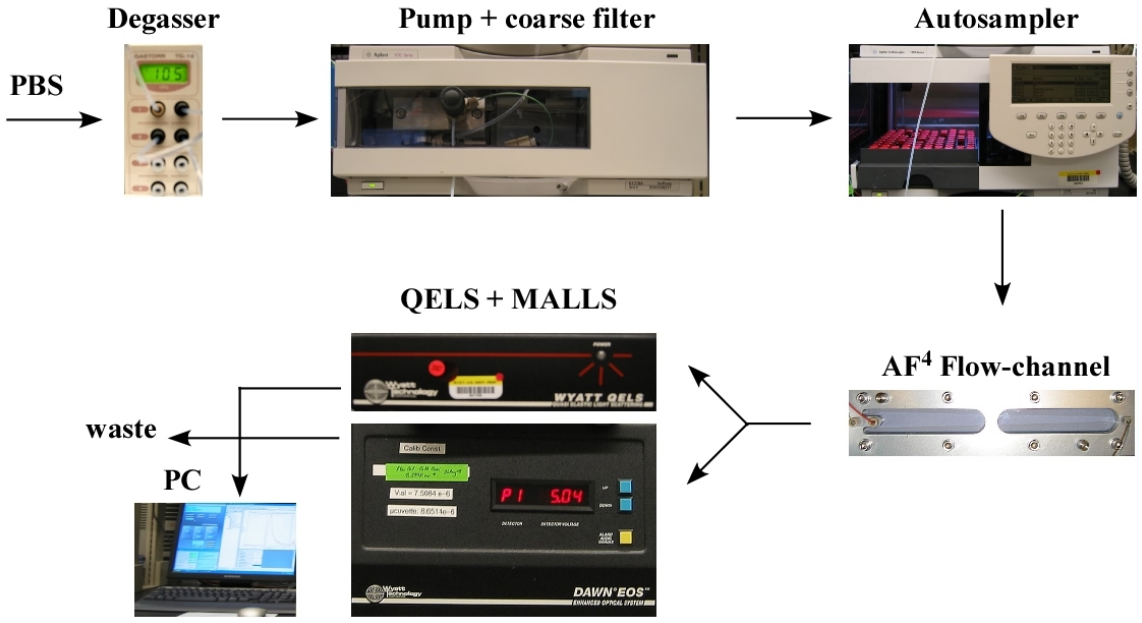

Figure 49 Light scattering and AF^4 set-up.

The schematic light scattering set-up shown in Figure 49 illustrates the arrangement of the used components to perform vesicle size distribution measurement. PBS is the mobile phase in which the vesicles are dispersed. PBS is first degassed and pumped through a coarse 1 μm and a fine 0.2 μm in-line filter combination to remove particulates in the mobile phase. The autosampler containing the vesicle samples injects a specified volume of the sample into the system, which is then carried with the mobile phase to the asymmetric flow field flow fractionation (AF^4) instrument, where the vesicles are fractionated and subsequently measured with the QELS/MALLS instrument. The light scattering data is then analyzed with a PC using vendor supplied software and the eluting sample is either discarded as waste or recollected.

Fluorescence Correlation Spectroscopy

Fluorescence correlation spectroscopy (FCS)[113,114] is a technique that can be used to determine the average concentration, hydrodynamic radii, diffusion coefficient, and kinetic chemical reaction rates of diffusing fluorescent particles,[115] based on measuring the second-order intensity autocorrelation function (ACF) of the fluorescence signal *P(t)*. In this work, it is assumed that the system consists of liposomes with encapsulated SRB and non-encapsulated freely diffusing SRB. The FCS analysis is applied to determine background SRB concentrations in liposome samples. It is assumed that *P(t)* is a stationary process which leads to a normalized ACF given by,

$$G(\tau) = \frac{\langle P(0) \cdot P(\tau) \rangle}{\langle P \rangle^2} \quad , \tag{6.12}$$

where the angular brackets ⟨ ⟩ indicate a time average, *P*, is the fluorescence signal as a function of time, and τ is the delay time.

Extracting useful information from an FCS measurement requires knowledge of the diffusion properties of the particles and the shape of the excitation volume. For confocal microscopy the shape of the excitation volume depends on the laser beam, the microscope objective, the confocal pinhole, and the detector. The instrument point spread function (PSF) describes the way in which light is transformed as it passes through and optical system. The volume created in solution from the laser beam focused by the confocal microscope set-up can be described by a three-dimensional Gaussian excitation volume given by[116],

$$\overline{PSF}_{3DG(x,y,z)} = \frac{I_{(x,y,z)}}{I_0} = \exp\left[-\frac{2 \cdot \left(x^2 + y^2\right)}{w_0^2} - \frac{2 \cdot z^2}{z_0^2} \right] \quad , \tag{6.13}$$

with an effective beam waist z_0 in the axial direction, a beam waist of the excitation profile w_0, and an excitation intensity I_0 at the center of the PSF. This simple model has some deficiencies, as in many cases it apparently does not describe the shape of the excitation volume accurately and can introduce artifacts that manifest as, for example, apparent additional diffusing species in the solution, or some type of nonstandard diffusion.[117] Hess *et al* suggests that the near three-dimensional PSF can be achieved by underfilling the back-aperture of the microscope objective and by using a small confocal back aperture[117], as is done in this work. Hence, the previous assumption of a 3-D Gaussian excitation volume is appropriate for this work. The 3-D Gaussian excitation leads to the following expression for the ACF of a multi-species system[115]

$$G(\tau) - G(\infty) = \sum_k \frac{G_k(0)}{\left(1 + \frac{\tau}{\tau_{D_k}}\right) \cdot \sqrt{1 + \frac{w_0^2 \cdot \tau}{z_0^2 \cdot \tau_{D_k}}}} \tag{6.14}$$

where, τ_{Dk} is the k^{th} species' diffusion time through the observation volume, G_∞ is the long time result for G_∞ having a theoretical value of 1, and $G_k(0)$ is related to the concentration and brightness of the k^{th} species in the following way,

$$G_k(0) = \frac{N_k \cdot x_k^2}{\langle P \rangle^2} \tag{6.15}$$

The fluctuations of the fluorescence signal stem from changes either the number of fluorescent particles or the number of photons per particle and per second in the excitation volume. A binary mixture of free SRB and liposomes that are equally bright (note: for the FCS analysis, only the background dye is of interest but not the distribution in liposome brightness) leads to the following expression from eq. 6.14,

$$G(\tau) = G_\infty + \frac{G_{SRB}(0)}{\left(1+\frac{\tau}{\tau_{D_{SRB}}}\right)\cdot\sqrt{1+\frac{w_0^2\cdot\tau}{z_0^2\cdot\tau_{D_{SRB}}}}} + \frac{G_{lip}(0)}{\left(1+\frac{\tau}{\tau_{D_{lip}}}\right)\cdot\sqrt{1+\frac{w_0^2\cdot\tau}{z_0^2\cdot\tau_{D_{lip}}}}} \tag{6.16}$$

An approximately 20-fold difference in the diffusion times exists between free SRB and liposomes, which is helps to extract $G_{SRB}(0)$ from the FCS signal, as shown schematically in Figure 50. The value of $G_{SRB}(0)$ and eq. 6.15 are combined to arrive at an estimate for the concentration of free SRB in the excitation volume.

Proper extraction of parameter estimates from FCS requires an accurate estimate of the error associated with the FCS measurement. Following Wohland *et al.*[118] the normalized FCS data, $g(\tau)$ is reported, such that $g(0)=1$ and $g_\infty = 0$,

$$g(\tau) = \frac{1}{N_S}\sum_{i=1}^{N_S}\frac{G_i(\tau)-G_{i,\infty}}{G_i(0)-G_{i,\infty}}, \tag{6.17}$$

where N_S is the number of data samples measured and the standard error of $g(\tau)$ is given by,

$$E[g(\tau)] = \frac{1}{\sqrt{N_s}}\sqrt{\frac{1}{N_s-1}\sum_{i=1}^{N_s}\left(\frac{G_i(\tau)-G_{i,\infty}}{G_i(0)-G_{i,\infty}} - g(\tau)\right)^2}. \tag{6.18}$$

The error in $g(\tau)$ is absent of any systematic errors that may cause a change in the average number of particles between measurement sets. This gives a more accurate estimate of the uncertainty in $g(\tau)$.

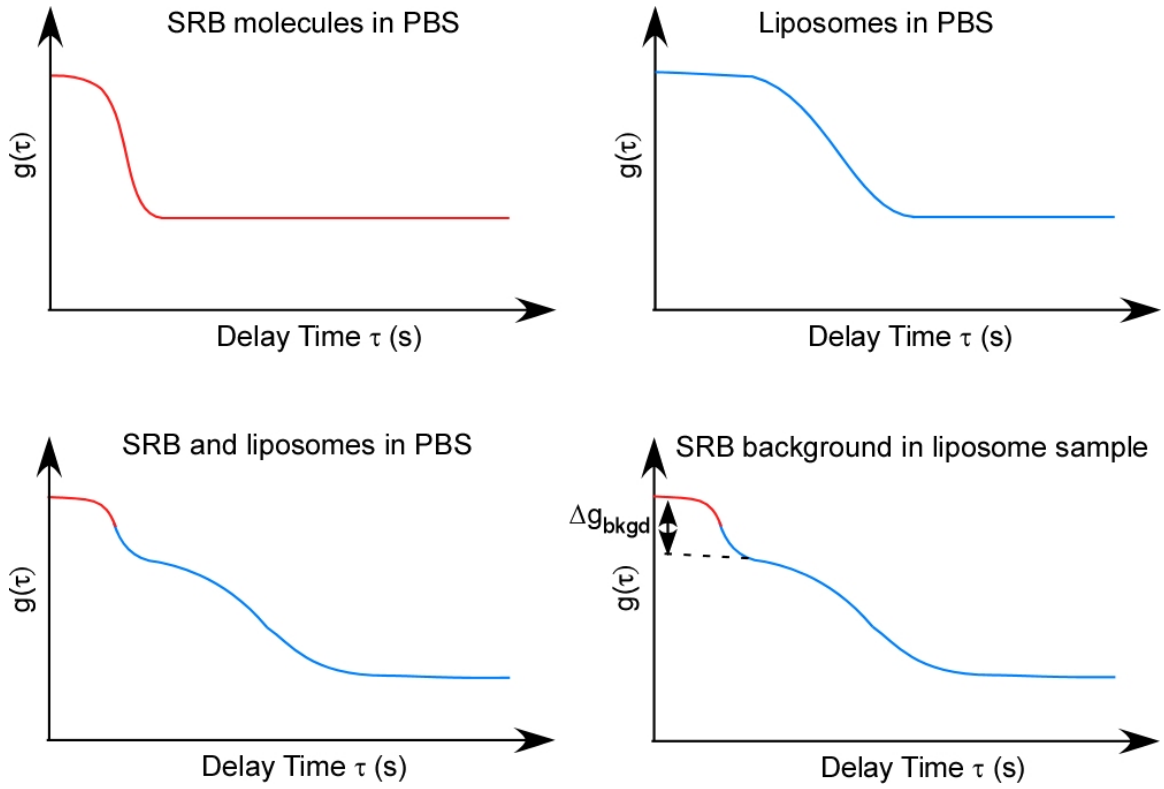

Figure 50 Schematic to determine background SRB concentration from FCS.

Fluorescence Cumulant Analysis

The study of the cumulants from a randomly fluctuation fluorescent field is a well established field.[81,94,96,119,120] Consider a tightly focused laser beam which creates a fluorescence excitation volume, *I(**r**)*, that is much smaller than the total sample volume. The sample contains *k* different, non-interacting, fluorescent species each having an average concentration and molecular brightness, given by c_k and q_k respectively. In the absence of shot-noise, the fluorescent molecules interact with the laser resulting in an ideal fluorescence intensity, $\Phi(t)$. Molecules diffuse randomly throughout the excitation volume which makes Φ a random variable. Therefore, it only makes sense to deal with the mean, $\langle\Phi\rangle$ and fluctuations about this mean, $\Delta\Phi = \Phi - \langle\Phi\rangle$ where $\langle\ \rangle$ represents a temporal average. The first two cumulants of Φ are related to c_k and q_k by

$$\langle\Phi\rangle = \chi_1 \sum_k q_k c_k, \tag{6.19}$$

$$\left\langle (\Delta\Phi)^2 \right\rangle = \chi_2 \sum_k {q_k}^2 c_k, \tag{6.20}$$

where $\chi_n = \int (W(r))^n d^3r$. The fluorescence intensity distribution, *W(r)*, depends on the excitation and collection intensity profiles of the microscope.

The fluorescence is measured by counting the number of photons arriving at a detector during an integration time, *t*. It is assumed that the integration time is small enough so that changes in a particle's position within the integration time can be neglected. The measured fluorescence introduces a shot noise contribution to the ideal fluorescence. A relation between the moments of the ideal and measured fluorescence is given by,

$$\left\langle (\Phi)^n \right\rangle = \langle P!/(P-n)! \rangle \tag{6.21}$$

where P is the number of photons detected per integration time. $\left\langle P^n \right\rangle$ is the n^{th} moment of the measured fluorescence. From eq. 6.21, the first two cumulants of the ideal and measured fluorescence are related as:

$$\langle \Phi \rangle = \langle P \rangle \tag{6.22}$$

$$\left\langle (\Delta\Phi)^2 \right\rangle = \left\langle (\Delta P)^2 \right\rangle - \langle P \rangle \tag{6.23}$$

Equations 6.19 and 6.20 relate the experimental parameters c_k and q_k to the ideal fluorescence. Equations 6.22 and 6.23 connect the ideal and measured fluorescence. Combining eqs. 6.19, 6.20, 6.22 and 6.23 allows extracting the relative brightness and absolute concentrations of a mixture of fluorescent particles from measurements of $\langle P \rangle$ and $\left\langle (\Delta P)^2 \right\rangle$.

The spatial profile functions, χ_n, are absorbed into the c and q parameters with the following substitutions,

$$a = \frac{\chi_1^2}{\chi_2}, \tag{6.24}$$

$$x_k = \frac{\chi_2}{\chi_1} q_k, \tag{6.25}$$

where a can be thought of as the excitation volume and x_k is the brightness of the k^{th} molecular species measured in photon counts per unit time. Substituting eq. 6.24 and 6.25 into eq. 6.19 and 6.20 leads to expressions linear in ac which are set equal to N, the average number of particles in the excitation volume,

$$\langle P \rangle = \sum_k N_k x_k + \langle P \rangle_B, \tag{6.26}$$

$$\left\langle (\Delta P)^2 \right\rangle - \langle P \rangle = \sum_k N_k x_k^2. \tag{6.27}$$

where $\langle P \rangle_B$ is the background count rate which is assumed to be Poissonian. Each liposome in a given ensemble contains an integer number, n, of SRB dye molecules (n = 0, 1, 2,…). It is assumed that the brightness of a particular liposome is given by nx_{SRB}. The amount of encapsulated compound across the liposome population is described with the brightness probability distribution, $\Pi(n)$. It is assumed that not all SRB in our sample is encapsulated inside the liposomes, but rather, some percentage of SRB is freely diffusing outside the liposomes. With these assumptions eq. 6.26 and 6.27 are written as following,

$$\langle P \rangle = N_{dye} x_{SRB} + N_{lip} x_{SRB} [n] + \langle P \rangle_B \tag{6.27}$$

$$\left\langle (\Delta P)^2 \right\rangle - \langle P \rangle = N_{dye} x_{SRB}^2 + N_{lip} x_{SRB}^2 [n^2], \tag{6.28}$$

where N_{dye} and N_{lip} are the average number of free dye molecules and liposomes (independent of n) in the excitation volume and

$$[n^x] = \sum_n \Pi(n) n^x. \tag{6.29}$$

The confocal microscope system is calibrated with a known concentration of SRB to determine the brightness of a SRB molecule, x_{SRB}. Combining eq. 6.27 with 6.28 we arrive at the following expression,

$$J = \frac{[n^2]}{[n]} = \frac{\left\langle (\Delta P^2) \right\rangle - \langle P \rangle - N_{dye} x_{SRB}^2}{x_{SRB} \left(\langle P \rangle - \langle P \rangle_B - N_{dye} x_{SRB} \right)} \quad . \tag{6.30}$$

Assuming all liposomes in a given sample are equally bright (a common assumption) is equivalent to setting $[n^2] = [n]^2$ and $J = [n]$ equals the average number of encapsulated

SRB molecules within a liposome. A more realistic assumption for the number of encapsulated molecules per liposome is given by a Poisson distribution ($[n^2] = [n]^2 + [n]$). From this distribution we find an expression for the average number of molecules per liposome,

$$[n] = J - 1 \quad , \tag{6.31}$$

which means the equal brightness assumption will overestimate the average number of encapsulated molecules by 1. This overestimate is especially important in the limit of low n.

Nomenclature

AC : Alternating current

ACF : Autocorrelation function

AF^4 : Asymmetric flow field flow fractionation

DDS : Drug delivery system

$DiIC_{18}$: 1,1-dioctadecyl-3,3,3,3-tetramethylindocarbocyanine perchlorate, non-polar fluorescent membrane dye

DMPC : Dimyristoyl phosphatidyl choline, lipid

DCP : Dicetyl-phosphate, anionic phospholipid bilayer component

DRIE : Deep reactive ion etching, anisotropic dry etching method

E.E. : Encapsulation efficiency

FCA : Fluorescence cumulant analysis

FCS : Fluorescence correlation spectroscopy

FRR : Buffer-to-solvent flow rate ratio

IPA : 2-propanol, isopropanol, lipid solvent

LP : Low-pass

MHF : Microfluidic hydrodynamic focusing

MALLS: Multi-angle laser-light scattering, for determining the geometric radius R_g

MWCO: Molecular weight cut-off

PBS : Phosphate buffered saline, hydration buffer for the lipid molecules

PCH : Photon counting histogram

PEG : Polyethylene glycol

QELS : Quasi-elastic light scattering, for determining the hydrodynamic radius R_h

SRB : Sulforhodamine B, water-soluble fluorophore

TTL : Transistor-transistor logic

R_G : Root mean square radius

R_g : Geometric radius, determined with MALLS

R_h : Hydrodynamic radius, determined with QELS

Re : Reynolds number

Q_B : Buffer (PBS) volumetric flow rate

Q_S : Solvent (IPA) volumetric flow rate

Q_t : Total volumetric flow rate

w_{fs} : Focused IPA/lipid stream width

Bibliography

1. Allen, T.M. & Cullis, P.R. Drug delivery systems: Entering the mainstream. *Science* **303**, 1818-1822 (2004).
2. Rawat, M., Singh, D. & Saraf, S. Nanocarriers: Promising vehicle for bioactive drugs. *Biological & Pharmaceutical Bulletin* **29**, 1790-1798 (2006).
3. Findley, F.K.a.G. The True Status of Drug Delivery Systems. in *The Drug Delivery Companies Report 2001* 66-68 (PharmaVentures Ltd., 2001).
4. Hung, L.H. et al. Alternating droplet generation and controlled dynamic droplet fusion in microfluidic device for CdS nanoparticle synthesis. *Lab on a Chip* **6**, 174-178 (2006).
5. Advanced Drug Delivery Systems: New Development s, New Technologies. 150 (Business Communications Company, 2006).
6. Lasic, D.D. Doxorubicin in sterically stabilized liposomes. *Nature* **380**, 561-562 (1996).
7. Innovation in Drug Delivery: The Future of nanotechnology and non-invasive protein delivery. in *Business Insights* (2006).
8. Torchilin, V.P. Recent advances with liposomes as pharmaceutical carriers. *Nature Reviews Drug Discovery* **4**, 145-160 (2005).
9. Lasic, D.D. Novel applications of liposomes. *Trends in Biotechnology* **16**, 307-321 (1998).
10. Gregoriadis, G. Immunological Adjuvants - a Role for Liposomes. *Immunology Today* **11**, 89-97 (1990).
11. Gregoriadis, G. Carrier Potential of Liposomes in Biology and Medicine .1. *New England Journal of Medicine* **295**, 704-710 (1976).
12. Alving, C.R. Liposomes as Carriers of Antigens and Adjuvants. *Journal of Immunological Methods* **140**, 1-13 (1991).
13. Bangham, A.D., Standish, M.M. & Watkins, J.C. Diffusion of Univalent Ions across Lamellae of Swollen Phospholipids. *Journal of Molecular Biology* **13**, 238-252 (1965).
14. http://nai.arc.nasa.gov.
15. Banerjee, R. Liposomes: Applications in medicine. *Journal of Biomaterials Applications* **16**, 3-21 (2001).
16. Kikuchi, H. et al. Gene delivery using liposome technology. *Journal of Controlled Release* **62**, 269-277 (1999).
17. Templeton, N.S. et al. Improved DNA: Liposome complexes for increased systemic delivery and gene expression. *Nature Biotechnology* **15**, 647-652 (1997).
18. Ramachandran, S., Quist, A.P., Kumar, S. & Lal, R. Cisplatin nanoliposomes for cancer therapy: AFM and fluorescence Imaging of cisplatin encapsulation, stability, cellular uptake, and toxicity. *Langmuir* **22**, 8156-8162 (2006).
19. Abraham, S.A. et al. The liposomal formulation of doxorubicin. in *Liposomes, Pt E*, Vol. 391 71-97 (2005).
20. Schmid, M.H. & Korting, H.C. Liposomes - a Drug Carrier System for Topical Treatment in Dermatology. *Critical Reviews in Therapeutic Drug Carrier Systems* **11**, 97-118 (1994).

21. Gulsen, D., Li, C.C. & Chauhan, A. Dispersion of DMPC liposomes in contact lenses for ophthalmic drug delivery. *Current Eye Research* **30**, 1071-1080 (2005).
22. Andresen, T.L., Jensen, S.S. & Jorgensen, K. Advanced strategies in liposomal cancer therapy: Problems and prospects of active and tumor specific drug release. *Progress in Lipid Research* **44**, 68-97 (2005).
23. Crosasso, P. et al. Preparation, characterization and properties of sterically stabilized paclitaxel-containing liposomes. *Journal of Controlled Release* **63**, 19-30 (2000).
24. Mayer, L.D., Krishna, R., Webb, M. & Bally, M. Designing liposomal anticancer drug formulations for specific therapeutic applications. *Journal of Liposome Research* **10**, 99-115 (2000).
25. Mamot, C., Drummond, D.C., Hong, K., Kirpotin, D.B. & Park, J.W. Liposome-based approaches to overcome anticancer drug resistance. *Drug Resistance Updates* **6**, 271-279 (2003).
26. Sadava, D., Coleman, A. & Kane, S.F. Liposomal daunorubicin overcomes drug resistance in human breast, ovarian and lung carcinoma cells. *Journal of Liposome Research* **12**, 301-309 (2002).
27. Pavelic, Z., Skalko-Basnet, N., Filipovic-Grcic, J., Martinac, A. & Jalsenjak, I. Development and in vitro evaluation of a liposomal vaginal delivery system for acyclovir. *Journal of Controlled Release* **106**, 34-43 (2005).
28. Martina, M.S. et al. Generation of superparamagnetic liposomes revealed as highly efficient MRI contrast agents for in vivo imaging. *Journal of the American Chemical Society* **127**, 10676-10685 (2005).
29. Ayyagari, A.L. et al. Long-circulating liposomal contrast agents for magnetic resonance imaging. *Magnetic Resonance in Medicine* **55**, 1023-1029 (2006).
30. Mulder, W.J.M., Strijkers, G.J., van Tilborg, G.A.F., Griffioen, A.W. & Nicolay, K. Lipid-based nanoparticles for contrast-enhanced MRI and molecular imaging. *Nmr in Biomedicine* **19**, 142-164 (2006).
31. Saito, R. et al. Gadolinium-loaded liposomes allow for real-time magnetic resonance imaging of convection-enhanced delivery in the primate brain. *Experimental Neurology* **196**, 381-389 (2005).
32. Lasic, D.D. The Mechanism of Vesicle Formation. *Biochemical Journal* **256**, 1-11 (1988).
33. Tan, Y.C., Hettiarachchi, K., Siu, M. & Pan, Y.P. Controlled microfluidic encapsulation of cells, proteins, and microbeads in lipid vesicles. *Journal of the American Chemical Society* **128**, 5656-5658 (2006).
34. Li, Y. & Yip, W.T. Liposomes as protective capsules for active silica sol-gel biocomposite synthesis. *Journal of the American Chemical Society* **127**, 12756-12757 (2005).
35. Kazakov, S. & Levon, K. Liposome-nanogel structures for future pharmaceutical applications. *Current Pharmaceutical Design* **12**, 4713-4728 (2006).
36. Gregoriadis, G. Engineering liposomes for drug delivery: Progress and problems. *Trends in Biotechnology* **13**, 527-537 (1995).
37. Litzinger, D.C., Buiting, A.M.J., Vanrooijen, N. & Huang, L. Effect of Liposome Size on the Circulation Time and Intraorgan Distribution of Amphipathic

Poly(Ethylene Glycol)-Containing Liposomes. *Biochimica Et Biophysica Acta-Biomembranes* **1190**, 99-107 (1994).
38. Batzri, S. & Korn, E.D. Single Bilayer Liposomes Prepared without Sonication. *Biochimica Et Biophysica Acta* **298**, 1015-1019 (1973).
39. Kremer, J.M.H., Esker, M.W.J., Pathmamanoharan, C. & Wiersema, P.H. Vesicles of Variable Diameter Prepared by a Modified Injection Method. *Biochemistry* **16**, 3932-3935 (1977).
40. Szoka, F. & Papahadjopoulos, D. Comparative Properties and Methods of Preparation of Lipid Vesicles (Liposomes). *Annual Review of Biophysics and Bioengineering* **9**, 467-508 (1980).
41. Wagner, A., Vorauer-Uhl, K., Kreismayr, G. & Katinger, H. The crossflow injection technique: An improvement of the ethanol injection method. *Journal of Liposome Research* **12**, 259-270 (2002).
42. Maulucci, G. et al. Particle size distribution in DMPC vesicles solutions undergoing different sonication times. *Biophysical Journal* **88**, 3545-3550 (2005).
43. Hamilton, R.L., Goerke, J., Guo, L.S.S., Williams, M.C. & Havel, R.J. Unilamellar Liposomes Made with the French Pressure Cell - a Simple Preparative and Semi-Quantitative Technique. *Journal of Lipid Research* **21**, 981-992 (1980).
44. Jahn, A. et al. Preparation of nanoparticles by continuous-flow microfluidics. *Journal of Nanoparticle Research* **10**, 925-934 (2008).
45. Sounart, T.L. et al. Spatially-resolved analysis of nanoparticle nucleation and growth in a microfluidic reactor. *Lab on a Chip* **7**, 908-915 (2007).
46. Chan, E.M., Mathies, R.A. & Alivisatos, A.P. Size-controlled growth of CdSe nanocrystals in microfluidic reactors. *Nano Letters* **3**, 199-201 (2003).
47. Jahn, A., Vreeland, W.N., Gaitan, M. & Locascio, L.E. Controlled vesicle self-assembly in microfluidic channels with hydrodynamic focusing. *Journal of the American Chemical Society* **126**, 2674-2675 (2004).
48. Jahn, A., Vreeland, W.N., DeVoe, D.L., Locascio, L.E. & Gaitan, M. Microfluidic directed formation of liposomes of controlled size. *Langmuir* **23**, 6289-6293 (2007).
49. Brazhnik, K.P. et al. Directed growth of pure phosphatidylcholine nanotubes in microfluidic channels. *Langmuir* **21**, 10814-10817 (2005).
50. Yu-Chen Lin, M.L., Yu-Tsung Wang, Tzung-Heng Lai, Jen-Ta Chaing, Keng-Shian Huang. A new method for the preparation of self-assembled phospholipid microtubes using microfluidic technology. in *The 13th International Conference on Solid -State Sensors, Actuators, and Microsystems* 1592-1595 (Seoul, Korea, 2005).
51. Dittrich, P.S., Heule, M., Renaud, P. & Manz, A. On-chip extrusion of lipid vesicles and tubes through microsized apertures. *Lab on a Chip* **6**, 488-493 (2006).
52. Alivisatos, A.P. Semiconductor clusters, nanocrystals, and quantum dots. *Science* **271**, 933-937 (1996).
53. Jensen, K.F. Microreaction engineering - is small better? *Chemical Engineering Science* **56**, 293-303 (2001).

54. Edel, J.B., Fortt, R., deMello, J.C. & deMello, A.J. Microfluidic routes to the controlled production of nanoparticles. *Chemical Communications*, 1136-1137 (2002).
55. Cottam, B.F., Krishnadasan, S., deMello, A.J., deMello, J.C. & Shaffer, M.S.P. Accelerated synthesis of titanium oxide nanostructures using microfluidic chips. *Lab on a Chip* **7**, 167-169 (2007).
56. Knight, J.B., Vishwanath, A., Brody, J.P. & Austin, R.H. Hydrodynamic focusing on a silicon chip: Mixing nanoliters in microseconds. *Physical Review Letters* **80**, 3863-3866 (1998).
57. Bessoth, F.G., deMello, A.J. & Manz, A. Microstructure for efficient continuous flow mixing. *Analytical Communications* **36**, 213-215 (1999).
58. Johnson, T.J., Ross, D. & Locascio, L.E. Rapid microfluidic mixing. *Analytical Chemistry* **74**, 45-51 (2002).
59. Stroock, A.D. et al. Chaotic mixer for microchannels. *Science* **295**, 647-651 (2002).
60. Anna, S.L., Bontoux, N. & Stone, H.A. Formation of dispersions using "flow focusing" in microchannels. *Applied Physics Letters* **82**, 364-366 (2003).
61. Kuribayashi, K., Tresset, G., Coquet, P., Fujita, H. & Takeuchi, S. Electroformation of giant liposomes in microfluidic channels. *Measurement Science & Technology* **17**, 3121-3126 (2006).
62. Wolff, A. et al. Integrating advanced functionality in a microfabricated high-throughput fluorescent-activated cell sorter. *Lab on a Chip* **3**, 22-27 (2003).
63. Wu, Z.G. & Nguyen, N.T. Hydrodynamic focusing in microchannels under consideration of diffusive dispersion: theories and experiments. *Sensors and Actuators B-Chemical* **107**, 965-974 (2005).
64. Dixit, S., Crain, J., Poon, W.C.K., Finney, J.L. & Soper, A.K. Molecular segregation observed in a concentrated alcohol-water solution. *Nature* **416**, 829-832 (2002).
65. Hawlicka, E. & Grabowski, R. Self-Diffusion in Water Alcohol Systems .3. 1-Propanol Water Solutions of Nai. *Journal of Physical Chemistry* **96**, 1554-1557 (1992).
66. Pratt, K.C. & Wakeham, W.A. Mutual Diffusion-Coefficient of Ethanol-Water Mixtures - Determination by a Rapid, New Method. *Proceedings of the Royal Society of London Series a-Mathematical Physical and Engineering Sciences* **336**, 393-406 (1974).
67. Pratt, K.C. & Wakeham, W.A. Mutual Diffusion-Coefficient for Binary-Mixtures of Water and Isomers of Propanol. *Proceedings of the Royal Society of London Series a-Mathematical Physical and Engineering Sciences* **342**, 401-419 (1975).
68. Wakisaka, A. & Ohki, T. Phase separation of water-alcohol binary mixtures induced by the microheterogeneity. *Faraday Discussions* **129**, 231-245 (2005).
69. Chrai, S.S., Murari, R. & Ahmad, I. Liposomes (a review) - Part one: Manufacturing issues. *Biopharm-the Applied Technologies of Biopharmaceutical Development* **14**, 10-+ (2001).
70. Gregoriadis, G. (ed.) *Liposome Technology Volume 2*, (2007).

71. Haran, G., Cohen, R., Bar, L.K. & Barenholz, Y. Transmembrane Ammonium-Sulfate Gradients in Liposomes Produce Efficient and Stable Entrapment of Amphipathic Weak Bases. *Biochimica Et Biophysica Acta* **1151**, 201-215 (1993).
72. Koehler, M. *Aetzverfahren fuer die Mikrotechnik*, (Wiley, New York, 1998).
73. Laermer, F. & Schilp, A. Verfahren zum anisotropen aetzen von silicium. (German Patent DE-4241045, 1994).
74. Wyatt, P.J. Light-Scattering and the Absolute Characterization of Macromolecules. *Analytica Chimica Acta* **272**, 1-40 (1993).
75. Giddings, J.C. Field-Flow Fractionation - Analysis of Macromolecular, Colloidal, and Particulate Materials. *Science* **260**, 1456-1465 (1993).
76. Edwards, K.A. & Baeumner, A.J. Analysis of liposomes. *Talanta* **68**, 1432-1441 (2006).
77. Ruozi, B., Tosi, G., Leo, E. & Vandelli, M.A. Application of atomic force microscopy to characterize liposomes as drug and gene carriers. *Talanta* **73**, 12-22 (2007).
78. Pethrick, R.A. & Dawkins, J.V. *Modern Techniques for Polymer Characterization*, (John Wiley, 1999).
79. Bouwstra, J.A., Gooris, G.S., Bras, W. & Talsma, H. Small-Angle X-Ray-Scattering - Possibilities and Limitations in Characterization of Vesicles. *Chemistry and Physics of Lipids* **64**, 83-98 (1993).
80. Joseph E. Reiner, A.J., Laurie E. Locascio, Michael Gaitan, John J. Kasianowicz. Liposome characterization with fluorescence cumulant analysis. in *Proc. SPIE* Vol. 6602 11 (Florence, Italy, 2007).
81. Muller, J.D. Cumulant analysis in fluorescence fluctuation spectroscopy. *Biophysical Journal* **86**, 3981-3992 (2004).
82. Zhang, Z.Y., Zhao, P., Xiao, G.Z., Lin, M. & Cao, X.D. Focusing-enhanced mixing in microfluidic channels. *Biomicrofluidics* **2**(2008).
83. Hertzog, D.E. et al. Femtomole mixer for microsecond kinetic studies of protein folding. *Analytical Chemistry* **76**, 7169-7178 (2004).
84. Brotherton, C.M., Sun, A.C. & Davis, R.H. Computational modeling and comparison of three co-laminar microfluidic mixing techniques. *Microfluidics and Nanofluidics* **5**, 43-53 (2008).
85. Hertzog, D.E., Ivorra, B., Mohammadi, B., Bakajin, O. & Santiago, J.G. Optimization of a microfluidic mixer for studying protein folding kinetics. *Analytical Chemistry* **78**, 4299-4306 (2006).
86. R.K, S. & A., L. *Laminar Flow Forced Convection in Ducts*, (Academic, New York, 1978).
87. Ruiz, J., Goni, F.M. & Alonso, A. Surfactant-Induced Release of Liposomal Contents - a Survey of Methods and Results. *Biochimica Et Biophysica Acta* **937**, 127-134 (1988).
88. Grabielle-Madelmont, C., Lesieur, S. & Ollivon, M. Characterization of loaded liposomes by size exclusion chromatography. *Journal of Biochemical and Biophysical Methods* **56**, 189-217 (2003).
89. Oku, N., Kendall, D.A. & Macdonald, R.C. A Simple Procedure for the Determination of the Trapped Volume of Liposomes. *Biochimica Et Biophysica Acta* **691**, 332-340 (1982).

90. Aurora, T.S., Li, W., Cummins, H.Z. & Haines, T.H. Preparation and Characterization of Monodisperse Unilamellar Phospholipid-Vesicles with Selected Diameters of from 300 to 600 Nm. *Biochimica Et Biophysica Acta* **820**, 250-258 (1985).
91. Dams, R., Lambert, W.E., Comhaire, F. & De Leenheer, A.P. Production and characterization of sulforhodamine B containing large unilamellar vesicles labeled with atrazine. *Analytica Chimica Acta* **399**, 185-191 (1999).
92. Rigler, P. & Meier, W. Encapsulation of fluorescent molecules by functionalized polymeric nanocontainers: Investigation by confocal fluorescence Imaging and fluorescence correlation Spectroscopy. *Journal of the American Chemical Society* **128**, 367-373 (2006).
93. Chen, C.S., Yao, J. & Durst, R.A. Liposome encapsulation of fluorescent nanoparticles: Quantum dots and silica nanoparticles. *Journal of Nanoparticle Research* **8**, 1033-1038 (2006).
94. Reiner, J.E., Jahn A.,. Liposome characterization with fluorescence cumulant analysis. in *Proc. SPIE noise and fluctuations in biological, biophysical, and biomedical systems* Vol. 6602 66021-66012 (2007).
95. Magatti, D. & Ferri, F. 25 ns software correlator for photon and fluorescence correlation spectroscopy. *Review of Scientific Instruments* **74**, 1135-1144 (2003).
96. Qian, H. & Elson, E.L. Distribution of Molecular Aggregation by Analysis of Fluctuation Moments. *Proceedings of the National Academy of Sciences of the United States of America* **87**, 5479-5483 (1990).
97. Lee, R.J., Wang, S., Turk, M.J. & Low, P.S. The effects of pH and intraliposomal buffer strength on the rate of liposome content release and intracellular drug delivery. *Bioscience Reports* **18**, 69-78 (1998).
98. Isenberg, J.S., Frazier, W.A. & Roberts, D.D. Thrombospondin-1: a physiological regulator of nitric oxide signaling. *Cellular and Molecular Life Sciences* **65**, 728-742 (2008).
99. Rongen, H.A.H., Bult, A. & vanBennekom, W.P. Liposomes and immunoassays. *Journal of Immunological Methods* **204**, 105-133 (1997).
100. Isenberg, J.S. & Roberts, D.D. Personal communication. (2008).
101. Diaz-Quijada, G.A. et al. Surface modification of thermoplastics - towards the plastic biochip for high throughput screening devices. *Lab on a Chip* **7**, 856-862 (2007).
102. Tsao, C.W., Hromada, L., Liu, J., Kumar, P. & DeVoe, D.L. Low temperature bonding of PMMA and COC microfluidic substrates using UV/ozone surface treatment. *Lab on a Chip* **7**, 499-505 (2007).
103. Nishiya, T., Kainoh, M., Murata, M., Handa, M. & Ikeda, Y. Reconstitution of adhesive properties of human platelets in liposomes carrying both recombinant glycoproteins Ia/IIa and Ib alpha under flow conditions: specific synergy of receptor-ligand interactions. *Blood* **100**, 136-142 (2002).
104. Isenberg, J.S. et al. CD47 is necessary for inhibition of nitric oxide-stimulated vascular cell responses by thrombospondin-1. *Journal of Biological Chemistry* **281**, 26069-26080 (2006).

105. Isenberg, J.S., Roberts, D.D. & Frazier, W.A. Cd47: A new target in cardiovascular therapy. *Arteriosclerosis Thrombosis and Vascular Biology* **28**, 615-621 (2008).
106. Korgel, B.A., van Zanten, J.H. & Monbouquette, H.G. Vesicle size distributions measured by flow field-flow fractionation coupled with multiangle light scattering. *Biophysical Journal* **74**, 3264-3272 (1998).
107. Kerker, M. *The scattering of light and other electromagnetic radiation*, (Academic Press, 1969).
108. Glick, D. *Methods of biochemical analysis*, (John Wiley & Sons, Inc., 1988).
109. Wong, M. & Thompson, T.E. Aggregation of Dipalmitoylphosphatidylcholine Vesicles. *Biochemistry* **21**, 4133-4139 (1982).
110. Zimm, B.H. The Scattering of Light and the Radial Distribution Function of High Polymer Solutions. *Journal of Chemical Physics* **16**, 1093-1099 (1948).
111. Kaye, W. & McDaniel, J.B. Low-Angle Laser Light Scattering-Rayleigh Factors and Depolarization Ratios. *Applied Optics* **13**, 1934-1937 (1974).
112. Lecture material for the Light scattering Workshop at Wyatt Technolgy Inc.
113. Magde, D., Elson, E.L. & Webb, W.W. Fluorescence Correlation Spectroscopy .2. Experimental Realization. *Biopolymers* **13**, 29-61 (1974).
114. Magde, D., Webb, W.W. & Elson, E. Thermodynamic Fluctuations in a Reacting System - Measurement by Fluorescence Correlation Spectroscopy. *Physical Review Letters* **29**, 705-&& (1972).
115. Hess, S.T., Huang, S.H., Heikal, A.A. & Webb, W.W. Biological and chemical applications of fluorescence correlation spectroscopy: A review. *Biochemistry* **41**, 697-705 (2002).
116. Rigler, R., Mets, U., Widengren, J. & Kask, P. Fluorescence Correlation Spectroscopy with High Count Rate and Low-Background - Analysis of Translational Diffusion. *European Biophysics Journal with Biophysics Letters* **22**, 169-175 (1993).
117. Hess, S.T. & Webb, W.W. Focal volume optics and experimental artifacts in confocal fluorescence correlation spectroscopy. *Biophysical Journal* **83**, 2300-2317 (2002).
118. Wohland, T., Rigler, R. & Vogel, H. The standard deviation in fluorescence correlation spectroscopy. *Biophysical Journal* **80**, 2987-2999 (2001).
119. Krichevsky, O. & Bonnet, G. Fluorescence correlation spectroscopy: the technique and its applications. *Reports on Progress in Physics* **65**, 251-297 (2002).
120. Chen, Y., Muller, J.D., So, P.T.C. & Gratton, E. The photon counting histogram in fluorescence fluctuation spectroscopy. *Biophysical Journal* **77**, 553-567 (1999).